Final Technical Report
October 2004 – November 2006

High Performance Flexible Reversible Solid Oxide Fuel Cell

Performed under DOE Cooperative Agreement DE-FC36-04GO14351

Prepared for
United States Department of Energy
Golden Field Office
Golden, CO

Jie Guan
Nguyen Minh
Badri Ramamurthi
James Ruud
Jin-Ki Hong
Patrick Riley
Dacong Weng

GE Global Research Center

19310 Pacific Gateway Drive
Torrance, CA 90502

DISCLAIMER

ABSTRACT

This report summarizes the work performed for the program entitled “High Performance Flexible Reversible Solid Oxide Fuel Cell” under Cooperative Agreement DE-FC36-04GO14351 for the U. S. Department of Energy. The overall objective of this project is to demonstrate a single modular stack that generates electricity from a variety of fuels (hydrogen and other fuels such as biomass, distributed natural gas, etc.) and when operated in the reverse mode, produces hydrogen from steam. This project has evaluated and selected baseline cell materials, developed a set of materials for oxygen and hydrogen electrodes, and optimized electrode microstructures for reversible solid oxide fuel cells (RSOFCs); and demonstrated the feasibility and operation of a RSOFC multi-cell stack. A 10-cell reversible SOFC stack was operated over 1000 hours alternating between fuel cell (with hydrogen and methane as fuel) and steam electrolysis modes. The stack ran very successfully with high power density of 480 mW/cm^2 at 0.7V and 80% fuel utilization in fuel cell mode and >6 SLPM hydrogen production in steam electrolysis mode using about 1.1 kW electrical power. The hydrogen generation is equivalent to a specific capability of 2.59 Nm^3/m^2 with electrical energy demand of 3 kWh/Nm^3. The performance stability in electrolysis mode was improved vastly during the program with a degradation rate reduction from 8000 to 200 mohm-cm^2/1000 hrs. This was accomplished by increasing the activity and improving microstructure of the oxygen electrode. Both cost estimate and technology assessment were conducted. Besides the flexibility running under both fuel cell mode and electrolysis mode, the reversible SOFC system has the potentials for low cost and high efficient hydrogen production through steam electrolysis. The cost for hydrogen production at large scale was estimated at ~\$2.7/kg H_2, comparing favorably with other electrolysis technology.

TABLE OF CONTENTS

TABLE OF ABBREVIATIONS

ASR:	Area Specific Resistance
ATR:	Autothermal Reforming
BOP:	Balance of Plant
BOS:	Balance of System
CoH	Cost of Hydrogen
CTE:	Coefficient of Thermal Expansion
DC:	Direct Current
EMPA:	Electron Microprobe Analysis
GDC:	Gadolinia Doped Ceria
GE:	General Electric Company
GE-GR:	GE Global Research
LSC:	Lanthanum Strontium Cobaltite
LSCF:	Lanthanum Strontium Cobalt Ferrite
LSF	Lanthanum Strontium Ferrite
LSM:	Lanthanum Strontium Manganite
OCV:	Open Circuit Voltage
PEM	Proton Exchange Membrane
RSOFC	Reversible Solid Oxide Fuel Cell
S/C:	Steam-to-Carbon Ratio
ScSZ:	Scandia-Stabilized Zirconia
SDC:	Samaria Doped Ceria
SEM:	Scanning Electron Microscope
SLPM	Standard Liter Per Minute
SOEC:	Solid Oxide Electrolysis Cell
SOFC:	Solid Oxide Fuel Cell
SR:	Steam Reforming
YSZ:	Yttria-Stabilized Zirconia

EXECUTIVE SUMMARY

This report summarizes the work performed for the program entitled “High Performance Flexible Reversible Solid Oxide Fuel Cell” under Cooperative Agreement DE-FC36-04GO14351 for the U. S. Department of Energy. The overall objective of this project is to demonstrate a single modular stack that generates electricity from a variety of fuels (hydrogen and other fuels such as biomass, distributed natural gas, etc.) and when operated in the reverse mode, produces hydrogen from steam. This project has developed a set of materials and optimized electrode microstructures for reversible solid oxide fuel cells (RSOFCs); and demonstrated the feasibility and operation of a reversible SOFC multi-cell stack. The technology advancements in this program have formed a basis for future work to move the technology toward practical application.

The project was successfully completed with major accomplishments highlighted below:

- Materials for reversible SOFC were reviewed and a topical report was generated, summarizing the options available and the selected materials for investigation.
- Several oxygen electrode candidates were screened, including lanthanum strontium manganites (LSM), lanthanum strontium ferrites (LSF), and lanthanum strontium cobalt ferrites (LSCF). Under both fuel cell and electrolysis operating mode, performance of the oxygen electrode is in the order of LSCF>LSF>LSM/YSZ.
- Excess performance degradation has been observed with LSM/YSZ as the oxygen electrode in electrolysis mode mainly due to electrode delamination. LSCF and LSF have shown better performance stability in electrolysis mode than LSM/YSZ electrode.
- Oxygen electrode performance “irreversibility” has been associated with differences in vacancy diffusion and activation at the oxygen electrode/electrolyte interface under fuel cell mode and electrolysis mode. Higher current densities can lead to depletion of vacancies at the interface in electrolysis mode. Experimental data has matched well with a non-symmetrical vacancy model.
- Higher polarization losses for hydrogen electrode have been predicted under electrolysis mode mainly due to difference in H_2 and H_2O diffusions. Thinner electrode and smaller particles are preferred.
- Cell performance with LSCF oxygen electrode has been evaluated for fuel cell mode, electrolysis mode, and fuel cell/electrolysis cyclic mode. Degradation was similar in fuel cell, electrolysis, and cyclic modes and perhaps enhanced degradation in electrolysis mode.

- Internal reforming with Ni/YSZ has been modeled and demonstrated. >98% CH_4 conversion was measured, consistent with thermodynamic prediction. Fuel cell performance with internal reforming was similar to that with 64%H_2/36%N_2 fuel.
- Performance has been improved with electrode material selection and process engineering. Substantial degradation rate reduction has been achieved with LSCF oxygen electrode in electrolysis mode. The area specific resistance (ASR) for the electrolysis mode has been reduced to ~400 mohm-cm^2 and the degradation rate has been reduced to about 200-300 mohm-cm^2/1000hrs.
- Performance degradation has been characterized with LSCF oxygen electrode. For the uncoated interconnects, the initial ASR at 750°C was 20% higher than the ASR at 800°C but the degradation rate was about two times slower. A protective coating on the metallic interconnect has been evaluated. The cells with the coated interconnect has shown a factor of two reduction in degradation rate while maintaining the initial ASR.
- Several multi-cell stacks have been built and tested under power generation and electrolysis mode. A 10-cell stack has been operated over 1000 hours alternating between fuel cell and steam electrolysis modes. The stack has run very successfully with high performance of 480 mW/cm^2 at 0.7V and 80% fuel utilization in fuel cell mode, and 6 SLPM hydrogen production in steam electrolysis mode using about 1.1 kW electrical power. The hydrogen generation is equivalent to a specific capability of 2.59 Nm^3/m^2 with electrical energy demand of 3 kWh/Nm^3.
- Varied hydrogen production technologies have been reviewed with focus on steam reforming and water electrolysis. The potentials and technical challenges have been analyzed. High temperature steam electrolysis has potential for high electrolyzer efficiency, thus the potentials for reducing electrical energy demand and lowering hydrogen production cost.
- The cost estimate of RSOFC has been conducted for fuel cell mode, dual mode and the electrolysis mode. The electrical energy cost is the major contributor to the hydrogen production cost. Besides the flexibility running under both fuel cell mode and electrolysis mode, the RSOFC has the potentials for low cost and high efficient hydrogen production through steam electrolysis. The cost of hydrogen production at large scale has been estimated at ~\$2.7/kgH_2, comparing favorably with other electrolysis technology.

1 INTRODUCTION

This report summarizes the work performed for the program entitled "High Performance Flexible Reversible Solid Oxide Fuel Cell" under Cooperative Agreement DE-FC36-04GO14351 for the U. S. Department of Energy. The overall objective of this project is to demonstrate a single modular stack that generates electricity from a variety of fuels (hydrogen and other fuels such as biomass, distributed natural gas, etc.) and when operated in the reverse mode, produces hydrogen from steam. This project has culminated in the demonstration of the feasibility and operation of a reversible solid oxide fuel cell multi-cell stack and the development of a set of materials and optimized electrode microstructures. The advancements have formed a basis for further work to move the technology toward practical application.

2 OVERVIEW

Solid oxide fuel cells (SOFCs) are known to be reversible, i.e., they can be operated under dual modes: power generation mode and electrolysis mode. In power generation mode, the SOFC acts as a fuel cell and generates electricity by electrochemically combining fuel and oxidant. In reverse mode when power is applied to the cell, the SOFC acts as an electrolyzer and produces chemicals such as hydrogen through steam electrolysis.

A reversible SOFC (RSOFC) is a single unit that operates efficiently in both power generation and hydrogen production modes. Since the SOFC has the capability for internal reforming of hydrocarbons, the RSOFC can be made fuel flexible. Fuel-flexible RSOFCs eliminate the need for an external reformer, thus simplifying the system and reducing system costs. With the RSOFC, a completely renewable production of electricity and hydrogen becomes possible when power generation and water or steam electrolysis are coupled. For instance, a renewable energy supply (e.g., solar, wind) can be used by the fuel cell to produce hydrogen and oxygen from water. These chemicals can be used directly or stored for subsequent uses to produce electricity through the same fuel cell in reverse mode. Similarly, the RSOFC can generate electricity from biomass, and the electricity can then be used to produce hydrogen from steam electrolysis. Figure 2-1 schematically illustrates the operating principles of a RSOFC with an oxygen-ion electrolyte.

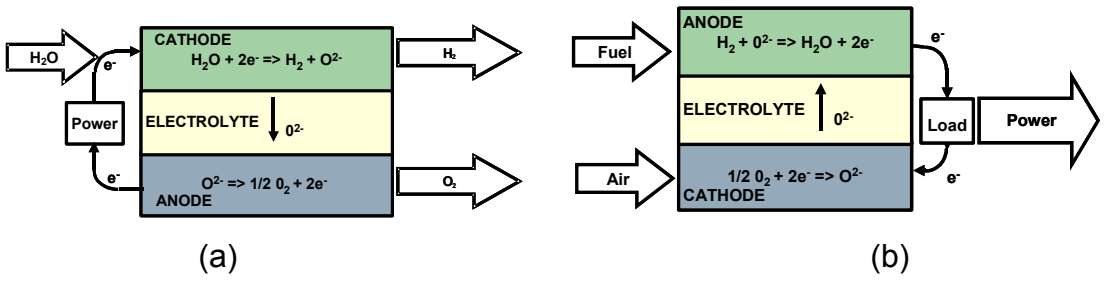

Figure 2-1. (a) H_2 generator, (b) Fuel Cell

The key challenges in the development of fuel-flexible reversible SOFCs relate to the reversibility of the electrodes and the internal reforming capability of the anode or hydrogen electrode. The reversible electrode must provide adequate performance and

durability in both power generation and electrolysis operation. Challenges on the reversible hydrogen electrode for internal reforming are risks associated with carbon deposition and thermal management. The combination of reversibility and reforming capability presents significant technical challenges in electrode development. To achieve the project objectives, the overall approach for the program is shown in Figure 2-2. The project concentrated on three areas: reversible electrode development, reversible cell evaluation, and stack demonstration. These efforts addressed the key technical challenges except the thermal management issues associated with internal reforming. Thermal management for operation with internal reforming is currently being addressed in the on-going SOFC projects at GE. A cost analysis effort and a technology assessment were also conducted to estimate the hydrogen production cost and evaluate the status and potential of reversible SOFC technology.

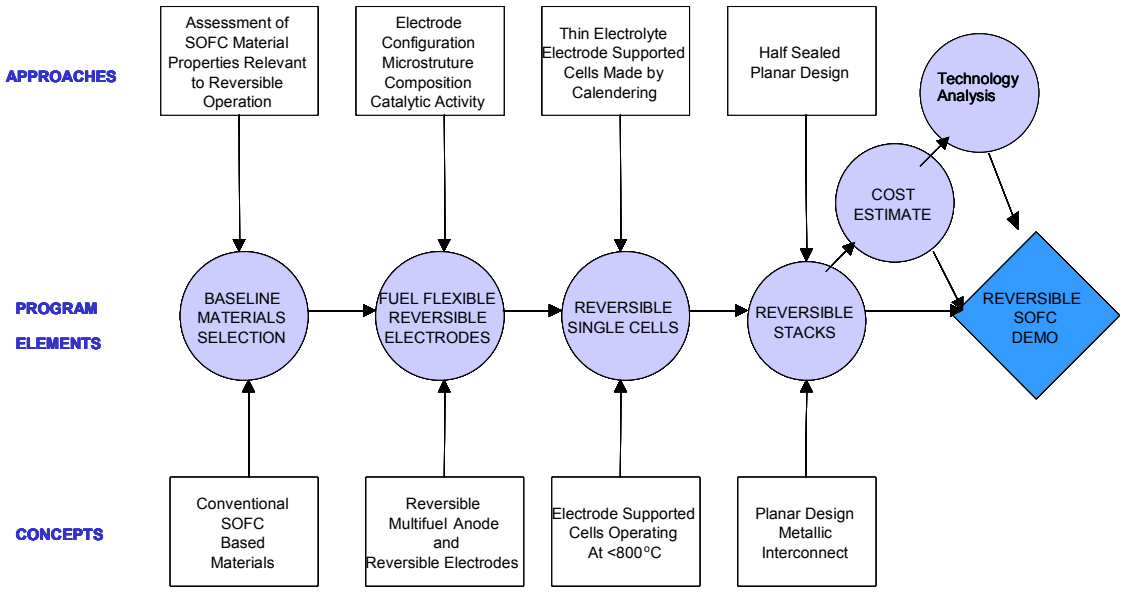

Figure 2-2. A schematic showing the approaches, program elements, and concepts

The program has been executed according to the overall approach outlined in Figure 2-2. Progress was summarized and reported in the following areas:

- Electrode development
- Cell fabrication and evaluation
- Stack development
- Cost estimate
- Technology assessment

3 ELECTRODE DEVELOPMENT

3.1 MATERIALS ASSESSMENT

The objective of this effort was to conduct a comprehensive material assessment to define the compositions of the baseline materials to be evaluated for this project with focus on (i) compiling all potential materials, (ii) evaluating materials against the criteria for reversibility and reforming capability to verify selection, (iii) identifying key elements for improved reversibility and reforming capability, and (iv) defining compositions of the baseline materials for the project.

In term of the technology status, the SOFC has been developed extensively for stationary powers and recently, portable (soldier power) and mobile (auxiliary power unit or APU) applications [1-3]. Power plants up to 250 kW size have been demonstrated. Work on high-temperature electrolysis (hydrogen from steam, pure oxygen from air, and oxygen from CO_2) using oxygen-ion or proton-conducting oxides has been limited to small stack/system demonstrations and laboratory-scale investigations. Table 3-1 summarizes the status of SOFC technology and high-temperature electrolysis based on oxygen-ion and proton conductors.

Table 3-1. Summary of status of SOFC technology and high-temperature electrolysis

Device	Products	Electrolyte	Electrodes	Status and Key Challenges
SOFC	Electricity from a variety of fuels	Zirconia, Ceria, Gallate (O^{2-} conductors)	Cathode: LSM, LSCF, LSF, SSC Anode: Ni	Demo units up to 250 kW in operation • Performance improvement • Stack/system cost reduction
Electrolyzer	H_2 and O_2 from H_2O	Zirconia, Ceria, Gallate (O^{2-} conductors)	Cathode: Pt Anode: Pt, LSM, LSF, LSCF, SSC	R&D bench scale, small demo units • Materials development • Polarization losses • Interface stability
		$Ba(Sr)CeO_3$, $Ba(Sr)ZrO_3$, $A_3(B'B'')O_9$, (H^+ conductors)	Cathode: Pt Anode: Pt	R&D bench scale • Materials development • Materials stability • Conductivity • Polarization losses
	O_2 from CO_2	Zirconia, Ceria, Gallate (O^{2-} conductors)	Cathode: Pt Anode: Pt, LSM, LSF, LSCF, SSC	R&D bench scale • Materials development • Polarization losses • Interface stability

LSM: $La_{1-x}Sr_xMnO_3$; LSCF: $(La_xSr_{(1-x)})_y\ Co_{(1-z)}\ Fe_zO_{3-\delta}$; LSF: $La_{1-x}Sr_xFeO_3$; SSC: $Sm_{0.5}Sr_{0.5}CoO_3$

3.1.1 Electrolyte Systems

The main options for the electrolyte materials are oxygen-ion conductors (stabilized zirconia, doped ceria, doped lanthanum gallate) and proton conductors (doped cerates, zirconates) as shown in Table 3-1.

3.1.1.1 High Temperature Proton Conductors

A proton conductor is a compound in which proton (H^+) can move (conduct) freely in the material lattice. The major proton-conducting compounds include (1) water-containing systems, (2) oxo acids and their salts (sulfates, selenates, phosphates, and arsenates), (3) blend of organic and inorganic compounds, and (4) high-temperature proton conductors. Only high temperature proton conductors are potentially suitable for RSOFC application. High-temperature proton-conducting compounds are mainly hydroxides and oxides. Phosphates with the structure of ($Ca_5(PO_4)_3OH$) may retain structural hydroxyl ions (i.e., hydroxides) up to very high temperatures (>1000°C); however, the proton conductivity is very low. Oxide-based proton conductors include Y_2O_3, La_2O_3, $KTaO_3$, acceptor-doped titanates ($MTiO_3$, M=Sr, Ba), accepted-doped cerates ($ACeO_3$, A=Sr, Ba), zirconates ($AZrO_3$, A=Ca, Sr, and Ba), and thoria ($BaThO_3$). Specific efforts in high temperature proton conductors have been concentrated on developing perovskite-type proton conductors such as $ACeO_3$, $AZrO_3$, and $BaThO_3$ because of their relatively high proton conductivities. Cerates-based perovskites are the most attractive candidates because of the combination of high proton conductivity and good stability under fuel cell operating environments. Two well-known $ACeO_3$-based proton conductors are doped $BaCeO_3$ and $SrCeO_3$, in which substitution for Ce by trivalent cations creates oxygen vacancies and other charged defects, resulting in mixed conduction in atmospheres containing O_2, H_2 and H_2O vapor. In $ACeO_3$-based proton conductors, since the incorporation of protons into materials is through the reaction of proton-containing species with the oxygen related defects, materials typically have mixed oxygen-ion and proton conductivity. $SrCeO_3$ with orthorhombic structure is more distorted from cubic lattice than $BaCeO_3$ with tetragonal structure. The orthorhombic structure of $SrCeO_3$ inhibits oxygen-ion conduction but has little influence on proton conduction. Consequently, protonic conduction may be favorable in $SrCeO_3$-based materials and thus may be more suitable for steam electrolysis in comparison with $BaCeO_3$-based materials.

All of the existing high temperature proton conductors have limited applications in RSOFC. Cerates have acceptable conductivity, but they are not stable as they readily react with water and carbon dioxide. Zirconates are relatively stable, but their conductivity is too low for practical applications.

3.1.1.2 Oxygen-ion Conductors

The most popular oxygen-ion conductive electrolyte is stabilized zirconia because of its well-known stability and acceptable conductivity as they are the two key parameters in selection of electrolyte material. For alternate electrolytes, the desired temperature of operation may determine the choice of materials.

Stabilized Zirconia: Stabilized zirconia has been widely used as SOFC electrolyte materials because of its well-known stability and acceptable ionic conductivity [2,4]. For 8mol% yttria-stabilized zirconia (8YSZ, $Zr_{0.84}Y_{0.16}O_2$), the typical density is around 5.90g/cm^3 and the conductivity at 800°C is ~0.03 S/cm and thermal

expansion coefficient (100-1000°C) is around $10.8x10^{-6}$ K^{-1}. The bending strength of 8YSZ is ~300 and ~225 MPa at 25°C and 1000°C, respectively. Scandia-stabilized zirconia (ScSZ) usually has higher conductivity than YSZ. The conductivity of 10%mol Sc_2O_3 doped ZrO_2 (10ScSZ) is ~0.08 S/cm at 800°C. The thermal expansion coefficient and mechanical strength of ScSZ are also close to those of YSZ. Stabilized zirconia can exhibit conductivity aging and its impact on SOFC performance and stability can be significant if the aging rate is fast and the electrolyte is relatively thick. The conductivity aging is considered to be due to grain boundary conduction change with time and precipitation of tetragonal phase from cubic matrix. Conductivity aging of ScSZ is typical and it is being addressed with co-dopant such as Y, Ce, and Al. YSZ also exhibits aging and the conductivity aging effect appears to be reduced by increasing mole percentage of yttria to ~10mol%.

Doped Ceria: Ceria electrolytes are commonly considered for use at lower temperatures (<550°C) where the electronic conductivity is insignificant. Ceria electrolytes also have a lower mechanical strength than zirconia. The thermal expansion coefficient of doped ceria is typically higher than doped zirconia. For example, the thermal expansion coefficients (50-900°C) for $Ce_{0.8}Sm_{0.2}O_{1.9}$ (SDC20) and $Ce_{0.8}Gd_{0.2}O_{1.9}$ (GDC20) are 13.3 and $12.9x10^{-6}$ K^{-1}, respectively [5].

Lanthanum Gallates: Perovskite $LaGaO_3$ doped with Sr for La and Mg/Fe/Co for Ga site exhibits high oxygen-ion conductivity. For a gallate-based electrolyte, particular attention should be paid to its reactivity with nickel, low mechanical strength, volatility of Ga species at high temperatures, and the high cost associated with the usage of gallium.

3.1.2 Oxygen Electrode

The main function of the oxygen electrode is to provide the reaction sites for the electrochemical reduction of oxidant in fuel cell mode and oxygen evolution in electrolysis mode. The common materials can be grouped into (1) noble metal electrode, (2) lanthanum manganites, (3) cobaltites, and (4) ferrites. Each group of materials includes a number of variations in doping species and dopant amount. Selection of the oxygen electrode material depends on the desired electrochemical and mechanical properties, such as catalytic activity, electrical conductivity, and thermal expansion coefficient. It also depends on the material's chemical stability/compatibility with neighboring materials, such as the electrolyte, interconnect, and contact materials.

Metal-based Electrode: Materials for use in metal-based oxygen electrode include Pt, Ag, Pd and their mixtures with compatible electrolyte materials. For instance, Pt/YSZ has been used as the oxygen electrode for CO_2 reduction and steam electrolysis. Pd/YSZ can be used as an SOFC cathode. These electrode materials are generally stable but their catalytic activities are relatively low because of limited length of triple phase boundaries that is possible to achieve. Also, the interface between the electrode and electrolyte is relatively weak and the cost associated with the noble metal is high.

Lanthanum Manganites: Doped $LaMnO_3$ has been extensively used as cathode materials in SOFCs. This selection has been primarily on three factors: high electrical conductivity in oxidized atmospheres, adequate compatibility with yttria stabilized zirconia electrolyte, and acceptable thermal expansion match with other cell/stack components. Various dopants have been investigated to tailor the material properties, including strontium, calcium, barium, chromium, cobalt, iron, copper, lead, magnesium, nickel, potassium, sodium, titanium, rubidium, and yttrium. Presently, strontium doping is the most commonly used. Sr-doped lanthanum manganite (LSM) can be expressed in a general formula of $(La_{1-x}Sr_x)_{1-y}MnO_3$. Material properties vary with the level of Sr doping x and A site deficiency y.

Lanthanum Cobaltites: Doped lanthanum cobaltites ($LaCoO_3$) are another perovskite cathode material for the SOFC. Similar to $LaMnO_3$, $LaCoO_3$ can also be doped with various dopants to tailor the material properties. Generally, lanthanum cobaltites have a higher conductivity and catalytic activity than lanthanum manganites, but the cobaltites tend to readily interact with YSZ electrolytes to form insulating phases, such as $SrZrO_3$ and $La_2Zr_2O_7$ even with A-site deficiency. Thermal expansion coefficients of lanthanum cobaltites are also relatively high ($>18x10^{-6}$ K^{-1}). These electrode materials have been investigated for ceria- and gallate-based electrolytes. They can also be used for zirconia electrolyte, but a barrier layer such as ceria must be implemented to reduce interactions.

Lanthanum Ferrites: Doped lanthanum ferrites ($LaFeO_3$) are another perovskite cathode material recently explored for SOFC electrodes. Similar to $LaMnO_3$ and $LaCoO_3$, $LaFeO_3$ can also be doped with various dopants to tailor material properties. Generally, lanthanum ferrites have a higher conductivity and catalytic activity than lanthanum manganites. Thermal expansion coefficients are only moderately high ($12\sim13x10^{-6}$ K^{-1}). Long-term performance stability of this material has to be proven.

3.1.3 Hydrogen Electrode

The main function of the hydrogen electrode is to provide reaction sites for electrochemical oxidation of the fuels in fuel cell mode and steam reduction in electrolysis mode. Possible hydrogen electrodes are based on available SOFC anode materials such as (1) Ni-based, (2) Cu-based, and (3) conducting ceramic-based materials. Selection of material depends on its stability, conductivity, compatibility, porosity, catalytic activity, and thermal expansion.

Ni-based Electrode: Porous Ni/YSZ cermet is currently the most extensively used anode material for the SOFC application because of its low cost (as compared to noble metals such as Pt and Pd), stability, catalytic activity, and conductivity. The Ni-based anode is also a fairly good catalyst for steam reforming although it also tends to promote carbon deposition when the steam-to-carbon ratio is low. Concerns over the Ni-based anode include its limited sulfur tolerance (< 10ppm) and redox tolerance as Ni tends to interact with sulfur and it can also be re-oxidized at high temperatures when the oxygen partial pressure is high enough. In addition to the commonly used Ni/YSZ

cermet, Ni/ceria and Ni/Sc-zirconia are also being used to enhance their electrochemical activities and reforming ability.

Cu-based Electrode: Similar to Ni/ceria cermet, Cu/ceria cermet is being considered for the SOFC anode primarily for direct hydrocarbon oxidation, as Cu does not promote carbon deposition as Ni does. However, Cu has low activity for fuel oxidation, and its low melting point imposes additional challenges in operating conditions and fabrication processes. Similar to Ni-based electrodes, the Cu-based electrode also has limited sulfur tolerance and redox tolerance.

Conducting Ceramic Electrode: To address sulfur and redox tolerance issues, several conducting ceramics are being explored, such as doped (La, Sr)TiO_3, doped $LaNiO_3$, doped $LaCrO_3$, and doped niobates. Most of these ceramic anodes are in their early development stages and their catalytic activity and conductivity are relatively low for efficient operations.

3.1.4 Selection Criteria

The preferred materials must have high electrochemical performance and sufficient durability/stability in both power generation and electrolysis operation mode.

For high electrochemical performance, the following criteria must be met:

- electrolyte must be conductive enough
- hydrogen electrode must have low concentration polarization, low ohmic losses and be capable of internal reforming
- oxygen electrode must have low activation polarization and low ohmic losses

For sufficient durability, the selected materials must meet the following requirements:

- electrolyte must be stable with both oxidizing and reducing environments
- electrolyte materials must have sufficient mechanical properties
- both electrode materials must be compatible with the electrolyte
- hydrogen electrode must be resistant to coking, redox, and have low coarsening rates
- oxygen electrode must have sufficient oxygen evolution kinetics to avoid electrode pitting/delaminating, low sintering rates, and adequate compatibility with metallic interconnects

3.1.5 Baseline Materials

3.1.5.1 Electrolyte Materials

Stabilized zirconia has been used almost extensively as the electrolyte materials for SOFCs because the material possesses adequate oxygen–ion conductivity and exhibits desirable stability in both oxidizing and reducing atmospheres. Although its conductivity is not as high as ceria and gallate based materials, its ohmic losses can be minimized with thin-film electrolytes. Based on the selection criteria and other programmatic conditions, yttria-stabilized zirconia (YSZ), more specifically, 8mol% Y_2O_3 doped zirconia, was used as baseline electrolyte material for RSOFC development under this program. Electrode materials were selected to be compatible with the YSZ electrolyte.

3.1.5.2 Oxygen Electrode

Oxygen electrode materials were based on LSM and selected variations from La-Sr-Co-Fe based materials. Selection of LSM was based on its well-known compatibility and fair performance demonstrated so far as SOFC electrode materials. Improvement of LSM was focused on its microstructure and interface properties to improve the reversibility and durability. Selection of La-Sr-Co-Fe based electrode was based on its potential of high performance while its compatibility and fabricability were to be proven. The oxygen electrode materials down-selection was based on the progress in electrode performance, durability as well as feasibility within the program scope, schedule, and budget.

LSM-based Electrode: To be efficient and reliable for RSOFC, both performance and durability of LSM based materials need to improve. First, materials originally developed for power generation need to be optimized for electrolysis mode. Second, durability of the oxygen electrode is generally low under electrolysis operation, improvement on this property is required for reversible applications. Experiments at GE with symmetric LSM-YSZ electrodes under constant current densities of 0.5 A/cm^2 have shown that the anodic oxygen electrode can delaminate from the electrolyte in as short as five days. Two LSM-based materials were selected: one baseline LSM-1 and another LSM-2 with slightly higher Sr content for higher conductivity.

La-Sr-Co-Fe-based Electrode: Mixed ionic electronic conductors (MIEC) with ceria barrier layers was another choice of oxygen electrode. Ferrites and cobaltites in the family $(A_xSr_{(1-x)})_yFe_zCo_{(1-z)}O_{3-\delta}$ have significant mixed ionic and electronic conductivity compared with LSM, which is almost purely an electronic conductor. The increased ionic conductivity is expected to spread out the oxygen reaction zone and reduce the degradation rates compared with LSM in electrolysis mode.

The compositional space to be investigated focused around low Co levels to reduce the coefficient of thermal expansion (CTE) mismatch between the MIEC and other cell components. The degree of substoichiometry, y, is an important parameter which was varied to evaluate the effect on both performance in power generation and

electrolysis mode. Substoichiometric perovskites reduce the formation of undesired products and produce distorted perovskite structures with enhanced catalytic activity. The focused compositions were $(La_{0.8}Sr_{0.2})_{0.95}FeO_3$ (LSCF 82-25), another Sr-doped $LaFeO_3$ (LSF-2), and one composition with general formula of $(L_xSr_{(1-x)})_yFe_zCo_{(1-z)}O_{3-\delta}$ (LSCF-1).

A samaria-doped-ceria (SDC) barrier layer can be used between the oxygen electrode and the YSZ electrolyte. In addition to preventing unwanted reactions with the electrolyte during processing, ceria layers have been shown to reduce the cell area specific resistance or ASR in electrolysis. The increased ionic conductivity may spread the reaction zone allowing more efficient use of the cell area.

3.1.5.3 Hydrogen Electrode

Ni-YSZ was selected as hydrogen electrode for ROSFC because of its well-known properties and its high performance as SOFC anode although limited results are available on steam electrolysis. Volume fraction of Ni can be varied in the range of 40-80% and raw materials (both YSZ and NiO) characteristics can be modified to achieve microstructures for reduced activation polarization, reduced concentration polarization, improved mechanical strength and CTE match, and electronic conductivity.

3.1.6 Summary

An assessment of potential materials for reversible SOFCs was conducted. The assessment included (i) compiling all potential materials, (ii) evaluating materials against the criteria for reversibility and reforming capability to verify selection, (iii) identifying key elements for improved reversibility and reforming capability, and (iv) defining compositions of the baseline materials for the project. Based on assessment of materials and technology status and program budget and schedule constraints, the following materials were selected for development under this program:

- Yttria-stabilized zirconia (YSZ), more specifically, 8mol% Y_2O_3 doped zirconia was used as baseline electrolyte material. Electrode materials were selected to be compatible with the YSZ electrolyte.
- Oxygen electrode materials were based on LSM and selected variations from La-Sr-Co-Fe based materials. Selection of LSM was based on its well-known compatibility and excellent performance demonstrated so far as SOFC electrode material. Selection of La-Sr-Co-Fe based electrode was based on its potential of high performance while its compatibility and fabricability needed to be proven in the beginning of the electrode development tasks. Two LSM (LSM-1, and LSM-2), two LSF (LSCF 82-25, LSF-1) and LSCF (LSCF-1) are selected for study.
- Ni-YSZ was selected as hydrogen electrode for RSOFC with improvements focusing on microstructure engineering.

3.2 ELECTRODE MODELING

The objective of this effort was to develop models to provide guidance and prediction for optimized microstructures with focus on (i) electrode modeling, (ii) electrode reversibility, (iii) electrode microstructure, and (iv) internal reforming on hydrogen electrode.

3.2.1 Electrode Modeling

The reversible electrode model describes the performance of a reversible solid oxide fuel cell consisting of three layers, namely, the hydrogen electrode, electrolyte, and oxygen electrode. Material and microstructure parameters are the inputs to the model. Using these parameters, the effective transport and reaction parameters such as electronic/ionic conductivity and active surface area are computed. The effective transport and reaction parameters are then provided as inputs to the performance model, which computes the performance for given operating conditions such as cell temperature, fuel composition and operating voltage. The model is capable of predicting performance, both in power generation and electrolysis modes.

The key assumptions in the model are as follows:

- The assumption of electroneutrality leads to formulate the model in terms of one composition variable, i.e., the electrochemical potential of ions ($\overline{V}_i$) and one electrical state variable, i.e., the electrochemical potential of electrons ($\overline{V}_e$).
- Butler-Volmer reaction kinetics (with transfer coefficient $\beta = 0.5$) was used in the model to describe the overall redox reactions in the electrodes. Furthermore, the reaction kinetics in the anode and cathode was assumed to be similar in electrolysis and power generation modes.
- Contact resistances at the interconnect/electrode and electrode/electrolyte interfaces were not considered in the model. Although the interfacial charge transfer rate can be modeled by Butler-Volmer kinetics, reliable estimates of the interfacial exchange current density were not available.
- The fuel cell was assumed to operate under isothermal conditions with cell temperature equal to the operating temperature.
- The system was one-dimensional with all variations in fuel composition and potential occurring across the thickness of the fuel cell. The assumption was expected to be valid for button cells (1 inch size) under low fuel (or steam) utilization conditions.

Shown in Figure 3-1 and Figure 3-2 are the model predictions in comparison with button cell performance under low fuel utilization conditions in the power generation mode. Two oxygen electrodes, LSM/YSZ and LSF, were considered. The cell temperature was varied between 650 and 850°C, while the fuel composition was fixed (97% H_2 with 3% humidification).

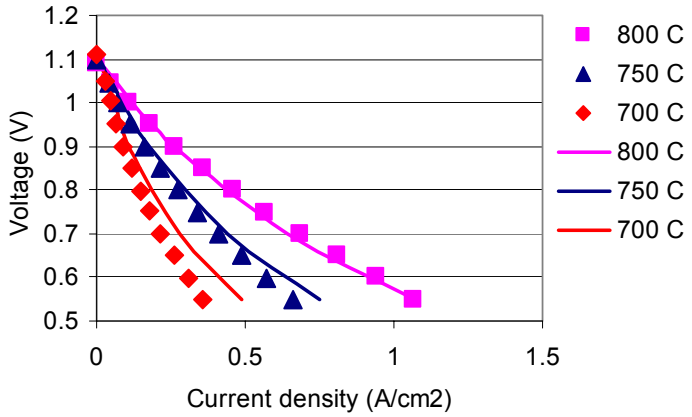

Figure 3-1 Model prediction (solid lines) is compared with experimental data (closed symbols) for a fuel cell with LSM/YSZ as the cathode.

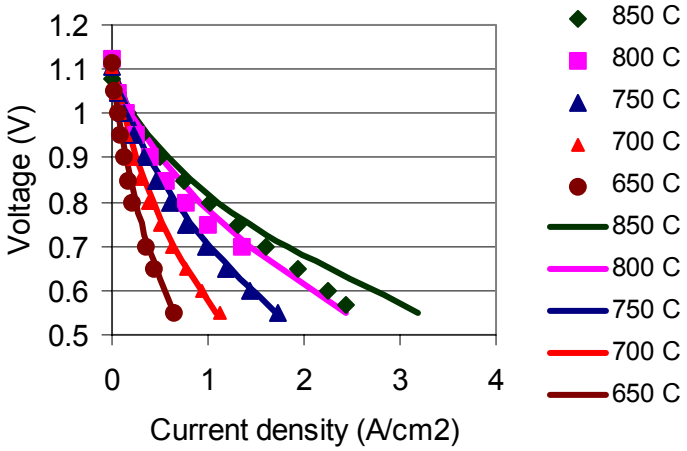

Figure 3-2 Model prediction (solid lines) is compared with experimental data (closed symbols) for a fuel cell with LSF as the cathode.

For the purposes of validation, the oxygen electrode exchange current density, i_{0c}, was known with the least amount of certainty and hence was considered to be an adjustable parameter. The activation energies [6, 7] of ~1.6 eV for LSM/YSZ and 1.85 eV for LSF were seen to provide reasonable agreement with data. Estimated exchange current densities were 0.15 A/cm^2 for LSM/YSZ and 0.1 A/cm^2 for LSF at 800°C in air. Literature estimates from surface exchange coefficient data [8] yield exchange current densities of 0.2 and 0.6 A/cm^2 at 800°C for Sr contents of 0.1 and 0.4 respectively in LSF, indicating reasonable agreement with our estimates.

3.2.2 Electrode Reversibility

3.2.2.1 Oxygen Electrode

The irreversible behavior of oxygen electrode might be associated with the diffusion of oxygen vacancies through the perovskite and adsorbed oxygen through the surface [9]. Based on the hypothesis, an oxygen electrode model was developed to solve for the diffusion and reaction of oxygen vacancies through the thickness of the oxygen electrode.

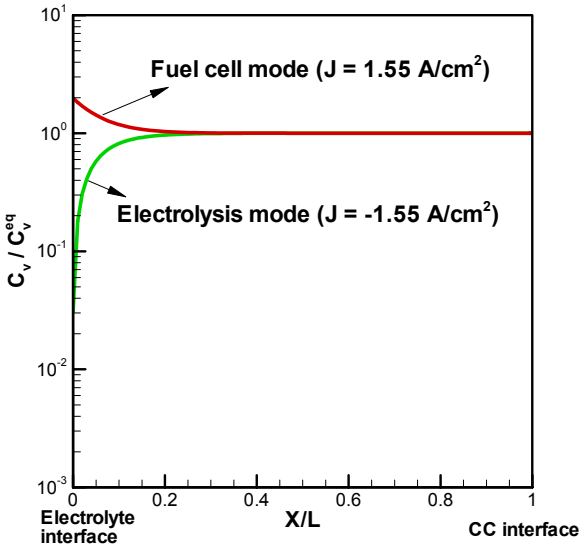

Figure 3-3 Spatial variation of vacancy concentration along the thickness of the oxygen electrode at 700°C. The total current density is 1.55 A/cm^2.

Figure 3-3 shows a typical spatial variation of normalized vacancy concentration for a constant current density of 1.55 (fuel cell mode) and -1.55 A/cm^2 (electrolysis mode). Under the fuel cell mode, the vacancy concentration of the oxygen electrode at the electrode/electrolyte interface is higher than the equilibrium value due to injection of vacancies from the electrolyte; while under the electrolysis mode, the vacancy concentration near the electrolyte is lowered due to transport of vacancies into the electrolyte. For a current of 1.55 A/cm^2 in the electrolysis mode, significant depletion of vacancies is seen near the electrolyte interface, leading to high activation and concentration overpotentials of the oxygen electrode.

The activation (η_s) and concentration (η_c) overpotentials could be calculated from Equations (2) and (3) in Table 3-2, respectively. The parameter values used to compare with experimental data are summarized in Table 3-3.

Table 3-2 Model equations in dimensionless form for vacancy and adsorbed oxygen transport through porous oxygen electrode

Description	*Equation*	
Vacancy transport:	$\frac{d^2\hat{c}_v}{dx^2} = G_{v1}\hat{c}_v\hat{\theta} + \frac{G_{v1}\theta^{eq}}{\left(1-\theta^{eq}\right)}\hat{\theta} - \frac{G_{v1}}{\left(1-\theta^{eq}\right)}$	**(1)**
Activation overpotential:	$i = i_0\left(\frac{c_v(0)}{c_v{}^{eq}}\right)^{1-\beta}\left(e^{\frac{(1-\beta)\eta_s F}{RT}} - e^{\frac{-\beta\eta_s F}{RT}}\right)$	**(2)**
Concentration overpotential:	$\eta_c = \frac{RT}{2F}\ln\left(\frac{c_v(0)}{c_v{}^{eq}}\right)$	**(3)**
Boundary condition at the electrolyte interface:	$\frac{d\hat{c}_v}{dx} = \frac{i}{J^*}$	**(4)**
Boundary condition at the current collector interface:	$\frac{d\hat{c}_v}{dx} = 0$	**(5)**

Table 3-3 Independent parameters in the oxygen electrode model

Parameter	*Description*	*Value*
J^*	$J^* = \frac{2FD_v{}^{eff}c_v{}^{eq}}{L}$	0.095 A/cm^2
β		0.5
i_0		0.014 A/cm^2
G_{v1}	$G_{v1} = \frac{L^2 A_s}{D_v{}^{eff}}k_r\Gamma^{\pi}\theta^{eq}$	284.4
θ^{eq}		0.05

Shown in Figure 3-4 are the overpotentials as a function of total current density. Tafel type kinetics can be observed under fuel cell operating mode, while a saturation of total current density is seen in the electrolysis mode. The saturation is largely due to the reduction of $c_v(0)$, which corresponds to the vacancy concentration at the electrode/electrolyte interface, leading to a sharp increase in both the activation and concentration overpotentials.

To compare the oxygen electrode overpotential obtained from the model with the experimental value, the hydrogen electrode overpotential (calculated) was subtracted from the total experimental overpotential to yield experimental oxygen electrode overpotential as shown by the open symbols in Figure 3-5. Good agreement was observed between model and experiment data when irreversibility effects were included in the O_2 electrode model. A Tafel slope of F/RT was observed in the fuel cell mode at higher current densities, while a saturation current density of ~1.5 A/cm^2 was observed in the electrolysis mode. With the hypothesis that the saturation occurs primarily due to

vacancy depletion near the electrode/electrolyte interface as seen in Figure 3-3, the experimental data can be consistently explained.

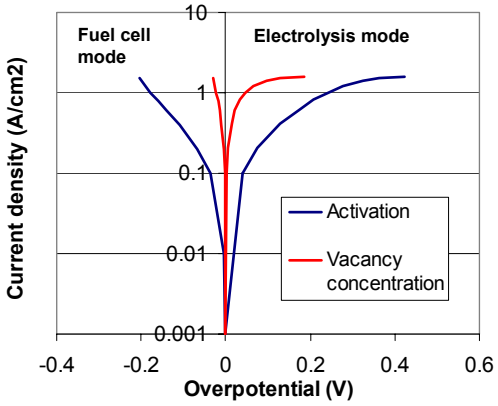

Figure 3-4 Activation and concentration overpotentials as a function of total current density

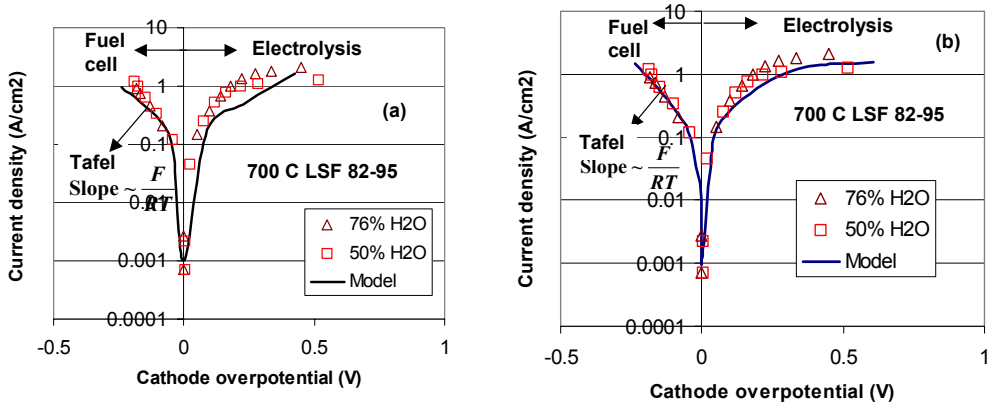

Figure 3-5 Comparison between model and experiment assuming a) reversible and b) irreversible O_2 electrode

With the asymmetric (or irreversible) oxygen electrode model, temperature impact on electrode reversibility has been investigated (Figure 3-6 and Figure 3-7). Figure 3-6a shows the comparison between model and experiment data at high temperature 850°C with the assumptions of symmetric and asymmetric oxygen electrodes. The asymmetric O_2 electrode assumption is seen to yield a better agreement with the experimental data, especially at high cell potentials in the electrolysis mode. The activation and concentration overpotentials were computed by solving for the vacancy concentration in the asymmetric electrode model as shown in Figure 3-6b.

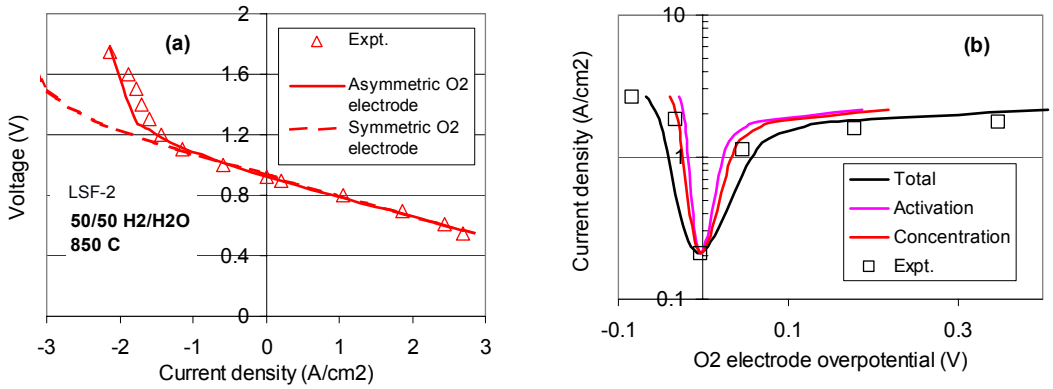

Figure 3-6 a) I-V curves and b) electrode overpotential contributions to the total O_2 electrode overpotential at 850°C

Shown in Figure 3-7 are the experimental data at 650°C in comparison with electrode models under the assumptions of symmetric and asymmetric oxygen electrodes. It appears that both models have reasonable fits to the experimental data and the oxygen electrode overpotentials (Figure 3-7b) exhibited symmetric characteristics within the current range examined (<1 A/cm^2). It is also seen that the oxygen electrode overpotential is largely dominated by the activation potential. At lower temperatures (650°C) in the electrolysis mode, the oxygen vacancies may be less depleted near the oxygen electrode/electrolyte interface because of low current density, leading to a more symmetric behavior. At higher temperatures (850°C), however, the high current density is largely limited by the depletion of vacancies near the oxygen electrode/electrolyte interface.

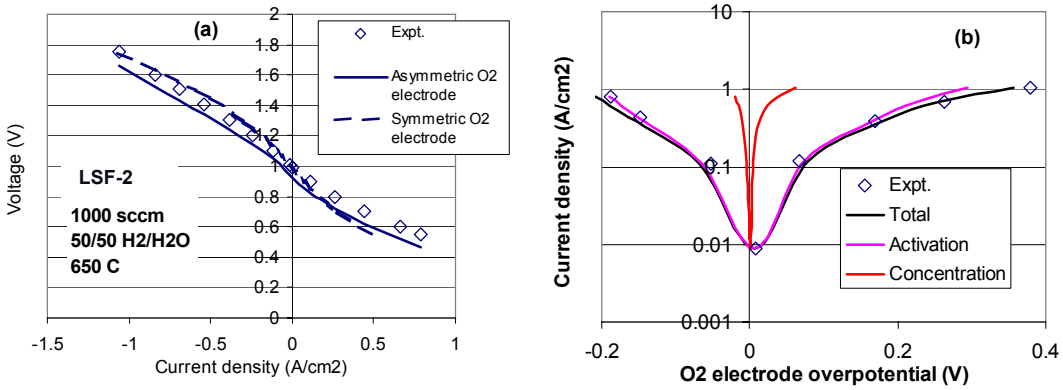

Figure 3-7 a) I-V curves and b) electrode overpotential contributions to the total O_2 electrode overpotential at 650°C

3.2.2.2 Hydrogen Electrode

Comparison between model and experiment performed on button cells at 800°C with $(La_{0.8}Sr_{0.2})_{0.95}FeO_{3-\delta}$ (LSF 82-95) as the oxygen electrode was shown in Figure 3-8. Fair agreement between the model and experiment was evident under fuel cell mode down to an operating voltage of 0.55 V. In the electrolysis mode, for operating potentials below 1.2 V, the model was also in good agreement with the experiment, while discrepancies could be seen above 1.2 V. One possible reason for this discrepancy is non-negligible steam utilization, which leads to a lower steam partial pressure on the surface of the hydrogen electrode than the inlet steam partial pressure, resulting in reduced current densities at a given operating potential. In order to assess the impact of steam utilization, the outlet flow rates of H_2O and H_2 were computed as $N_{H_2O}^{out} = N_{H_2O}^{in}\left(1 - U_f\right)$ and $N_{H_2}^{out} = N_{H_2}^{in} + N_{H_2O}^{in} U_f$, where N_i^{in} and N_i^{out} are the inlet and outlet flow rates of species i respectively, and $U_f = I/(2FN_{H_2O}^{in})$ is the steam utilization, I is the total cell current. Knowing the outlet flow rates of the species, we compute the corresponding molar fractions: $x_{H_2} = N_{H_2}^{out} / N_{Total}$ and $x_{H_2O} = N_{H_2O}^{out} / N_{Total}$. With the assumption of a well-mixed system, these molar fractions are then assumed to be the same as those on the cell surface. Since x_{H_2} and x_{H_2O} determine the total current I, the electrode model is run iteratively with the above equations to obtain self-consistent values for x_{H_2}, x_{H_2O} and I. The experimental maximum steam utilizations for 76%, 50% and 20% H_2O correspond to 8%, 15% and 33% respectively. Since the utilization was high enough for the 20% H_2O case, the performance was re-computed by accounting for steam utilization and the result was shown by the dashed line in Figure 3-8. The solid lines for 76% H_2O and 50% H_2O correspond to utilizations of 8% and 15% respectively.

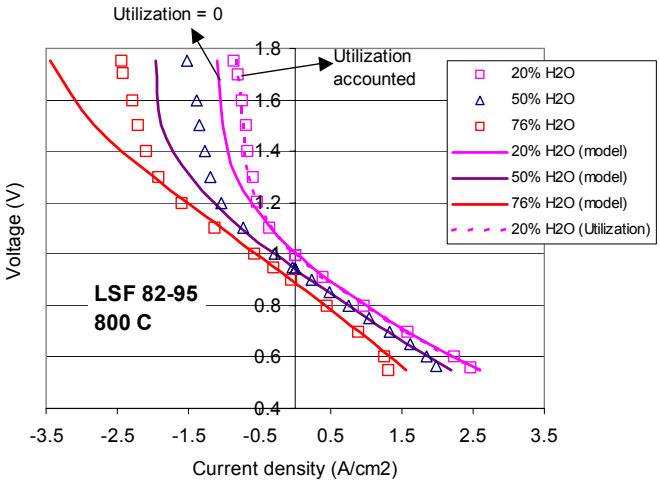

Figure 3-8 Comparison between model prediction and data for button cell tests performed with LSF82-95 oxygen electrode at 800°C.

It is apparent from the comparison that the cell behavior for 20% H_2O in the electrolysis mode can be explained via mass transport limitations associated with H_2O diffusion in the hydrogen electrode and the additional effect of the steam utilization. However, the above effects could not explain the cell behavior for operating potentials above 1.2 V with 50% and 76% H_2O feed. In fact, the calculated limiting current densities (hydrogen electrode) of 2.7 A/cm^2 and 4.2 A/cm^2 (for 50% and 76% H_2O respectively) are significantly different from the experimental values of 1.5 A/cm^2 and 2.5 A/cm^2, while the calculated limiting current density (1.1 A/cm^2) for 20% H_2O feed is comparable to the experimental value (0.9 A/cm^2). This suggests a possible rate-limiting transition from hydrogen electrode dominated behavior for 20% H_2O feed to oxygen electrode dominated behavior for 76% H_2O feed.

3.2.3 Electrode Microstructure

3.2.3.1 Oxygen Electrode Microstructure Optimization

Electrode microstructures can be optimized with optimal effective properties of the electrode. As an example, effective property calculation is illustrated in Figure 3-9 for a mixed ionic and electronic conductor (MIEC) electrode. The normalized conductivity follows a scaling law, decreasing with increasing porosity while the active bi-phase area (between MIEC and porosity) increases with increasing porosity in the range shown. The optimum porosity for optimal solid-gas bi-phase area is ~ 40%, but the electrode performance will be determined by a trade-off between both ionic conductivity and bi-phase area.

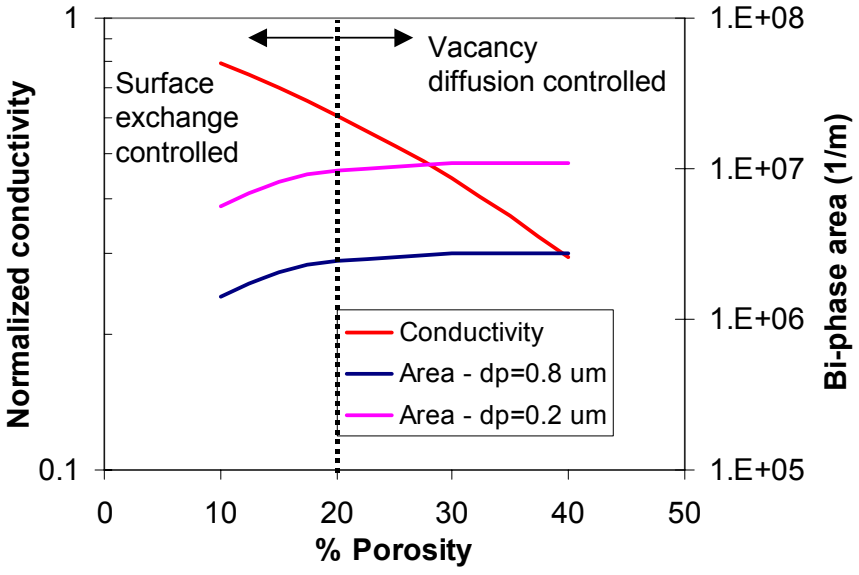

Figure 3-9 Dependence of effective conductivity and active bi-phase area on porosity.

Figure 3-10 shows the overpotential variations with porosity for given high and low current densities so as to be able to clearly identify the performance sensitivity with electrode microstructure. For smaller particle size (0.2 μm) in Figure 3-10a, which

corresponds to higher bi-phase area, the overpotential is typically low and exhibits less sensitivity to porosity. Relatively higher sensitivity is seen in the electrolysis mode, for a current density of -2 A/cm^2. Figure 3-10b shows a similar analysis, but with a larger particle size (0.8 μm). For a low current density of ±0.5 A/cm^2, the performance trend is similar to the case with the smaller particle size, but at a higher current density of ±1.4 A/cm^2, significantly larger variation of overpotential with porosity is seen, especially in the electrolysis mode. The reason for this is due to the fact that the above current density approaches the limiting current density in the electrolysis mode when porosity is >~40% or <~10%. At porosity >~40%, the conductivity is low and at porosity <~10%, the effective bi-phase area is low. The above analysis suggests that optimal electrode microstructure probably involves the choice of small particle sizes, so as to be able to reduce the overpotential as well as to mitigate the variation of performance with porosity.

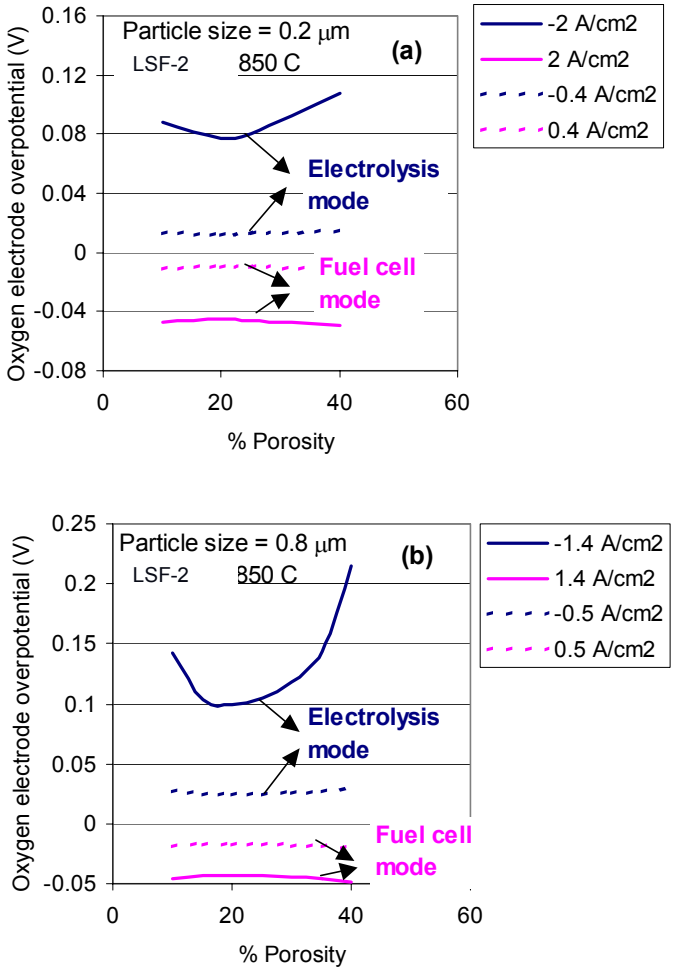

Figure 3-10 Calculated electrode overpotential for particle sizes of a) 0.2 μm, and b) 0.8 μm

3.2.3.2 Hydrogen Electrode Microstructure Optimization

The microstructure–performance relationship in the hydrogen electrode was established by computing "effective properties" using a statistical model. The microstructure parameters considered in this study were volume percentage of Ni, porosity, thickness and particle size. The calculations were performed on electrochemical active layer while fixing the microstructure properties of the support layer. Figure 3-11 shows the calculation of effective properties as a function of microstructure. The percolation boundary in Figure 3-11 bounds the region in which both Ni and YSZ phases are percolating. As the porosity increases, the percolation region for Ni and YSZ phases shrinks, until a porosity of ~55 % when only one of the solid phases is percolating, irrespective of the Ni volume fraction. The triple phase boundary (tpb) length shown in Figure 3-11a is seen to be at maximum for 50% Ni by solids for all porosities less than 55%. The optimal tpb length in the whole region is seen to occur for a porosity of ~ 15%. The normalized YSZ and Ni effective conductivities are shown in Figure 3-11 b and c, respectively. In the simulation region, the YSZ and Ni conductivities were seen to be maximal at a Ni volume of 20% and 80% respectively, and at a porosity of 5%.

The optimal microstructure of the hydrogen electrode is determined by a trade-off between the effective electrode properties such as tri-phase boundary length, YSZ effective conductivity, and diffusivities of H_2 and H_2O. The effective Ni conductivity is expected to weakly affect performance (far from the percolation threshold) since the bulk conductivity of Ni is significantly higher than that of YSZ. This trade-off then basically defines a region of interest, bounded by the dashed line in Figure 3-11, where we expect to see optimal performance. The effect of microstructure on performance (in both fuel cell and electrolysis modes) was evaluated in this region of interest, which covered a porosity ranging from 5% to 40% and Ni volume ranging from 25% to 60%.

Shown in Figure 3-12 is an example, estimating the hydrogen electrode overpotential as a function of the Ni volume and porosity. The thickness and particle size for the active layer were assumed to be 16 μm and 0.8 μm, respectively. Furthermore, the Ni and YSZ average particle sizes were assumed to be equal. For calculation of effective properties, the porosity was varied between 5% and 50%, while the % Ni volume was varied between 20% and 80%.

The performance was computed in terms of the electrode overpotential for fixed cell potentials of 0.7 V in the fuel cell mode and 1.3 V in the electrolysis mode. The conditions corresponded to 800°C operating temperature and 50%H_2/50%H_2O fuel composition. Regions I, II, and III are indicated by the dashed lines. Region I corresponds to the region where performance is limited by low triple phase boundary (tpb) length and poor mass transport of diffusing species (H_2 in the fuel cell mode and H_2O in the electrolysis mode). In Region II, performance is limited by both lower tpb length and lower electron conduction. In Region III, the performance is limited by low tpb length and poor ion conduction.

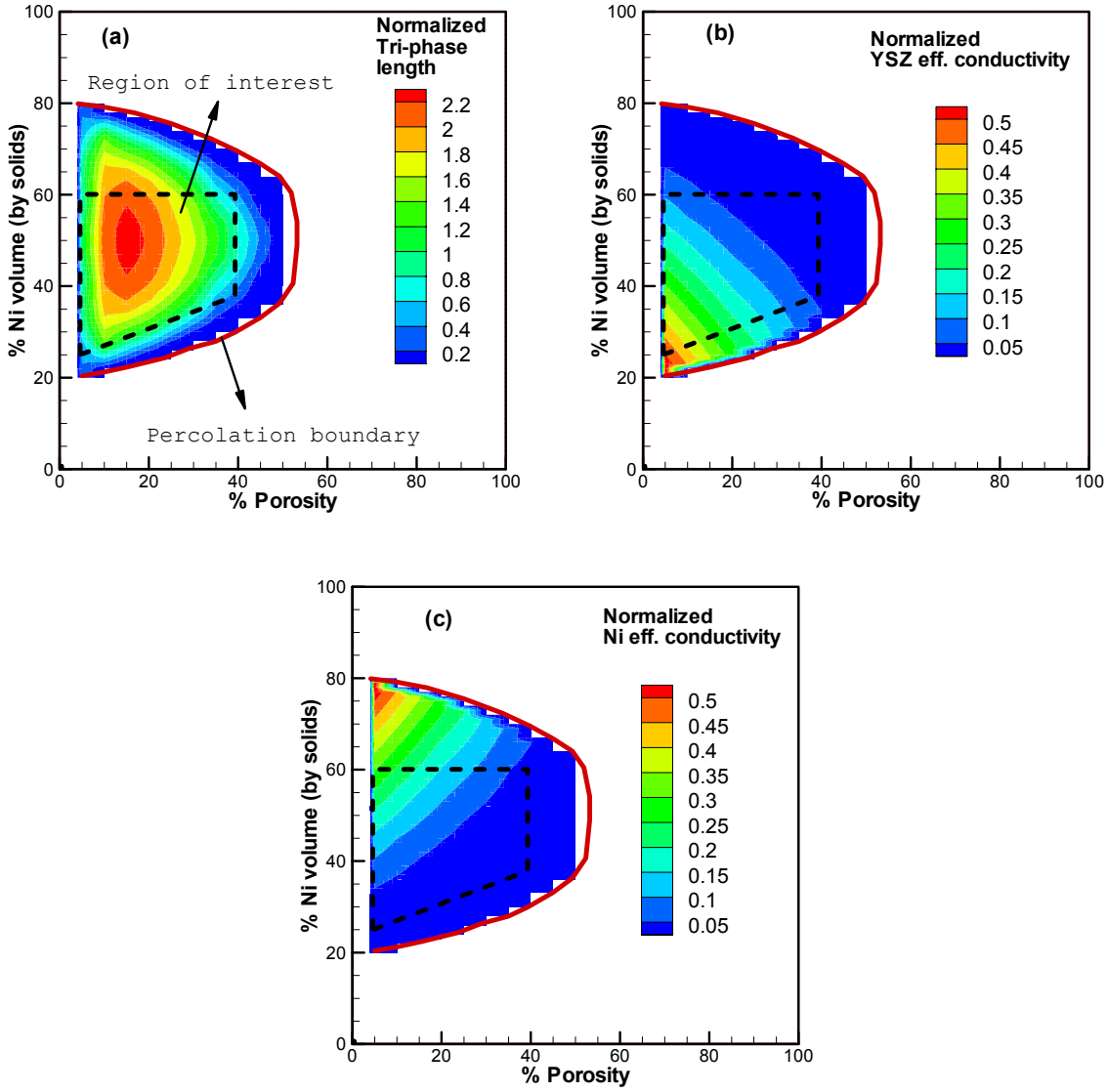

Figure 3-11. Dependence of a) Tri-phase boundary length, b) YSZ effective conductivity, and c) Ni effective conductivity on Ni volume and porosity

The optimal performance is predicted to occur at ~10% porosity and ~35vol% Ni with given particle size and thickness in the active layer for fuel cell mode (Figure 3-12a). For the electrolysis mode in Figure 3-12b, the optimal performance was predicted to occur at ~20% porosity and ~35vol% Ni. The higher optimal porosity in the electrolysis mode compared to fuel cell mode is likely due to different mass transport characteristics of H_2 and H_2O, since H_2O has a lower effective diffusivity than H_2.

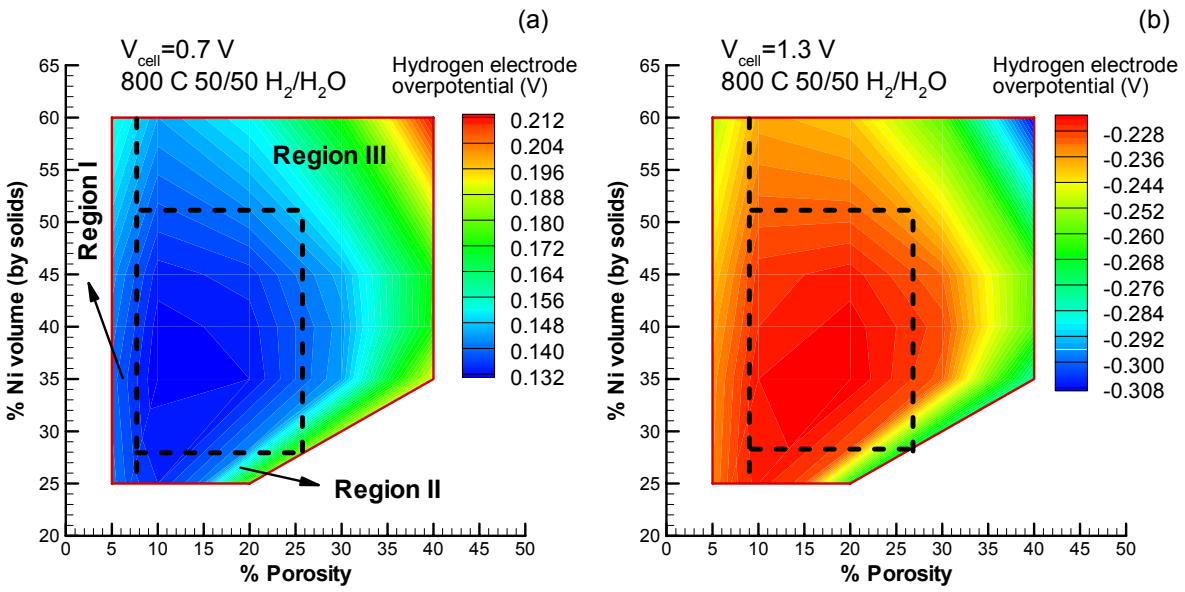

Figure 3-12 Hydrogen electrode performance in a) fuel cell mode, and b) electrolysis mode with thickness of 16 μm and average particle size of 0.8 μm

In order to assess the impact of varying particle size and thickness in the active layer, performance was evaluated for particle sizes of 0.4 and 1.6 μm and thicknesses of 8 and 32 μm, which correspond to a factor of two above and below the baseline values used in Figure 3-12. The fuel composition was fixed at 50%H_2/50%H_2O and the temperature was 800°C. Figure 3-13 shows the results in the fuel cell mode at an operating voltage of 0.7 V. Optimum performance for the run matrix was observed for a thickness of 8 μm and a particle size of 0.4 μm. For a particle size of 0.4 μm, a larger thickness shifted the optimum porosity to ~20-30% while a smaller thickness gave an optimal porosity range of 10-20%. The effect of thickness on performance was seen to be weak for the larger particle size of 1.6 μm, largely due to lower mass transport limitations from larger pore sizes.

Figure 3-14 shows the results in the electrolysis mode at an operating voltage of 1.3 V. A trend similar to the fuel cell mode is observed, except that the predicted optimal porosities are higher than those in the fuel cell mode by about 5%. The optimal Ni volume is similar to that in the fuel cell mode, typically ranging from 30-40%. Similar to the fuel cell mode, a thinner active layer with smaller particle size is predicted for lower overpotentials.

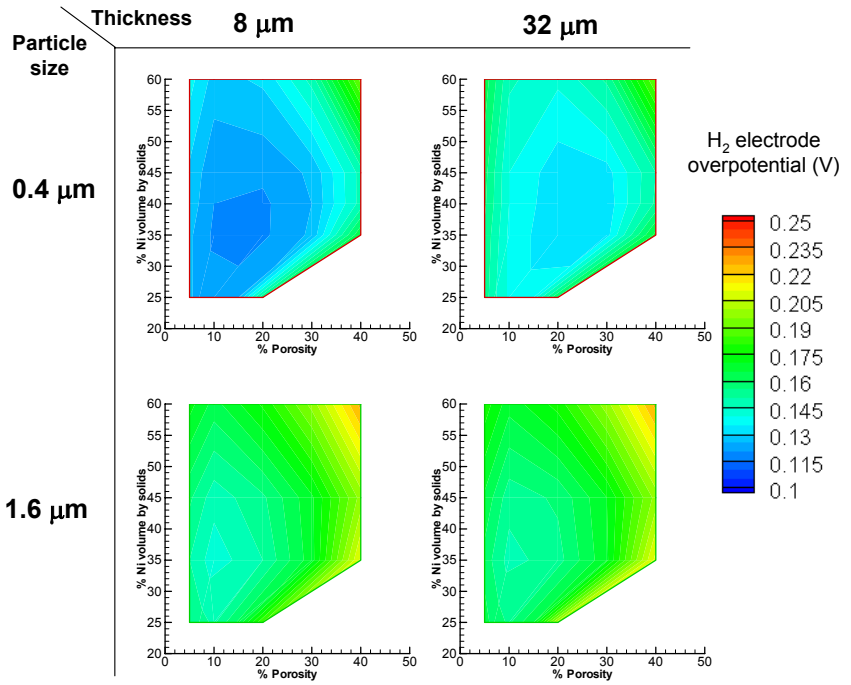

Figure 3-13 Hydrogen electrode overpotential dependence on active layer thickness and particle size in the fuel cell mode at an operating voltage of 0.7 V

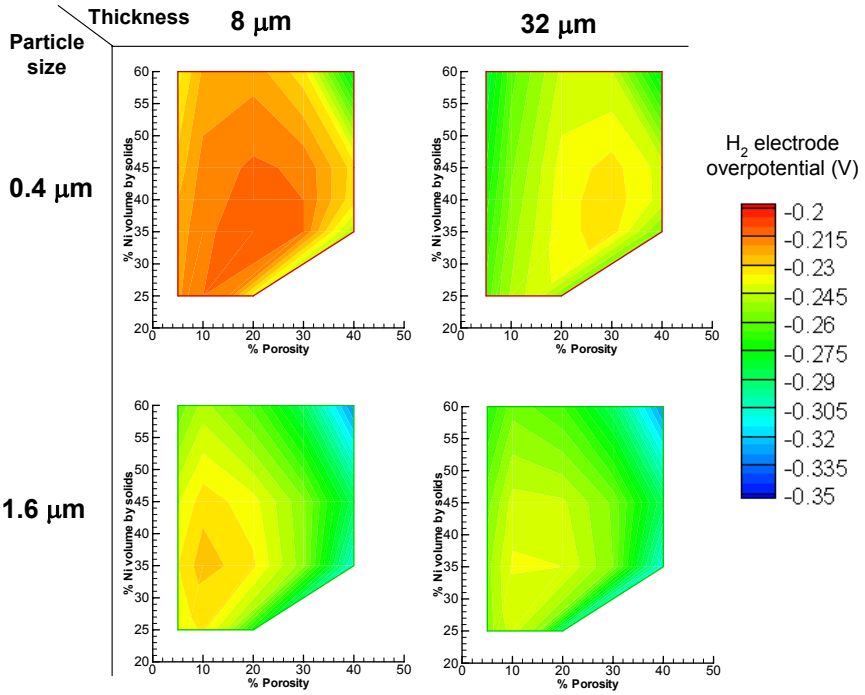

Figure 3-14 Hydrogen electrode overpotential dependence on active layer thickness and particle size in the electrolysis mode at an operating voltage of 1.3 V

3.2.4 On-cell Internal Reforming

The internal reforming model solves for formation and transport of charged and neutral species through the thickness of a hydrogen electrode. The model equations are shown in Table 3-4. Equations (6) and (7) describe the transport of electrons and ions through their corresponding potentials. Equation (8) describes the kinetics of charge transfer given by the Butler-Volmer equation. C_r^{ref} and C_p^{ref} correspond to the reference state concentrations of reactants and products respectively. The overpotential η appearing in Equation (8) was computed as $\eta = V_i - V_e - E_{ref}$, where E_{ref} is the reference potential. The reference potential in the hydrogen electrode was computed based on species concentrations at the hydrogen electrode/electrolyte interface, while at the oxygen electrode, the reference potential was set to zero. Equation (9), describes the transport and reaction of neutral species through the porous electrode. The first term on the right hand side denotes electrochemical generation or consumption of species while the second and third terms represent consumption or generation through reforming (R_{ref}) and shift (R_{sh}) reactions respectively with corresponding stoichiometric coefficients ν_i and π_i. Literature reforming and shift kinetics on a Ni catalyst were used [10]. The multicomponent diffusive flux computed from Equations (10), (11) and (12) is given by the dusty gas model [11] accounting for species diffusion through a porous medium. The effective properties of the porous medium such as the ionic/electronic conductivities σ_{io}^{eff}, σ_{el}^{eff} and the tri-phase area A were computed from a statistical model.

The boundary condition for species transport was incorporated by specifying a fixed value of the surface concentration of all neutral species. An internal boundary was numerically setup on electrode/electrolyte interfaces where the flux of neutral species was set to zero (no cross leakage). Internal reforming across the thickness of the hydrogen electrode and along the gas channels on the hydrogen electrode was analyzed independently.

Mole fractions of methane and hydrogen across the thickness of the hydrogen electrode are shown in Figure 3-15. Surface composition of the fuel was assumed to be 20% CH_4 and 30% H_2O balanced with N_2. Monotonic increase in H_2 mole fraction is seen under open circuit voltage conditions, while a non-monotonic profile is seen while drawing current. The electrochemical reaction consumes H_2 near the electrode/electrolyte interface, leading to the non-monotonic profile.

A “single channel” 1D model was developed to solve for the spatial variation of CH_4, H_2O, H_2, CO, CO_2 and N_2 along the length of the hydrogen electrode channel and the results are shown in Figure 3-16. The inlet conditions correspond to a fuel composition of 20% CH_4 and 30% H_2O balanced with N_2 and a temperature of 800°C. A fuel utilization of 80% and an operating voltage of 0.6 V were assumed. The average current density of 0.29 A/cm^2 computed from the model agrees well with the measured average current density of 0.275 A/cm^2. A rapid consumption of CH_4 and H_2O due to reforming is seen near the fuel inlet (Figure 3-16a), leading to an increase in H_2 and CO

concentrations and a corresponding increase in the local current density as seen in Figure 3-16b. Further downstream along the channel, when CH_4 is almost depleted, H_2 and CO concentrations decrease due to electrochemical consumption. As CH_4 is consumed, the consumption rate also drops and so does the current density due to depletion of H_2 and CO.

Table 3-4 Model equations describing charged and neutral species transport through the porous electrodes.

Description	*Equation*	
Electron Transport:	$\frac{d}{dx}\left(\sigma_{el}^{\ eff}\frac{dV_{el}}{dx}\right)=\pm Ai_n$	(6)
Ion Transport:	$\frac{d}{dx}\left(\sigma_{io}^{\ eff}\frac{dV_{io}}{dx}\right)=\mp Ai_n$	(7)
Charge Transfer Current:	$i_n=i_0\left\{\frac{C_r}{C_r^{ref}}\exp\left(\frac{\beta n_e F\eta}{RT}\right)-\frac{C_p}{C_p^{ref}}\exp\left(-\frac{(1-\beta)n_e F\eta}{RT}\right)\right\}$	(8)
Species Transport:	$\varepsilon\frac{\partial c_i}{\partial t}+\nabla\cdot\mathbf{N}_i=\pm\frac{Ai_n}{n_e F}+\nu_i R_{ref}+\pi_i R_{sh}$	(9)
Net Species Flux:	$\mathbf{N}_i=\mathbf{J}_i+x_i\mathbf{N}_T$	(10)
Multicomponent Diffusive Flux:	$\sum_{j\neq i}\frac{x_j\mathbf{J}_i-x_i\mathbf{J}_j}{\Delta_{ij}}=\frac{-p}{RT}\nabla x_i-\frac{x_i}{RT}\left(1-\frac{1/D_i^{\ eff}}{\sum_s x_s/D_s^{\ eff}}\right)\nabla p$	(11)
Total Flux:	$\mathbf{N}_T=\sum_i\mathbf{N}_i=\frac{\sum_{s=1}^{N_c}\frac{\mathbf{J}_s}{D_s^{\ eff}}}{\sum_{s=1}^{N_c}\frac{x_s}{D_s^{\ eff}}}-\frac{1}{RT}\left(\frac{Bp}{\mu}+\frac{1}{\sum_{s=1}^{N_c}\frac{x_s}{D_s^{\ eff}}}\right)\nabla p$	(12)

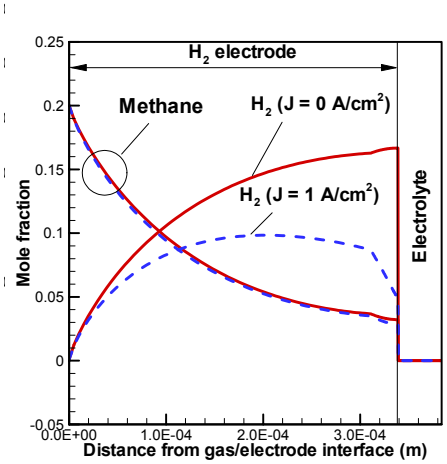

Figure 3-15. Spatial variation of methane and hydrogen along the thickness of the hydrogen electrode for current densities of 0 and 1 A/cm^2

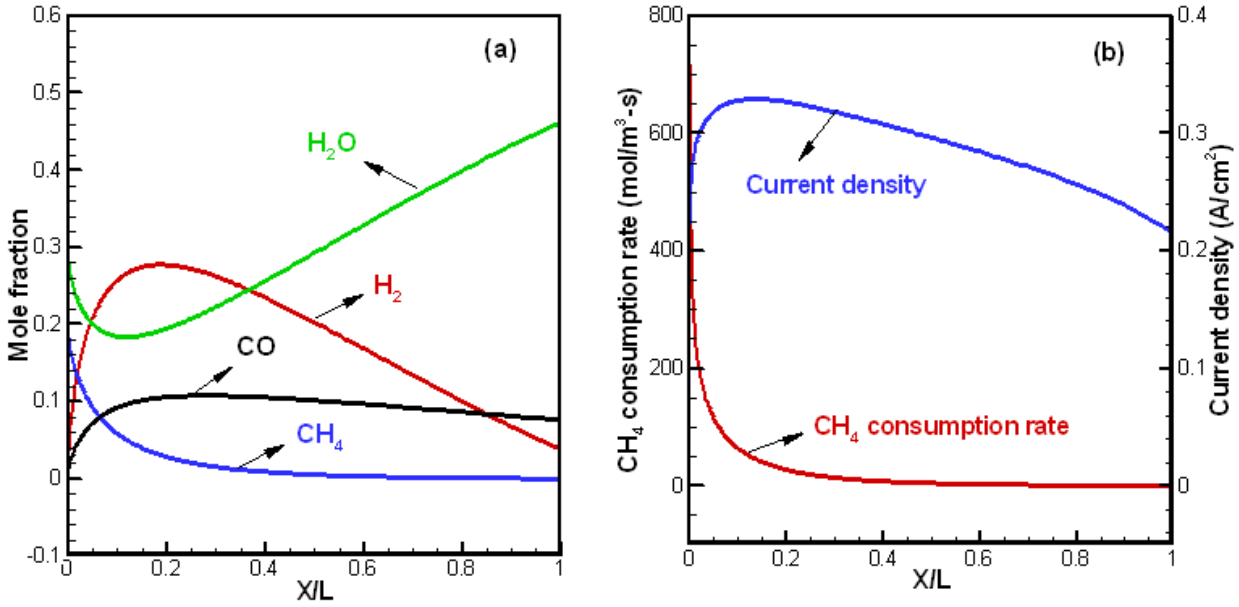

Figure 3-16. a) Spatial variation of fuel composition along the length of the fuel channel and b) the corresponding consumption rate and local current density. The inlet fuel composition was taken to be 20% CH_4 and 30% H_2O. The fuel utilization was calculated to be 80%. X is the distance from the fuel inlet along the channel and L is the total channel length (=1.067 m).

Evaluation of on-cell internal reforming has been conducted through experiments with gas composition analysis as well as the electrochemical performance measurement. Gas compositions were analyzed with a calibrated mass spectrometer. After the calibration process, the measured values (outlet) with the mass spectrometer were seen to agree well with set values (inlet) (Table 3-5).

Table 3-5 Comparison of the inlet and outlet compositions measured by the mass spectrometer after calibration.

	Inlet	Outlet
Ar	22.26%	22.90%
CO2	11.13%	11.20%
H2	22.26%	22.10%
H2O	22.08%	21.10%
CH4	11.13%	10.60%
CO	11.13%	11.60%

The on-cell internal reforming capability evaluation was conducted with a 1" testing fixture (Figure 3-17) under open circuit condition. The control volume for establishing a reforming model platform is also shown. The size of the control volume in the model only affects the transient solution as the residence time of the fuel mixture changes with the change in the control volume size. However, since the steady state solution is of interest in this case, the control volume size is largely arbitrary. Mass conservation equations were set up to solve for species mole fractions X_i (i = CH_4,

H_2O, CO, CO_2 and H_2) in the control volume accounting for reforming and shift reactions in the hydrogen electrode.

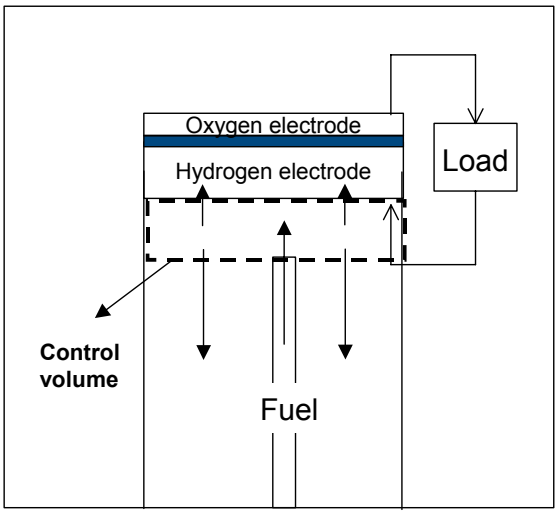

Figure 3-17 Experimental setup for on-cell internal reforming characterization

The nominal operating temperature is 800°C and the total inlet flow rate is 200 sccm. In order to determine if the inlet and outlet lines contributed to any reforming or gas-shift reactions, experiments were performed on a "blank cell" which consisted of an alumina disk that was sealed to the mounting tube. The outlet gas composition was then monitored to see if it differed from the inlet composition. The outlet composition was measured for three furnace temperatures of 200, 500 and 800°C. The inlet compositions were about 42% H_2O/17% CO/balance Ar for evaluating the gas-shift reactions, and 42% H_2O/17% CH_4/ balance Ar for evaluating reforming reactions in the lines. The difference between the inlet and outlet compositions was seen to be within 2% for the range of temperatures studied, suggesting no appreciable reforming or gas-shift reactions occurring in the lines.

A button cell consisting of Ni/YSZ hydrogen electrode and LSF-2 oxygen electrode then replaced the blank cell. The inlet fuel mixture consisted of only CH_4 and H_2O balance with buffer gas argon. The constraints imposed on the selection of inlet mole fractions are that the steam/carbon ratio is at least two and the sum of the inlet mole fractions (including the buffer gas) is equal to one. Hence, the colored contour region in Figure 3-18 defined the space of inlet CH_4 and H_2O mole fractions. The range of inlet mole fractions in this region is between 3% and 33% for CH_4 and 52% and 83% for H_2O. This range was also seen to provide stable values of outlet composition as measured by the mass spectrometer. Good qualitative agreement was observed between the model and experiment as shown in Figure 3-18, with the experimental trend captured by the model. Increase in inlet CH_4 fraction was seen to increase CH_4 reforming rate, and the outlet CH_4 mole fraction was seen to be less sensitive to inlet H_2O mole fraction. In the range of compositions investigated, a maximum methane conversion of 47% was measured. It is to be noted that the measured conversion is relatively low compared to equilibrium conversion, owing to the fact that the total inlet

flow rate was 200 sccm for 1" button cell, causing methane conversion to be kinetically controlled.

Electrochemical performance was also evaluated with 1" button cells (ferritic stainless steel, FSS-1, was used as current collectors). The measured cell performance is shown in Figure 3-19. Performance curves were obtained by varying the inlet mole fraction of CH_4 for a fixed inlet mole fraction of H_2O. The inlet H_2O mole fractions of 52.1%, 66.7% and 83.3% were chosen to make the measurement as shown in Figure 3-19a, b and c, respectively. For a given percentage of H_2O, the OCV and performance increased with increasing $\%CH_4$, with a power density of ~ 490 mW/cm^2 at 0.7 V for an inlet fuel composition of 52.1% H_2O and 25.8% CH_4. The performance was also seen to increase with decreasing $\%H_2O$. Since it was not easy to control the low flow rates for high fuel utilizations in 1" button cells, the electrochemical performance of on-cell internal reforming has been further characterized with large footprint cells.

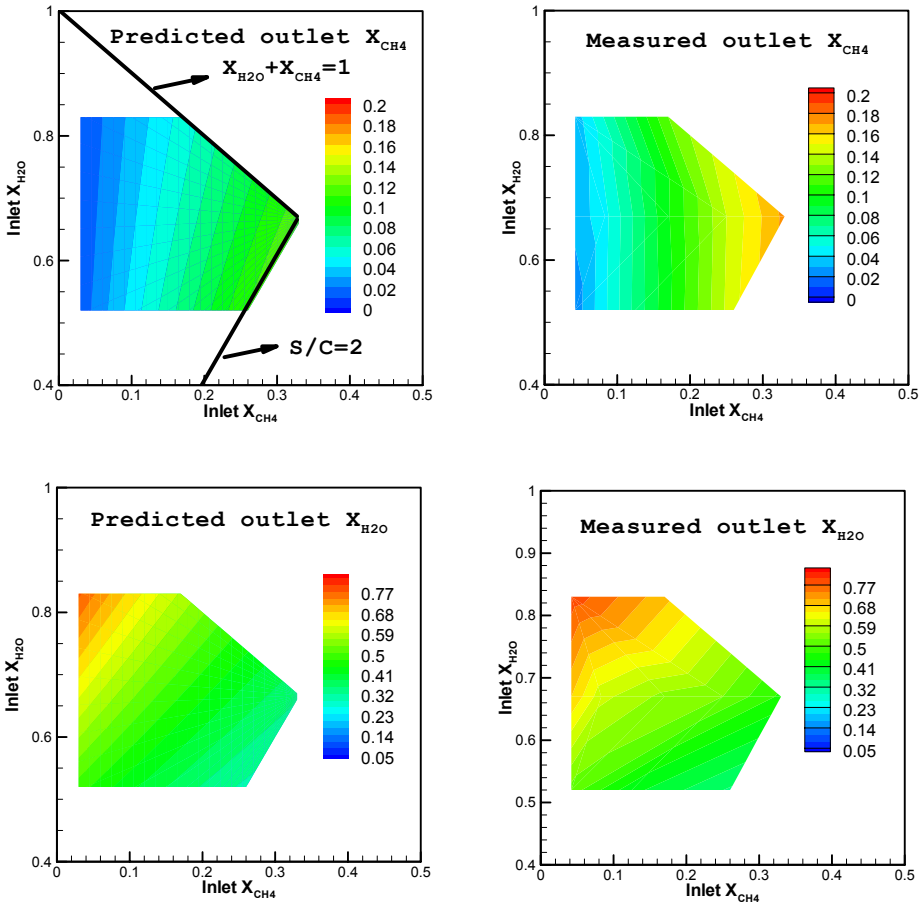

Figure 3-18 Comparison between model and experimental mole fraction of CH_4 and H_2O at the outlet as a function of inlet CH_4 and H_2O mole fractions.

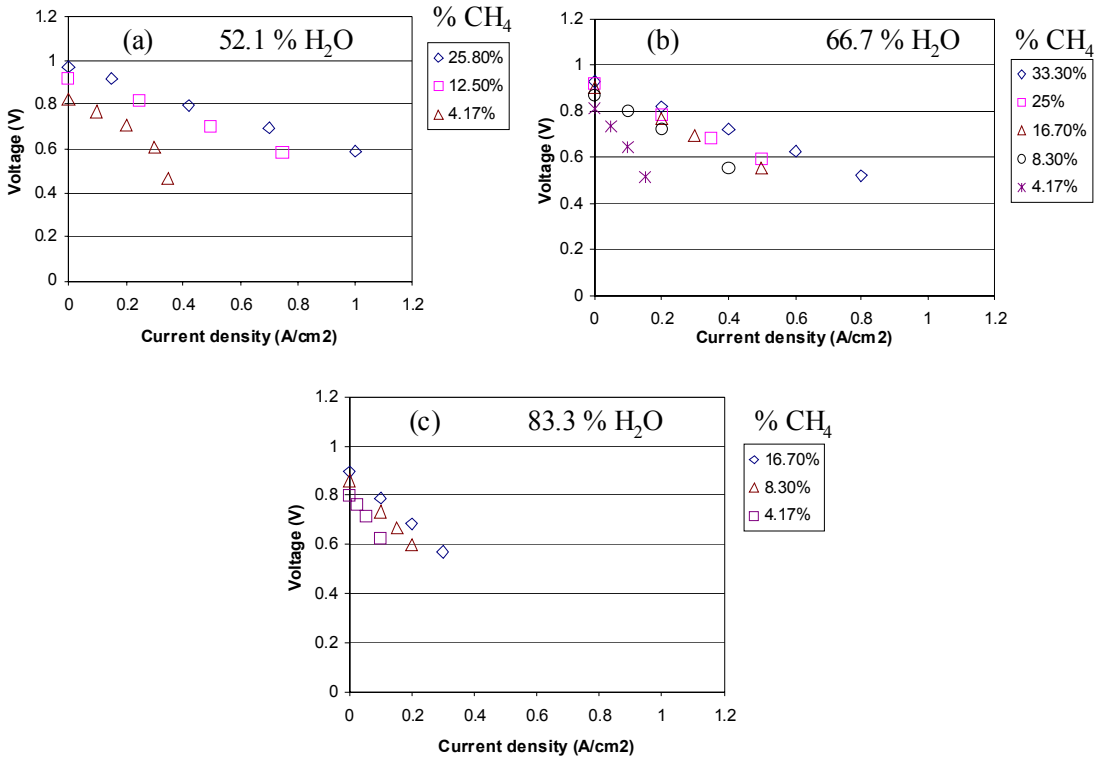

Figure 3-19. Measured button cell performance as a function of inlet mole fractions of CH_4 and H_2O at 800°C and a total flow rate of 200 sccm

3.3 ELECTRODE DEVELOPMENT

3.3.1 Oxygen Electrode Materials Selection

Five oxygen electrode candidates were selected as the candidates. Two LSM-based materials were chosen (denoted as LSM-1, LSM-2) and they were made into composite oxygen electrodes with 8YSZ. Three mixed ionic electronic conducting (MIEC) materials were selected: $(La_{0.8}Sr_{0.2})_{0.95}FeO_3$ (LSF82-95), another Sr-doped lanthanum ferrite (LSF-2), and one $(La_xSr_{1-x})_yCo_zFe_{1-z}O_3$ (LSCF-1). The MIEC electrodes were single-phase materials. The performance of the candidate materials was evaluated using 1-inch button cell tests under both fuel cell and electrolysis mode. Two different oxygen electrode attachments were used. A gold mesh attachment was used to evaluate the intrinsic materials performance of the electrode (Figure 3-20 and Figure 3-21). A stainless steel interconnect (GE13L) attachment was used to evaluate the impact of the interconnect on the electrode performance. The stability of the electrodes in fuel cell and electrolysis mode was screened for up to 100 hours.

Oxygen electrodes were fabricated on 1-inch button cells using screen-printing and subsequent sintering. Sintering temperatures varied according to the compositions and were chosen for optimized surface area of the electrode while providing good interparticle adhesion. LSM-containing electrodes were fabricated directly on the YSZ

electrolyte surface. When the MIEC electrodes were used, an interlayer of 20 mol% samaria-doped ceria (SDC) of ~5 microns in thickness was fabricated on top of the YSZ electrolyte.

Electrochemical performance was measured in button cell tests. H_2 humidified through a temperature-controlled water bubbler was used on the fuel side. The H_2 flow rate was 200 sccm and humidification of 3%, 50% and about 80% was used. Another fuel condition (134 sccm H_2/ 75 sccm N_2 humidified at 3%) was also used. Air at 1 slpm was delivered to the oxygen electrode. The sample was held in a furnace at temperatures between 700 and 800°C. A series of current-voltage or IV curves were taken at three different temperatures 800 ºC, 750 ºC, and 700 ºC and three different steam contents.

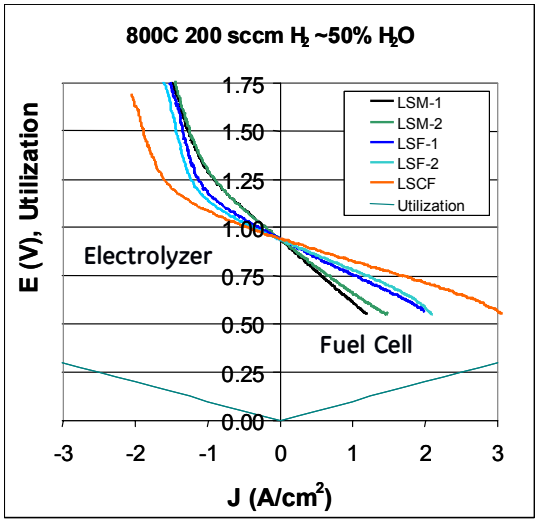

Figure 3-20. Oxygen electrode performance screening with Au screen as the current collectors

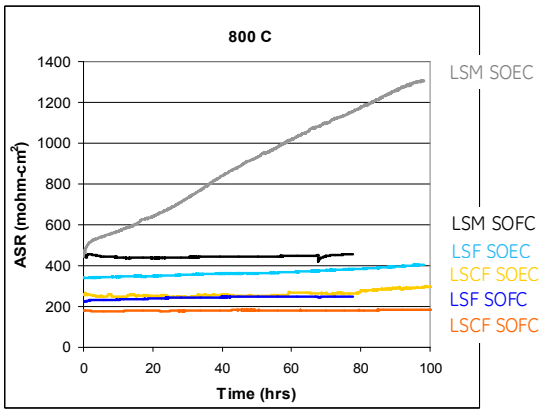

Figure 3-21. Performance stability of varied oxygen electrode with Au as current collectors

Performance and stability comparisons for the five oxygen electrodes with Au mesh and GE13L attachments are given in Table 3-6 to Table 3-11. An analysis of variance (ANOVA) was performed on the current densities measured in fuel cell and electrolysis mode at the reversible condition of 50% H_2/ 50% H_2O. As measured with Au mesh attachments, there was a significant difference in current density in both fuel cell and electrolysis mode for the five compositions. LSCF-1 was the best composition, the two LSF compositions were next best and the two LSM compositions were the worst. With GE13L attachments, no statistically significant difference was observed, although the mean current density in both modes was the highest for the LSCF-1 composition.

Stability of the five compositions is given in Table 3-8 and Table 3-11. Since only one sample was measured for each condition, statistical conclusions couldn't be drawn. However, the five compositions had similar stability with Au mesh attachments in fuel cell mode (Table 3-8), although LSM-2 and LSCF-1 appeared to be better. In electrolysis mode, the LSM compositions were the worst. The LSCF-1 and LSF82-95 compositions were the most stable in electrolysis mode. The LSF-2 composition showed an intermediate stability.

With GE13L attachments in fuel cell mode (Table 3-11), the stability of the LSCF-1 and LSM compositions was similar. The LSF82-95 composition had a very high degradation rate, probably caused by the attachment agent. In electrolysis mode, the two LSM compositions degraded the fastest. LSCF-1 was the most stable, with a degradation rate that was lower than that in fuel cell mode. The LSF82-95 showed intermediate stability in electrolysis mode with GE13L attachments.

In all respects, the LSCF-1 composition had the highest performance and the best stability. In almost all measurements, the LSM compositions had the lowest performance and showed catastrophically rapid degradation in electrolysis mode. The LSF compositions were intermediate in performance, showing some variability. Based on the performance screening, LSCF-1 was down selected as the oxygen electrode for further improvement.

Table 3-6 Current density for oxygen electrode compositions on button cells in fuel cell and electrolysis modes using Au mesh attachments

800 °C	200 sccm H_2/50% H_2O		134 sccm H_2/75 sccm N_2/3% H_2O	200 sccm H_2/ 3% H_2O	200sccm H_2/ 80% H_2O
Au mesh	J at 0.7V (A/cm^2)	J at 1.3 V (A/cm^2)	J at 0.7V (A/cm^2)	J at 0.7V (A/cm^2)	J at 1.3 V (A/cm^2)
LSM-1	0.69 ± 0.06	0.94 ± 0.10	0.77 ± 0.08	0.91 ± 0.13	1.30 ± 0.07
LSM-2	0.79 ± 0.08	0.94 ± 0.08	0.92 ± 0.12	1.07 ± 0.13	1.32 ± 0.03
LSF82-95	1.41 ± 0.13	1.19 ± 0.00	1.37 ± 0.06	1.64 ± 0.01	2.02 ± 0.13
LSF-2	1.59 ± 0.14	1.50 ± 0.23	1.69 ± 0.21	2.12 ± 0.17	2.29 ± 0.21
LSCF-1	2.05 ± 0.10	1.52 ± 0.29	2.09 ± 0.28	2.54 ± 0.42	2.40 ± 0.80

Table 3-7 Area specific resistance (ASR) for oxygen electrode compositions on button cells in fuel cell (at 0.7V) and electrolysis (at 1.3V) modes using Au mesh attachments

800 °C	200 sccm H_2/50% H_2O		134 sccm H_2/75 sccm N_2/3% H_2O	200 sccm H_2 /3% H_2O	200 sccm H_2/ 80% H_2O
Au mesh	ASR at 0.7V (ohm-cm^2)	ASR at 1.3 V (ohm-cm^2)	ASR at 0.7V (ohm-cm^2)	ASR at 0.7V (ohm-cm^2)	ASR at 1.3 V (ohm-cm^2)
LSM-1	348	386	473	407	325
LSM-2	301	385	390	341	321
LSF82-95	167	306	257	217	210
LSF-2	157	274	226	176	198
LSCF-1	170 ± 34	269 ± 16	170 ± 34	141 ± 33	221 ± 94

Table 3-8 Stability of ASR measured under constant voltage conditions using Au mesh attachments for fuel cell and electrolysis modes normalized per 100 hours

800 °C Au mesh	0.7V 200 sccm H_2 ASR change (mohm-cm^2/100 hrs)	1.3 V 100 sccm H_2/ 50% H_2O ASR change (mohm-cm^2/100 hrs)
LSM-1	22	840
LSM-2	3	440
LSF82-95	21	67
LSF-2	24	190
LSCF-1	5	62

Table 3-9 Current density for oxygen electrode compositions on button cells in fuel cell and electrolysis modes using GE13L stainless steel attachments

800 °C	200 sccm H_2/50% H_2O		134 sccm H_2/75 sccm N_2/3% H_2O	200 sccm H_2/ 3% H_2O	200sccm H_2/ 80% H_2O
GE13L	J at 0.7V (A/cm^2)	J at 1.3 V (A/cm^2)	J at 0.7V (A/cm^2)	J at 0.7V (A/cm^2)	J at 1.3 V (A/cm^2)
LSM-1	0.55 ± 0.06	0.84 ± 0.09	0.67 ± 0.04	0.74 ± 0.03	1.09 ± 0.17
LSM-2	0.57	0.81	0.65	0.72	1.11
LSF82-95	0.63 ± 0.02	0.68 ± 0.20	0.79 ± 0.06	0.92 ± 0.10	0.99 ± 0.57
LSCF-1	1.27 ± 0.59	1.27 ± 0.26	1.19 ± 0.32	1.35 ± 0.40	1.75 ± 0.40

Table 3-10 ASR for oxygen electrode compositions on button cells in fuel cell and electrolysis modes using GE13L stainless steel attachments

800 °C	200 sccm H_2/50% H_2O		134 sccm H_2/75 sccm N_2/3% H_2O	200 sccm H_2 /3% H_2O	200 sccm H_2/ 80% H_2O
GE13L	ASR at 0.7V (ohm-cm^2)	ASR at 1.3 V (ohm-cm^2)	ASR at 0.7V (ohm-cm^2)	ASR at 0.7V (ohm-cm^2)	ASR at 1.3 V (ohm-cm^2)
LSM-1	439	429	552	503	388
LSM-2	423	444	563	521	381
LSF82-95	370	664	463	405	512
LSCF-1	277	333	374	342	288

Table 3-11 Stability of ASR measured under constant voltage conditions for fuel cell and electrolysis modes with GE13L attachments normalized per 100 hours.

800 °C GE 13L	0.7V 200 sccm H_2 ASR change (mohm-cm^2/100 hrs)	1.3 V 100 sccm H_2/ 50% H_2O ASR change (mohm-cm^2/100 hrs)
LSM-1	180	730
LSM-2	240	860
LSF82-95	1080	540
LSCF-1	198	150

3.3.2 Stability Evaluation under Dual Mode

Degradation behavior of the selected oxygen electrode system, LSCF-1, was measured with 1-inch button cell tests in fuel cell, electrolysis and cyclic modes. A stainless steel interconnect (GE13L) attachment was used for both hydrogen electrode and oxygen electrode current collector. A rig with 6 button cells with a common fuel manifold was used. The H_2 flow rate was 200 sccm/cell and humidification of 50% was used. Air at 1 slpm was delivered to the oxygen electrode. The samples were held in a furnace at 800°C. Potential was applied using a multichannel potentiostat to achieve one of three conditions: cell voltage of 0.7V (fuel cell mode), 1.3V (electrolysis mode), or 12 hour cycles of 1.3V and 0.7V (cyclic mode).

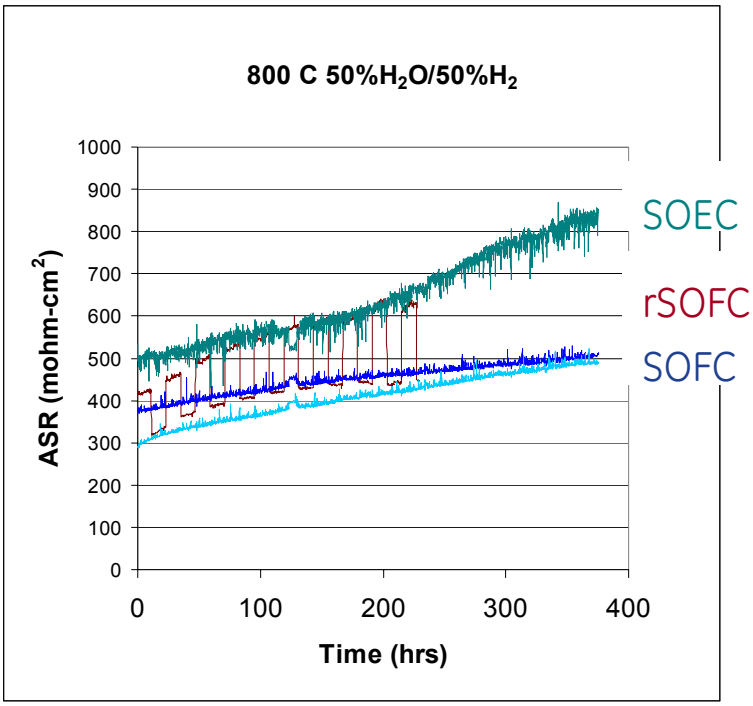

Figure 3-22. Typical ASR changes of cells operated under varied operating modes: fuel cell mode (SOFC), electrolysis mode (SOEC) and cyclic mode (rSOFC).

Two tests were run. In test 6G1, two of the six cells were run for 230 hours with one in fuel cell mode and one in cyclic mode. The other four cells did not meet

performance or stability criteria for testing. The second test was 6G3 in which five of the six cells were run for 375 hours. Two cells were in fuel cell mode, two cells in electrolysis mode and one in cyclic mode.

The typical ASR change with time under power generation mode, electrolysis mode, and cyclic mode is shown in Figure 3-22. The average ASR change per 100 hours is given in Table 3-12. The average change was about 45 mohm-cm^2/100 hours in fuel cell mode and a slightly higher degradation rate in electrolysis mode of 78 mohm-cm^2/100 hours. In a comparison of all of the data, there was no statistical difference among the steady state fuel cell, steady state electrolysis, cyclic fuel cell and cyclic electrolysis degradation rates.

Table 3-12 Degradation rates for cells with LSCF-1 oxygen electrode and GE-13L current collectors

Mode	0.7V 200 sccm H_2/ 50% H_2O ASR change (mohm-cm^2/100 hrs)	1.3 V 200 sccm H_2/ 50% H_2O ASR change (mohm-cm^2/100 hrs)	Test ID	Duration (hours)
Steady state	46	---	6G1-4	230
Cyclic	59	94	6G1-5	230
Steady state	35	---	6G3-1	375
Steady state	53	---	6G3-5	375
Steady state	---	77	6G3-3	375
Steady state	---	78	6G3-4	319
Cyclic	22	16	6G3-6	375
Average				
Steady state	45 ± 9	78 ± 1		
Cyclic	40 ± 26	55 ± 55		

3.3.3 Processing Improvement

In the initial performance and stability screening, the processing temperature for LSCF-1 electrode was 1025°C. Its selection was based on qualitative microstructural examination of test coupons. For potential performance improvement, sintering temperatures of 925, 975, and 1025°C were evaluated.

Current densities are given in Table 3-13 for LSCF-1 electrodes sintered at 1025°C (initial study in 3Q05) and at three levels in this study 925, 975, and 1025°C. It can be seen from the table that the highest current densities were obtained for the specimens fabricated in 3Q05. In the present study the highest current densities were observed for the lowest sintering temperature, which were slightly lower than those for the 3Q05 specimens. The 1025 °C sintering temperature in the present study had a significantly lower performance than the 3Q05 specimens.

Table 3-13 Current density for LSCF-1 oxygen electrodes on button cells in fuel cell and electrolysis modes.

800 °C	200 sccm H_2/50% H_2O		134 sccm H_2/75 sccm N_2/3% H_2O	200 sccm H_2/ 3% H_2O
	J at 0.7V (A/cm^2)	J at 1.3 V (A/cm^2)	J at 0.7V (A/cm^2)	J at 0.7V (A/cm^2)
1025 °C (3Q05)	2.05 ± 0.10	1.52 ± 0.29	2.09 ± 0.28	2.54 ± 0.42
925 °C	1.84 ± 0.13	1.20 ± 0.12	2.12 ± 0.24	2.42 ± 0.21
975 °C	1.67 ± 0.24	1.19 ± 0.30	1.72 ± 0.40	1.93 ± 0.41
1025 °C	1.37 ± 0.05	1.11 ± 0.02	1.54 ± 0.01	1.69 ± 0.02

Ohmic ASR is given in Table 3-14 for the 4 specimens. In the present set of specimens, the ohmic ASR increased with increasing sintering temperature. The ohmic ASR was higher for the present specimens than for the specimens fabricated in 3Q05. One possible cause of the shift in performance between 3Q05 and the current study is the increase in the ohmic resistance.

Table 3-14 Ohmic ASR at 800 °C

800 °C	(Ω-cm^2)
1025 °C (3Q05)	0.070 ± 0.020
925 °C	0.064 ± 0.006
975 °C	0.095 ± 0.014
1025 °C	0.113 ± 0.001
1075 °C	0.110

One of the possible causes to the performance shift between the 3Q05 specimens and the current set is the process variations. Since no significant improvement was observed at other temperatures, 1025°C was used as the typical processing temperature for LSCF-1 electrode.

3.3.4 Durability/Stability

The stability of the LSCF-1 oxygen electrode was examined in contact with varied metallic current collectors, including Au screen, commercial ferritic stainless steel (donated as FSS-1), and GE13L alloy through several contact agents, CB07, SPCex19, and CBLSC55. A graphical summary of degradation rate versus starting area specific resistance for fuel cell mode tests is given in Figure 3-23. The Au mesh interconnects showed about 7 mohm-cm^2/100 hours degradation rate. The FSS-1 interconnect samples had a lower degradation rate (about 30 mohm-cm^2/100 hours) than the GE13L

samples. The GE13L had a lower degradation rate with SPCex19 than with CBLSC55 contact agent. The FSS-1 samples with CB07 showed both higher starting performance and lower degradation rate than the GE13L samples. FSS-1 current collector with CB07 was down-selected for further optimization.

Scanning electron microcope (SEM) images have been taken on cells with LSCF-1 oxygen electrode. Qualitative energy-dispersive-X-ray analysis was performed at selected locations. The cell with Au mesh contacts, which showed good stability, did not give indications of large microstructural changes. No Sr was detected within the barrier layer or at the YSZ/barrier layer interface. The cell with the GE13L contact showed evidence of a thick reaction layer (between 10-40 μm) next to GE13L. Iron and chromium were detected in the layer, probably containing $SrCrO_x$ and iron oxides. Possible mechanisms for the increased degradation with the GE13L include the growth of the resistive layer and the chromium poisoning of the oxygen electrode.

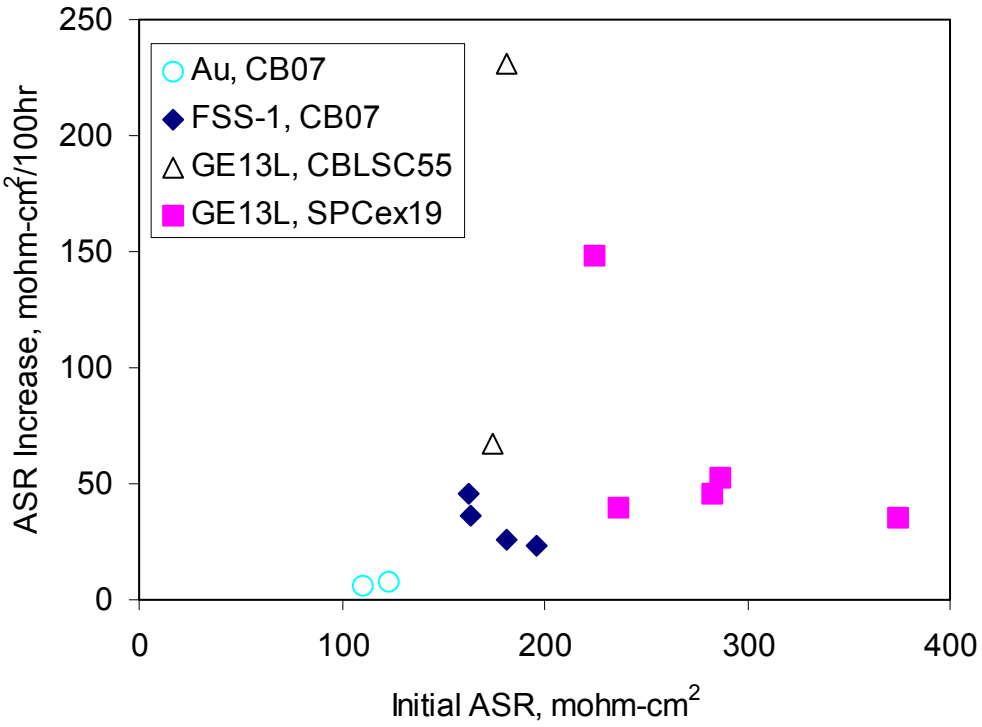

Figure 3-23. Degradation rate versus starting ASR for cells run in fuel cell mode at 0.7V (except for Au mesh samples run at 0.75V). Test durations are between 167-375 hours, and degradation rate is normalized per 100 hours

After the screening on the performance stability with varied current collectors and contact materials, the durability work was focused on evaluating effects of operating conditions and reducing the degradation rates with a protective coating on the interconnect surface at the oxygen electrode side. The oxygen electrode was LSCF-1.

FFS-1 and CB07 were used as the oxygen electrode current collectors and contact materials, respectively. Two configurations were evaluated: uncoated FSS-1 and FSS-1 with a protective coating. Performance was evaluated with 1-inch button cells. For performance testing, electrical attachment was made on the hydrogen side by bonding a perforated disk of 0.020-inch thick GE13L stainless steel. H_2 flow rate was 500 sccm and humidification of 50% was used. Air at 1 slpm was delivered to the oxygen electrode side.

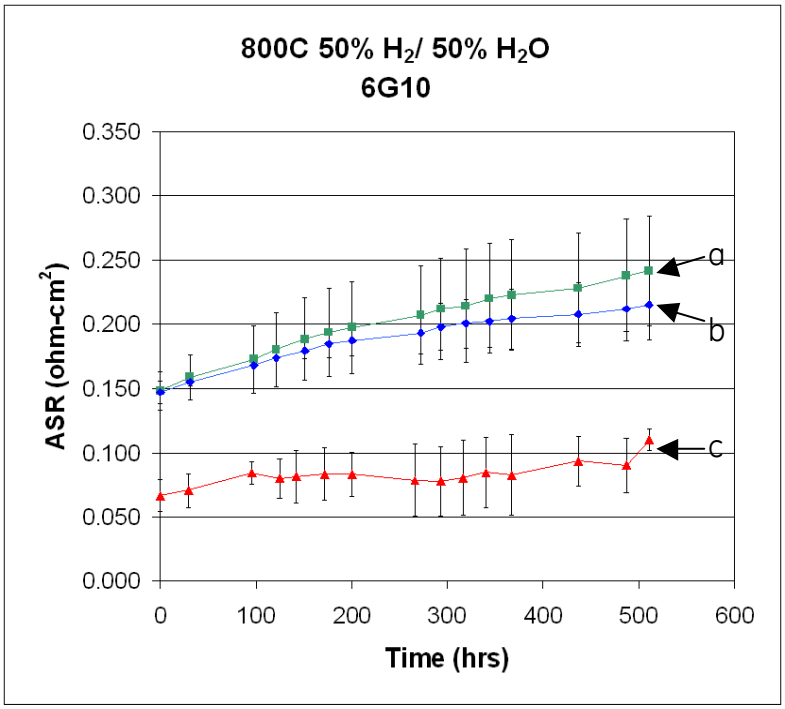

Figure 3-24 ASR as a function of time for cells under fuel cell mode with uncoated ferritic steel interconnects at 800°C with 50% H_2/ 50% H_2O: a) Total cell ASR determined at 1.5 A/cm^2 for cells held at 1.5 A/cm^2, b) Total cell ASR determined at 1.5 A/cm^2 for cells held at OCV, and c) Ohmic ASR determined from impedance for cells held at OCV

Four degradation experiments were performed. In the first experiment, cells with uncoated oxygen electrode interconnects were tested under fuel cell mode at 800°C for 511 hours. Three cells were held at 1.5 A/cm^2 and the voltage was monitored continuously. Two cells were held at open circuit voltage (OCV) and an IV curve and an AC impedance measurement was taken about once per day. The total cell ASR was calculated from the voltage at 1.5 A/cm^2 relative to the average Nernst potential, and the results are plotted in Figure 3-24. Also shown in Figure 3-24 is the ohmic ASR determined from the high frequency intercept of the AC impedance spectrum for the cells held at OCV. Comparing the total ASR obtained for those cells under the constant load and those cells held under OCV for most of the testing duration, there was no

statistically significant effect of electrochemical operation on degradation rate. This may suggest that the degradation rate be dominated by thermal/chemical mechanisms and less influenced by the electrochemical reactions when the cells were under load. The total ASR increase rate at 1.5 A/cm^2 was estimated about 160 mohm-cm^2/1000 hours and the ohmic ASR degradation was about 100 mohm-cm^2/1000 hours as summarized in Table 3-15.

In the second experiment six cells with uncoated ferritic steel interconnects were tested under fuel cell mode at 750 °C for 501 hours. Three cells were held at 1.25 A/cm^2, and the voltage was monitored continuously. Three cells were held at OCV, and an IV curve and an AC impedance measurement were taken about once per day. Total cell ASR was calculated from the voltage at 1.25 A/cm^2 relative to the average Nernst potential, and the results are plotted in Figure 3-25. Also shown is the ohmic ASR determined from the high frequency intercept of the AC impedance curve for the cells held at OCV. Similar to those observations at 800°C, there was no statistically significant effect of electrochemical operation on degradation rate. The ASR degradation rate at 1.25 A/cm^2 was about 60 mohm-cm^2/1000 hours and the ohmic ASR degradation was about 40 mohm-cm^2/1000 hours as summarized in Table 3-15. The total and ohmic degradation rates were significantly reduced at 750 °C compared with those at 800 °C for uncoated interconnects.

Table 3-15 Summary of ASR increase rates for cells tested in fuel cell mode. The change in total ASR at constant current density was calculated at 1.5 A/cm^2 for the 800°C tests and at 1.25 A/cm^2 for the 750 °C tests.

Interconnect	Temperature (°C)	Test condition	Change in total ASR at constant current density (mΩcm^2/ 1000 hrs)	Change in total ASR at 0.7V (mΩcm^2/ 1000 hrs)	Change in ohmic ASR (mΩcm^2/ 1000 hrs)
Uncoated FSS-1	800	OCV	140 ± 40	110 ± 30	80 ± 10
		1.5 A/cm^2	180 ± 60	110 ± 10	120 ± 10
Uncoated FSS-1	750	OCV	60 ± 40	70 ± 70	30 ± 10
		1.25 A/cm^2	60 ± 40	60 ± 20	50 ± 30
Coated FSS-1	800	OCV	50 ± 20	60 ± 20	90 ± 40
		1.5 A/cm^2	40 ± 20	---	---
		0.7V	70± 10	60 ± 10	90 ± 10

In the third experiment, six cells with coated ferritic interconnects were tested under fuel cell mode at 800°C for 479 hours. Three cells were held at 1.5 A/cm^2, and the voltage was monitored continuously. Three cells were held at OCV, and an IV curve and an AC impedance measurement were taken about once per day. ASR was calculated from the voltage at 1.5 A/cm^2 relative to the average Nernst potential, and the results are plotted in Figure 3-26. Also shown is the ohmic ASR determined from the high frequency intercept of the AC impedance curve for the cells held at OCV. Again, there was no statistically significant effect of continuously electrochemical operation on

degradation. The ASR degradation rate at 1.5 A/cm^2 was about 50 mohm-cm^2/1000 hours as summarized in Table 3-15. The total degradation rate was significantly reduced compared with the uncoated interconnect at 800°C, but the ohmic degradation rate was comparable. It is also worth to mention that the ohmic ASR increase appeared to be even larger than the "total" ASR increase calculated from the voltage at 1.5 A/cm^2 relative to the average Nernst potential. This may suggest electrode performance have improved over the testing period (or electrode "conditioning") when the protective coating was used.

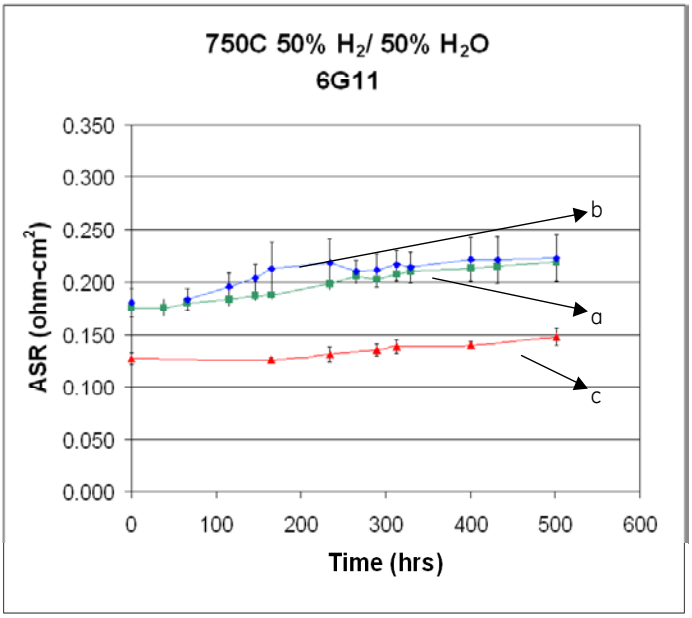

Figure 3-25 ASR as a function of time for cells under fuel cell mode with uncoated interconnects at 750 °C with 50% H_2/ 50% H_2O: a) Total ASR determined at 1.25 A/cm^2 for cells held at 1.25 A/cm^2, b) Total ASR determined at 1.25 A/cm^2 for cells held at OCV, and c) Ohmic ASR determined from impedance for cells held at OCV

In the fourth experiment, six cells with coated ferritic interconnects were tested at 800°C for 493 hours. Three cells were held in electrolysis mode at 1.3V, and current was monitored continuously. Three cells were held in fuel cell mode at 0.7V, and the current was monitored continuously. ASR was calculated from the current at 0.7V relative to the average Nernst potential for fuel cell mode and from the current at 1.3V for electrolysis mode. ASR as a function of time is plotted in Figure 3-27. Also shown is the ohmic ASR determined from the high frequency intercept of the AC impedance curve for the cells measured at the beginning and the end of the test. The total cell ASR degradation rate at 0.7V in fuel cell mode was about 60 mohm-cm^2/1000 hours (see Table 3-15) and the ASR degradation rate at 1.3V in electrolysis mode was about 80 mohm-cm^2/1000 hours as summarized in Table 3-16. The total and ohmic degradation rates were similar for fuel cell mode and electrolysis mode.

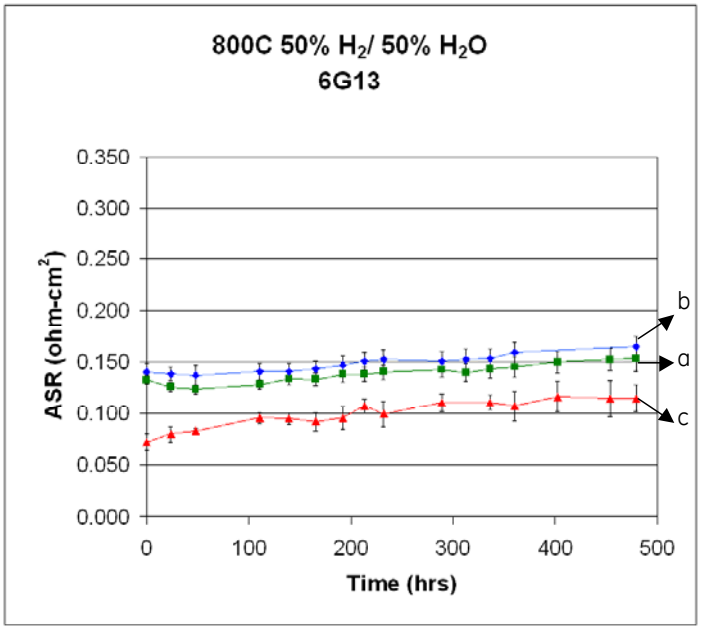

Figure 3-26 ASR as a function of time for cells with coated ferritic interconnects at 800 °C with 50% H_2/ 50% H_2O under fuel cell mode: a) Total ASR determined at 1.5 A/cm^2 for cells held at 1.5 A/cm^2, b) Total ASR determined at 1.5 A/cm^2 for cells held at OCV, and c) Ohmic ASR determined from impedance for cells held at OCV

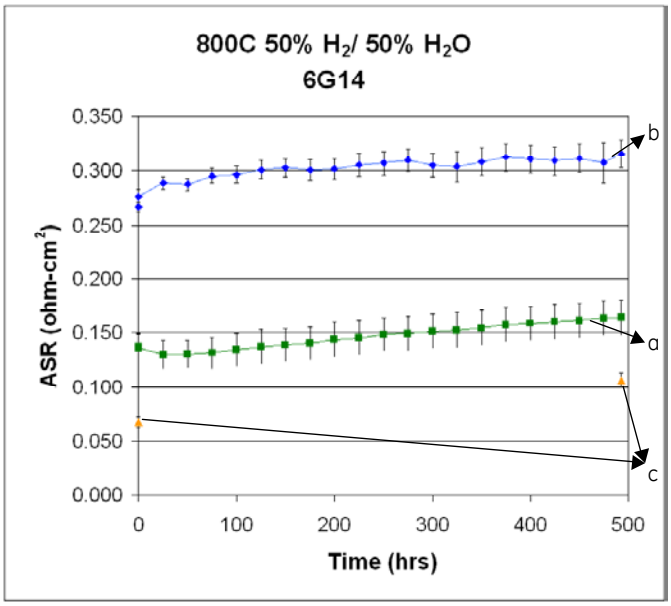

Figure 3-27 ASR as a function of time for cells with coated interconnects at 800°C with 50% H_2/ 50% H_2O: a) Total ASR determined at 0.7V for cells held at 0.7V under fuel cell mode, b) Total ASR determined at 1.3V for cells held at 1.3V under electrolysis mode, and c) Ohmic ASR determined from impedance for all cells at the beginning and end of the test

Table 3-16 Summary of ASR degradation rates for cells tested in electrolysis mode.

Interconnect	Temperature (°C)	Test condition	Change in total ASR at 1.3V ($m\Omega cm^2$/ 1000 hrs)	Change in ohmic ASR ($m\Omega cm^2$/ 1000 hrs)
Coated FSS-1	800	1.3V	80 ± 20	70 ± 10

In summary, the following conclusions can be made from the comparison of the ASR degradation rates with the material sets (LSCF-1, CB07, and FSS-1)

- No difference was observed in the degradation rate between cells held in fuel cell mode compared with cells that were held at OCV. Continuously electrochemical operation on the cell didn't significantly accelerate the performance degradation. The dominant degradation mechanisms were likely to be thermally activated.

- For the uncoated interconnects, the initial ASR at 750°C was 20% higher than the ASR at 800°C but the degradation rate was about two times slower, providing a favorable trade-off between performance and degradation. Reducing the operating temperature of the cell is an effective means to reduce degradation rates.

- The cells with the coated interconnects showed a factor of two reduction in degradation rate while maintaining the initial ASR.

- The ASR degradation rates under electrolysis mode at constant voltage of 1.3V are comparable to those under fuel cell mode at constant voltage of 0.7V.

4 CELL FABRICATION AND EVALUATION

4.1 CELL FABRICATION

Tape-calendering process was used to make electrode-supported reversible solid oxide fuel cells. In the basic calendering process, the starting materials for the tapes, either electrolyte or support electrode with additives, organic binders, and plasticizers are combined in a high shear mixer to create a homogeneous plastic mass. Each plastic mass is then rolled to produce a thin and flexible sheet to desired thickness. The electrolyte and support electrode tapes of certain thickness ratio are then laminated together to form a bilayer and subsequently rolled to reduce the thickness of each layer. Another support tape is added to the bilayer and again rolled down. The addition of support electrode tapes has the effect of reducing the electrolyte thickness while keeping the bilayer at a proper thickness. Such process is repeated until the desired thickness of electrolyte is reached. At this point the bilayer is cut to the desired shape and size. The green tapes are then fired in air to sinter the bilayer tape. The second electrode is then screen printed on the electrolyte surface of the bilayer to produce a single cell.

4.2 PERFORMANCE EVALUATION

The testing vehicle was a single cell module with cell of 16-cm in diameter and ferritic stainless steel (FSS-1) interconnect with gas manifolds and embedded flow fields. The nominal operating temperature was 800°C. For reversible operations, a mixture of 50%H_2O/50%H_2 was used to feed the hydrogen electrode under both fuel cell and electrolysis mode.

In addition to dilute hydrogen (64%H_2/36%N_2), methane was also used in the fuel cell operation to investigate the internal reforming characteristics. Gas chromatography was used to characterize the internal reforming composition. For hydrogen production mode, steam with hydrogen addition (to prevent Ni oxidation at the start of the electrolysis) was used as the reactant feed. Cell polarization, hydrogen production ability, performance stability over prolonged period has been measured.

4.3 BASELINE PERFORMANCE

In single cell module performance evaluation, the baseline cell configuration consists of a thin YSZ electrolyte sandwiched between a Ni/YSZ fuel electrode and a LSM/YSZ oxygen electrode. The performance is shown in Figure 4-5. It is seen that the polarization curves of fuel cell and electrolysis with 50%H_2O/50%H_2 stream is quite symmetric, implying that there is no drastic change in reaction kinetics between fuel cell and electrolysis under the testing conditions. For internal reforming capability, mixture of CH_4 and H_2O with steam-to-carbon ratio of 1.5 was used. The CH_4-H_2O mixture was further diluted with N_2 so that the fuel content under thermodynamic equilibrium would be close to that of 64%H_2/36%N_2 for performance comparison. With internal reforming fuel stream, CH_4 conversion through fuel electrode flow field was measured to be approximately 85% under open circuit. When a current was drawn, the internal reforming rate was promoted by the increase in steam content and CH_4 conversion reached as high as 99% at 60% fuel utilization.

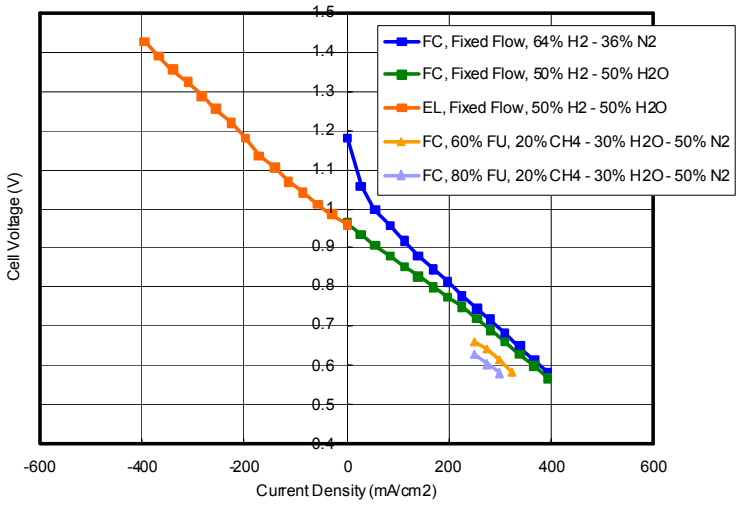

Figure 4-1 Baseline (U001) performance at 800°C

Electrolysis performance stability of baseline cells with LSM/YSZ oxygen electrode was also evaluated. As shown in Figure 4-2, the performance decayed rapidly with ASR increase of more than 10,000 mohm-cm^2/1000 hrs.

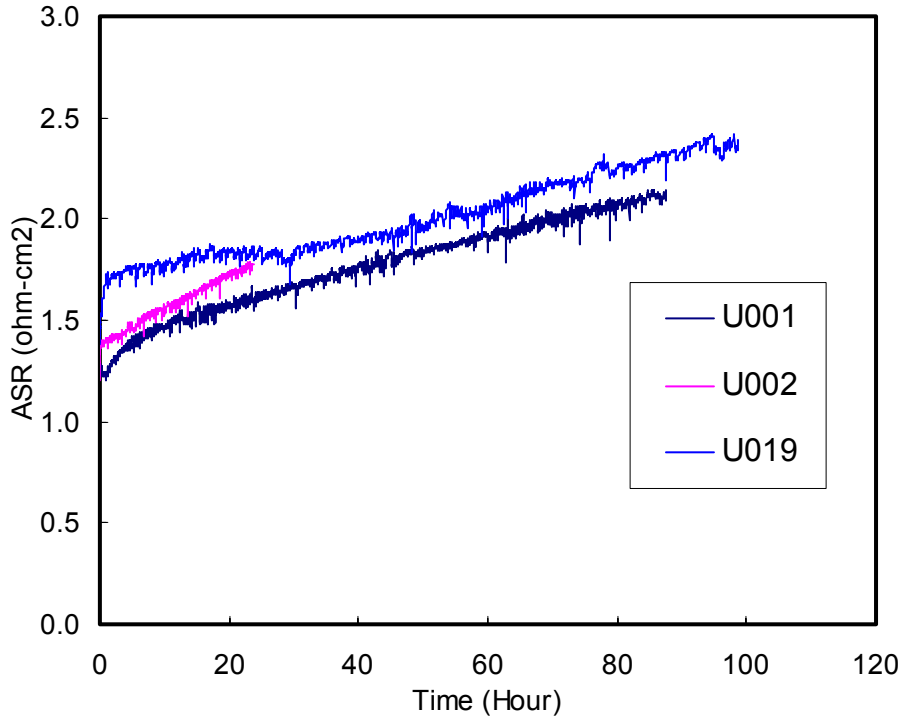

Figure 4-2 Performance stability at 800°C for three baseline cells (U001, U002, and U019) under electrolysis mode with LSM-based oxygen electrode

To diagnose the performance characteristics, a configuration with a reference electrode was used. The voltage leads of fuel electrode and oxygen electrode were wired against reference electrode to allow for individual electrode performance monitoring. Due to the electrode-supported thin electrolyte cell configuration, a measurement error is inevitable [12-14]. However, the cell configuration with a reference electrode can be used to "estimate" the electrode performance losses, especially for electrode performance stability.

Figure 4-3 shows the measured voltages over time from cell module U019. The cell was operated under fuel cell and electrolysis mode. While the fuel cell performance was relatively stable, the performance decayed rapidly under electrolysis mode. It appears that most of the degradation under the electrolysis operation came from the oxygen electrode. It has been known that LSM can interact with YSZ to form resistive materials such as $La_2Zr_2O_7$ and $SrZrO_3$. Under SOFC operations, the oxygen activity at the triple phase boundaries (tpb) decreases, which may lead to less driving force for the oxidative formation of $La_2Zr_2O_7$ and $SrZrO_3$. Under steam electrolysis, the oxygen

activity at the anode tpb will be increased, as the oxygen will be generated at the interface [15]. That may increase the formation of the resistive materials, leading to accelerated degradation and delamination induced by the local pressure built-up. This is consistent with the observation on delamination between the LSM/YSZ electrode and the YSZ electrolyte after electrolysis operation (Figure 4-4).

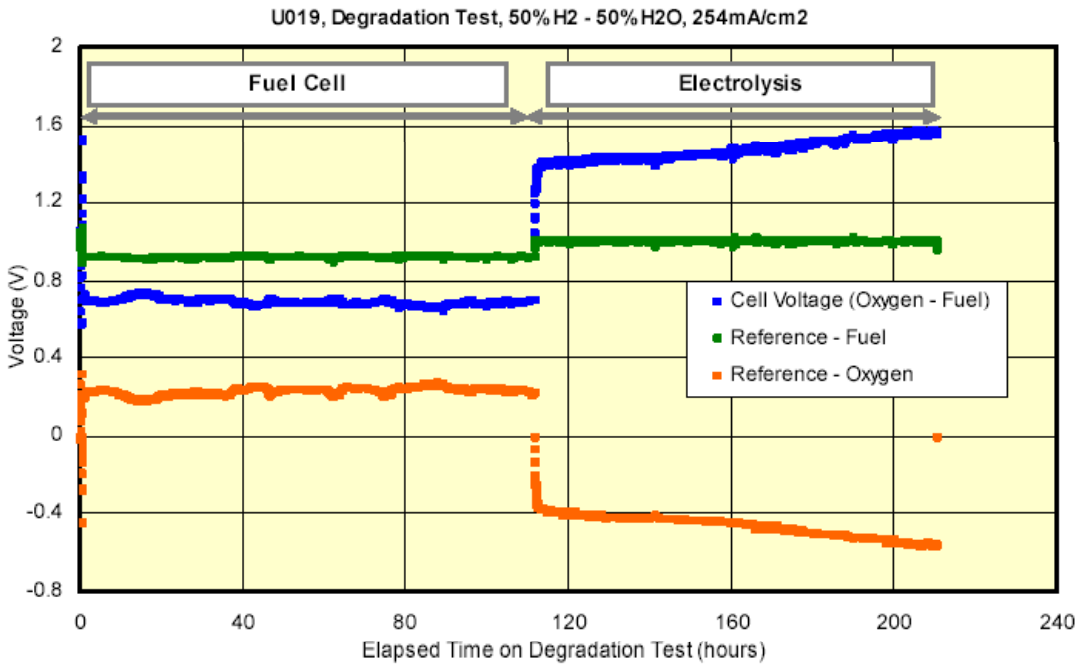

Figure 4-3. Voltage changes with time in cell module U019 under fuel cell and electrolysis operation at 800°C, indicating that the major decay was resulted from the oxygen electrode in electrolysis mode

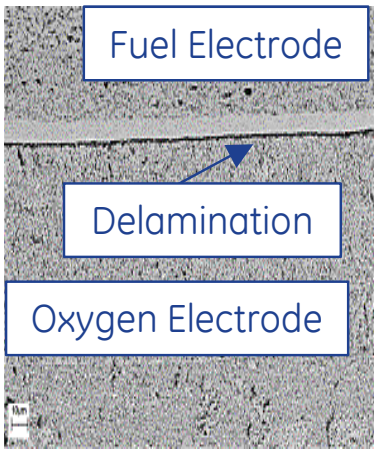

Figure 4-4 Cross section of a tested cell showing delamination between LSM/YSZ oxygen electrode and YSZ electrolyte

4.4 PERFORMANCE IMPROVEMENT

4.4.1 LSCF Electrode and SDC Barrier Layer

As LSCF performed better than the LSM/YSZ oxygen electrode in button cells screening, Gen-I cell were made with the LSCF-1 oxygen electrode and an improved hydrogen electrode with porosity engineering. The performance and performance stability of Gen-I cells were compared with baseline cell configurations. Figure 4-5 shows the polarization curves of the baseline cells and Gen-I cells measured with 50%H_2/50%H_2O fuel stream. As shown, significant improvement in RSOFC performance has been realized with the Gen-I cell design. The ASRs measured on individual cell tests are summarized in Table 4-1. More than 60% reduction in ASR was achieved by using Gen-I cell design.

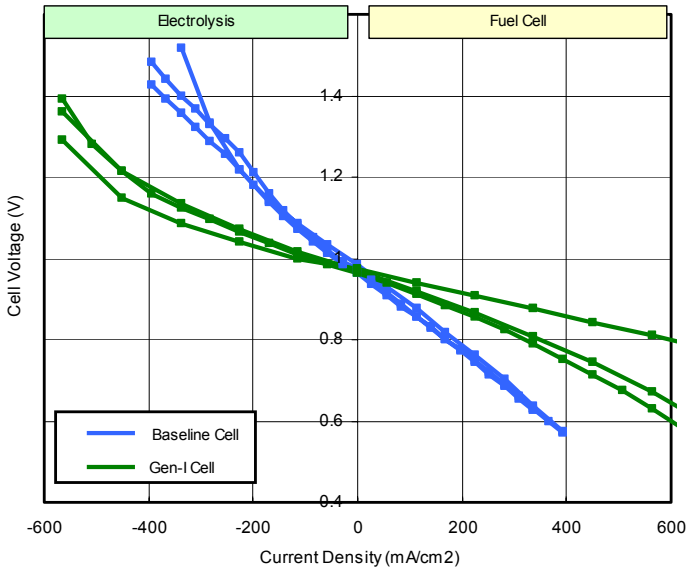

Figure 4-5 Polarization curves measured on 3 baseline cells and 3 Gen-I cells

Table 4-1 ASRs of baseline cells and Gen-I cells

Baseline Cell Test	Fuel Cell ASR at 0.282 A/cm2 (ohm-cm2)	Electrolysis ASR at -0.282 A/cm2 (ohm-cm2)
U001	0.853	1.183
U002	0.871	1.332
U019	0.814	1.346
Mean	0.846	1.287
St. Dev	0.03	0.09

Gen-I Cell Test	Fuel Cell ASR at 0.282 A/cm2 (ohm-cm2)	Electrolysis ASR at -0.282 A/cm2 (ohm-cm2)
U016	0.140	0.385
U017	0.332	0.527
U029	0.378	0.498
Mean	0.283	0.470
St. Dev	0.13	0.08

Along with the improvement in module performance as mentioned above, Gen-I cell tests also showed substantial improvement in performance durability over the

baseline cells. The degradation behaviors observed in three baseline cell tests and three Gen-I cell tests were compiled and compared in Figure 4-6 and Table 4-2.

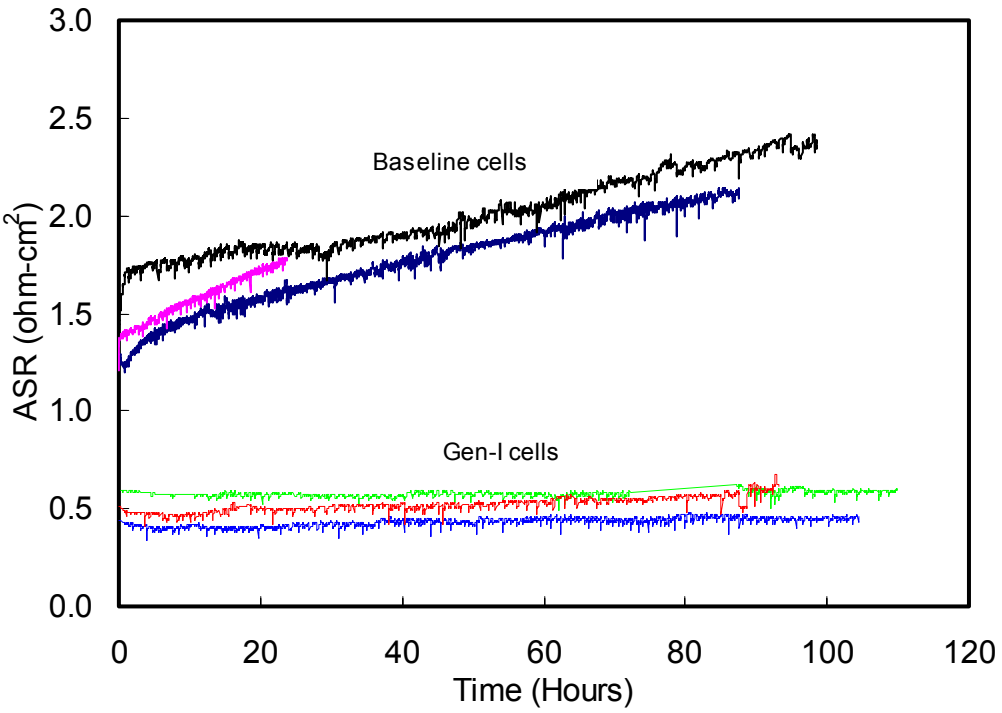

Figure 4-6 ASR changes over time at 0.254A/cm^2 in electrolysis with the baseline and the Gen-I Cells

Table 4-2 ASR increase over 100 hours measured at 0.254 A/cm^2 under electrolysis

Baseline Cell Tests	Degradation Rate (ASR increase / 100 hours : ohm-cm2 / 100 hours)
U001	1.01
U002	2.41
U019	1.01
Mean	1.48
Std Dev	0.81

Gen-I Cell Tests	Degradation Rate (ASR increase / 100 hours : ohm-cm2 / 100 hours)
U016	0.01
U017	0.00
U029	0.11
Mean	0.04
Std Dev	0.06

For SDC barrier layer process engineering, two firing temperature with 100°C difference have been tried and the cell performance was evaluated. As shown in Figure 4-7, no statistical significance was observed for the cells with baseline processing temperature and those with a higher processing temperature by 100°C.

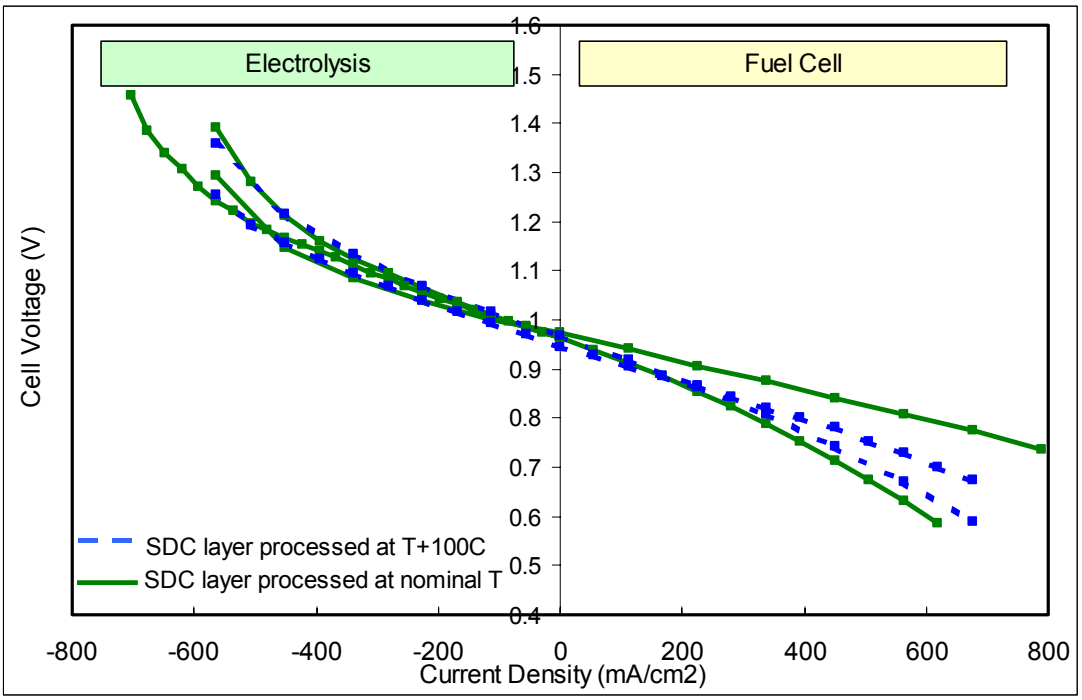

Figure 4-7 Initial performance of cell modules with SDC layer processed at different temperatures

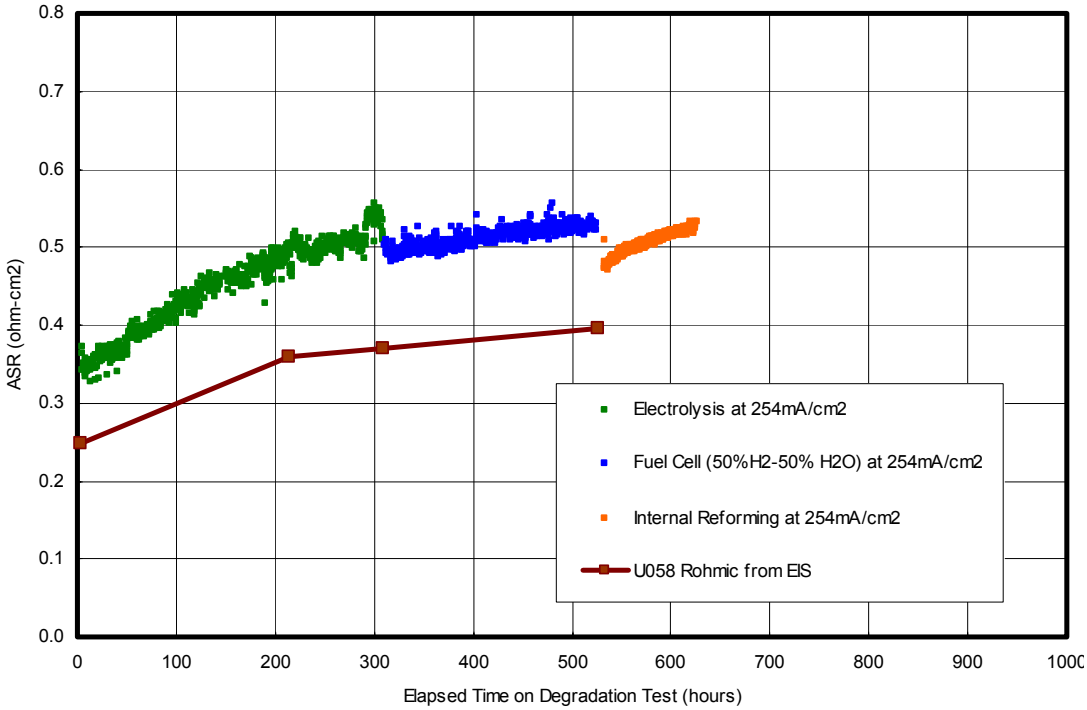

Figure 4-8 Performance stability of module (U058) with SDC layer processed at a higher temperature

Performance stability of the cells with SDC layer processed at a higher temperature was also evaluated and the estimated cell ASR is shown in Figure 4-8. The total cell ASR increase was estimated as ~0.2 ohm-cm^2/1000 hours and it was comparable to that observed in cells with SDC layer processed at baseline temperature. The ohmic ASR change measured with impedance analyzer is also shown in the same figure. Again, the ohmic resistance increase contributed significantly to the overall cell degradation. There has been a number of degradation mechanisms proposed in the literature [16-22], such as metal oxidation and Cr poisoning of the oxygen electrode. In addition to the metal oxidation and Cr poisoning to the electrode, another possibility is the reaction of Cr volatile species with LSCF electrode and contact material to form resistive phase $SrCrO_x$. A layer of $SrCrO_x$ has been observed in some of the tested cells.

4.4.2 Hydrogen Electrode

Two approaches were used to improve the hydrogen electrode. First, the hydrogen electrode microstructure was improved with porosity and layer configuration design. The improved hydrogen electrode was implemented in the Gen-I cell design, leading to significant performance improvement in conjunction with a LSCF-1 electrode. Second, Ni/YSZ ratio was tailored in an effort to further improve the electrode performance. Within the experimental range, however, no performance improvement has been realized. Nevertheless, the cell with modified hydrogen electrode was further tested for performance durability. The performance durability was shown in voltage change over time (Figure 4-9) and corresponding cell ASR change with time (Figure 4-10). In the nearly 1000-hour test, the cell was under electrolysis mode for most of the time. The voltage increase was estimated as 50mV/1000 hrs under an electrolysis current density of 0.254A/cm^2. This suggests a performance decay rate less than 5%/1000 hrs with initial cell voltage of ~1070 mV.

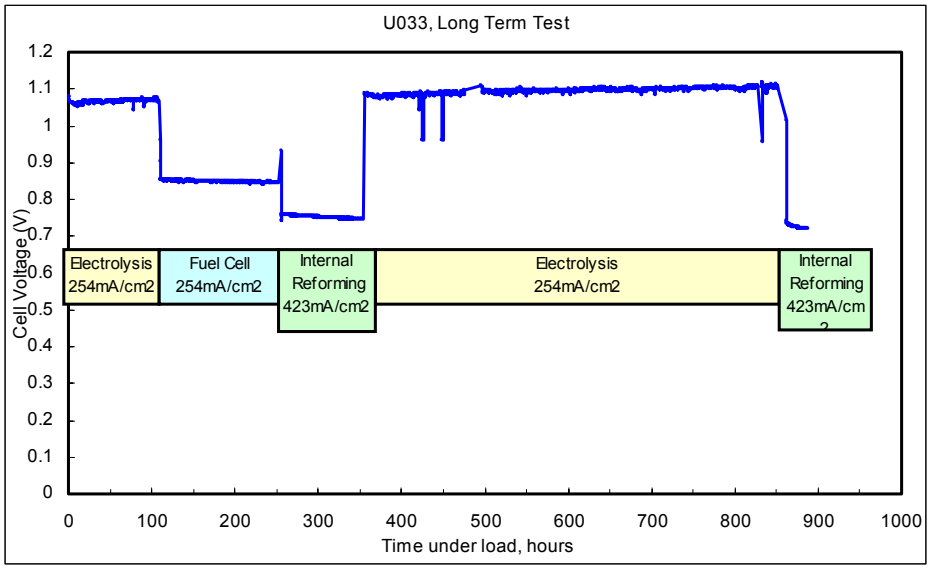

Figure 4-9 Performance stability of module U033 at 800°C

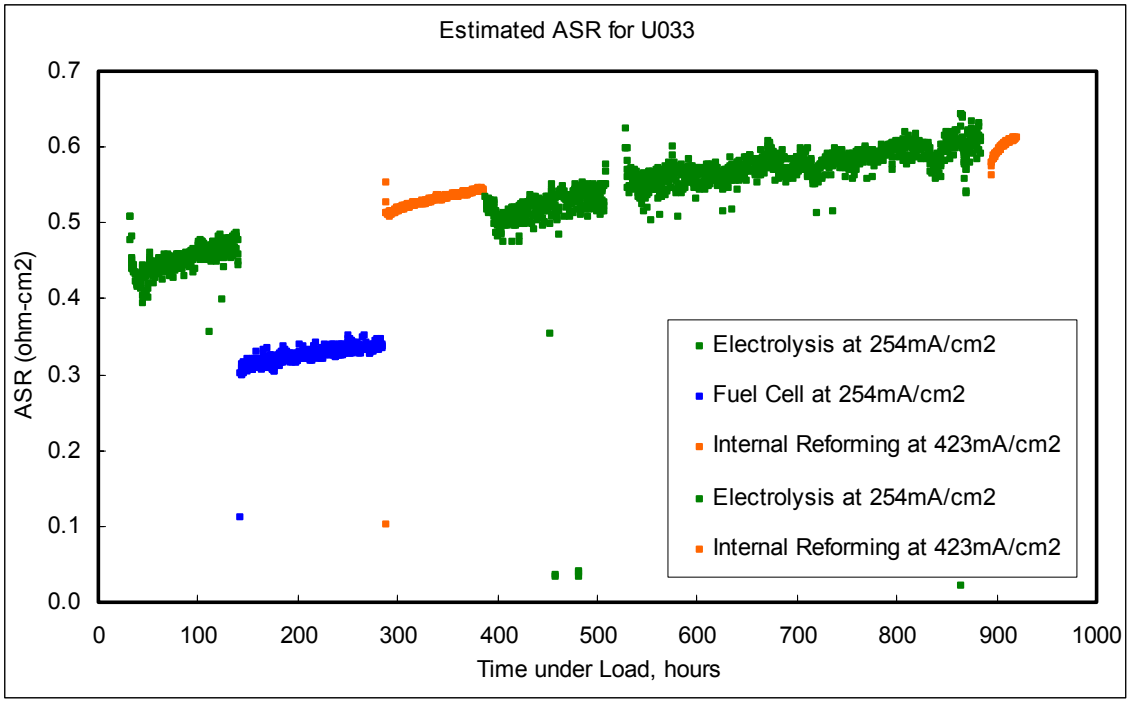

Figure 4-10 Estimated ASR change with time for module U033

As shown in Figure 4-10, the initial cell ASR was estimated around 0.43 ohm-cm^2 and it increased with time and reached ~0.6 ohm-cm^2 at the end of the test. Overall, the ASR increase was estimated to be ~0.2 ohm-cm^2/1000 hrs. The ohmic resistance of the module was also estimated with impedance analyzer and it was approximately 0.12 ohm-cm^2/1000 hrs, which accounted for roughly 60% of the cell module ASR increase. This suggests a significant ohmic contribution to the overall cell degradation observed.

4.4.3 Electrode and Interconnect Contact

Contacts between electrode and stainless steel interconnect (FSS-1) was investigated for possible performance and stability improvement.

In an effort to improve the contact between fuel electrodes and interconnect, the fuel electrode surfaces were pretreated before assembly and test. Two cell modules (U062 and U067), which had hydrogen electrode surfaces pretreated, were tested and compared with modules U029, U033 and U058 that had cells without such pretreatments. As shown in Figure 4-11, no improvement has been realized through the pretreatment on the fuel electrode surfaces.

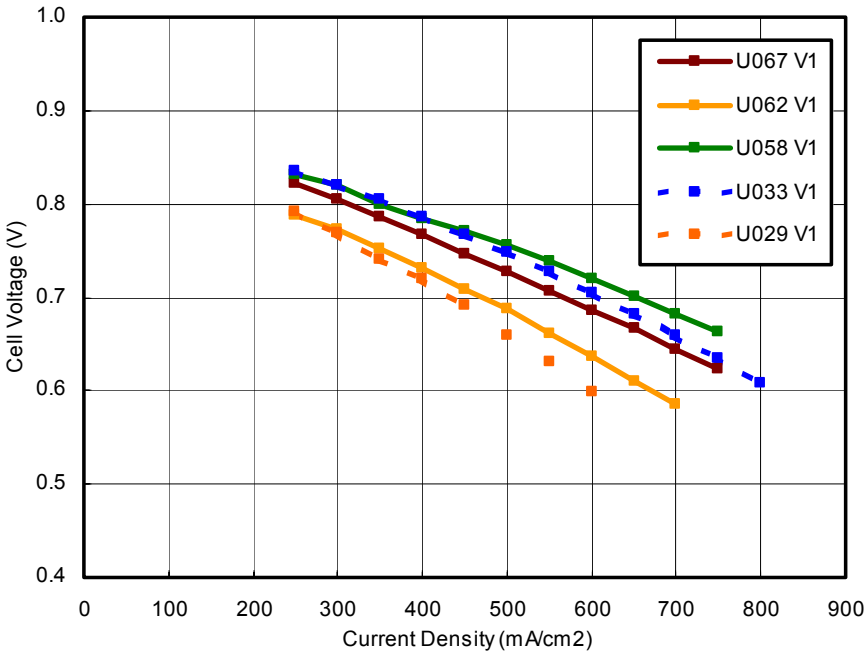

Figure 4-11 Fuel cell performance (800°C and 80% fuel utilization) of modules with (U062 and U067) and without (U0.29, U033, U058) hydrogen electrode pretreatment

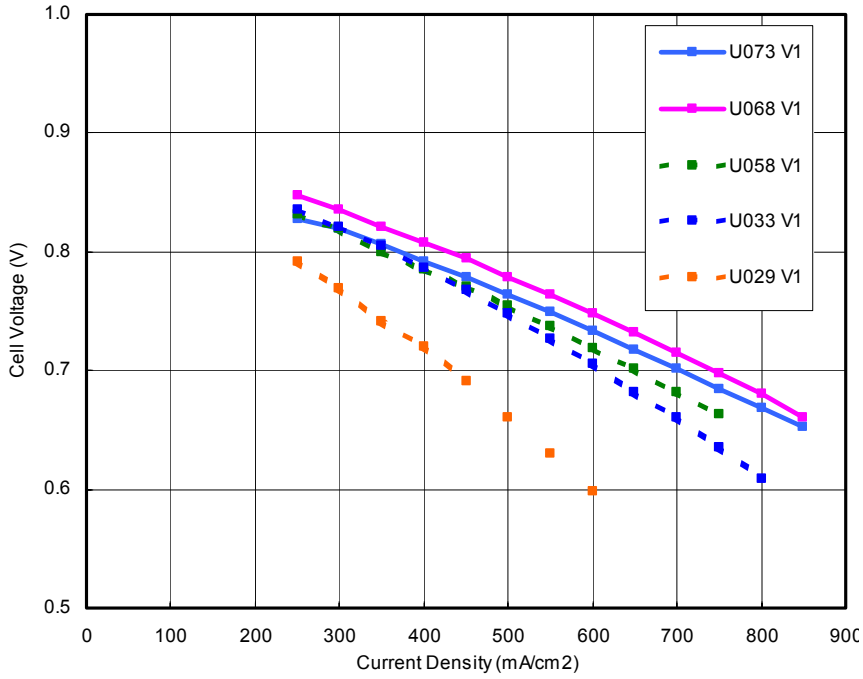

Figure 4-12 Fuel cell performance (800°C and 80% fuel utilization) of modules with (U068 and U073) and without (U029, U033, U058) pretreatment on the oxygen electrode interconnect surfaces

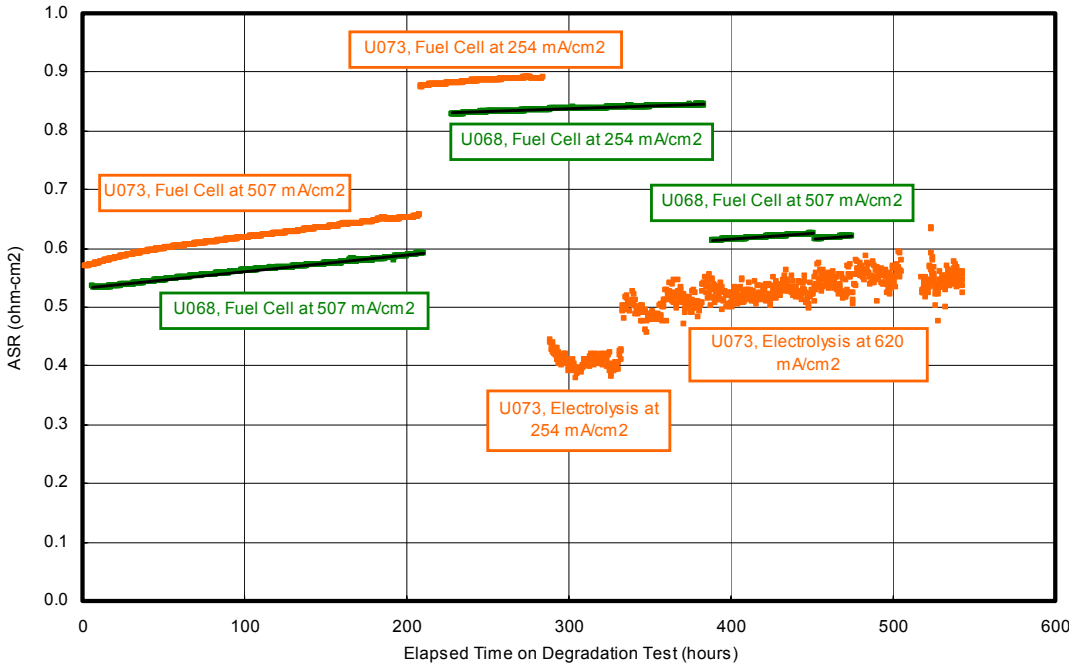

Figure 4-13 Stability of modules U068 and U073 at 800°C

To improve the contact between the oxygen electrode and adjacent interconnect, the interconnect surfaces were pretreated before cell assembly and test. As shown in Figure 4-12, modules with pretreated interconnect surfaces (U068 and U073) performed better than other modules without such treatment.

Stability of these two modules with pretreatment on the interconnect surfaces was also evaluated (Figure 4-13). The initial ASR and the ASR change over time are comparable for these two modules. The ASR increase was estimated as 200-300 mohm-cm^2/1000 hrs. This indicates the pretreatment on the interconnect surface has improved the module performance without compromise of the performance durability.

4.5 PERFORMANCE ANALYSIS AND OPERATION CHARACTERISTICS

4.5.1 Performance Analysis

Similar to the performance diagnosis on baseline cells, performance of Gen-I cells was investigated using a configuration with a reference. Figure 4-14 shows the measured voltages over time from a Gen-I cell module (U029). The cell was operated under electrolysis, fuel cell with hydrogen as fuel, and fuel cell with internal reforming. The degradation rate of Gen-I cells was seen to be lower under electrolysis operation than that under fuel cell operation. It appeared that most of the degradation under the fuel cell operation came from the oxygen electrode independent on the fuel feed (dilute hydrogen vs. CH_4/H_2O mixture). At ~330 hours, the reference vs. fuel electrode voltage

started to drop rapidly. This abnormality might be related to leakage through seal and cracks at cell edges, which were observed in the post-test analysis.

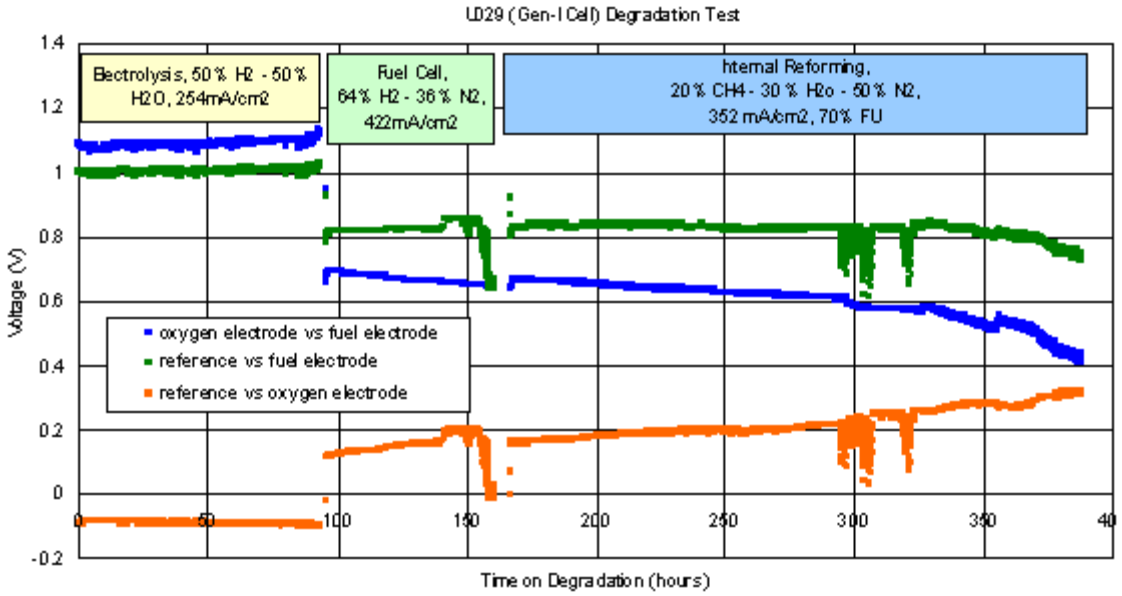

Figure 4-14 Measured voltage changes with time in Gen-1 cell U029 under electrolysis, fuel cell with dilute hydrogen fuel, and fuel cell with internal reforming at 800°C

4.5.2 Input Hydrogen Content

Impact of the hydrogen content to the cell performance was also evaluated under electrolysis mode. Generally, the feed stream needs to have proper amount of H_2 to keep Ni-based fuel electrode from being oxidized under various operation conditions. A test with varied H_2 content (balance with steam) in the feed stream was conducted at steam utilization ~22% and current density 254 mA/cm^2.

As shown Figure 4-15, in electrolysis cell voltage rose with inlet H_2 content. The equivalent OCVs at feed inlet and outlet were also calculated based on their corresponding gas compositions. The electrolysis cell voltage increase under the conditions tested was largely due to the Nernst potential increase with the H_2 content. From a system perspective, effective extraction of hydrogen from the product will significantly reduce the electrolysis cell voltage, thus the power consumption for the steam electrolyzer.

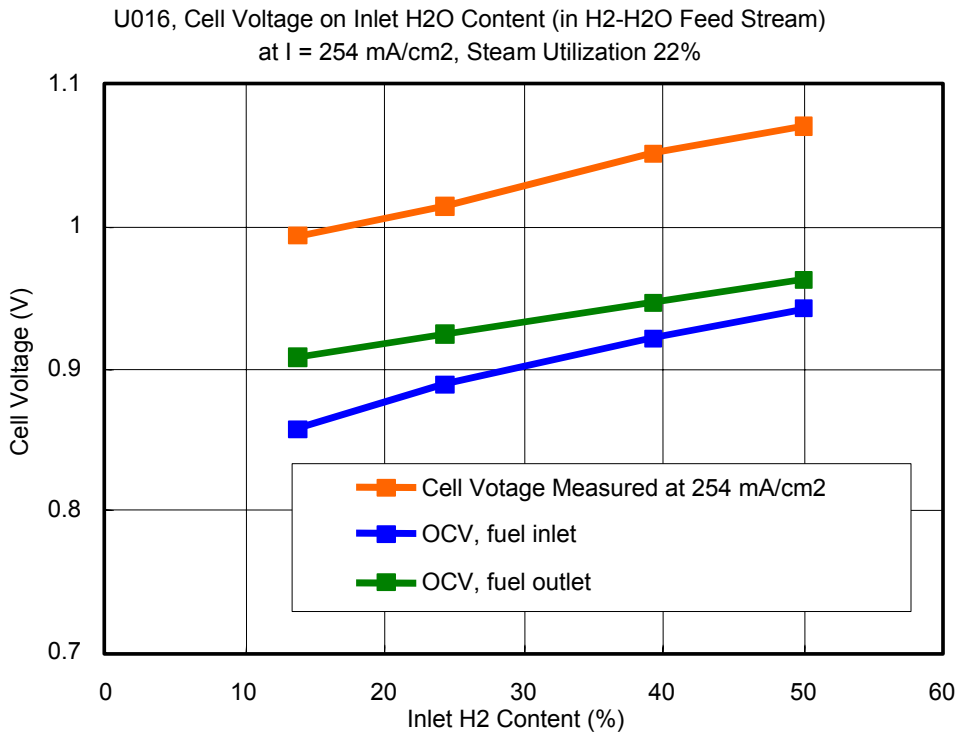

Figure 4-15. Impact of H_2 content in the inlet stream on electrolysis voltage, Nernst potentials at the inlet and outlet

5 STACK DEVELOPMENT

5.1 RSOFC STACK DESIGN AND ASSEMBLY

The RSOFC stack was based on GE proprietary stack design. The stack consisted of circular cells of active area 142 cm^2 per cell and interconnects made of a commercial ferritic stainless steel. Both fuel stream and air stream were preheated inside a furnace before entering stack to reduce the temperature gradient. Fuel exhaust stream out of individual single cells was collected in fuel outlet manifold and was directed to ventilation. A by-pass valve was installed to allow for flow rate measurement of fuel exhaust stream using a mass flow meter. Before stacking, all cells and stack repeat unit subassemblies passed through a quality control process.

5.2 STACK PERFORMANCE IMPROVEMENT

Two 3-cell stacks (U047 and U059) was assembled and tested before the final demonstration stack (U089, 10-cells) was built. Figure 5-1 shows the initial performance under fuel cell mode for the three stacks tested. Performance was improved from stack to stack with oxygen electrode process control and reduction of the contact resistance between the electrodes and interconnects.

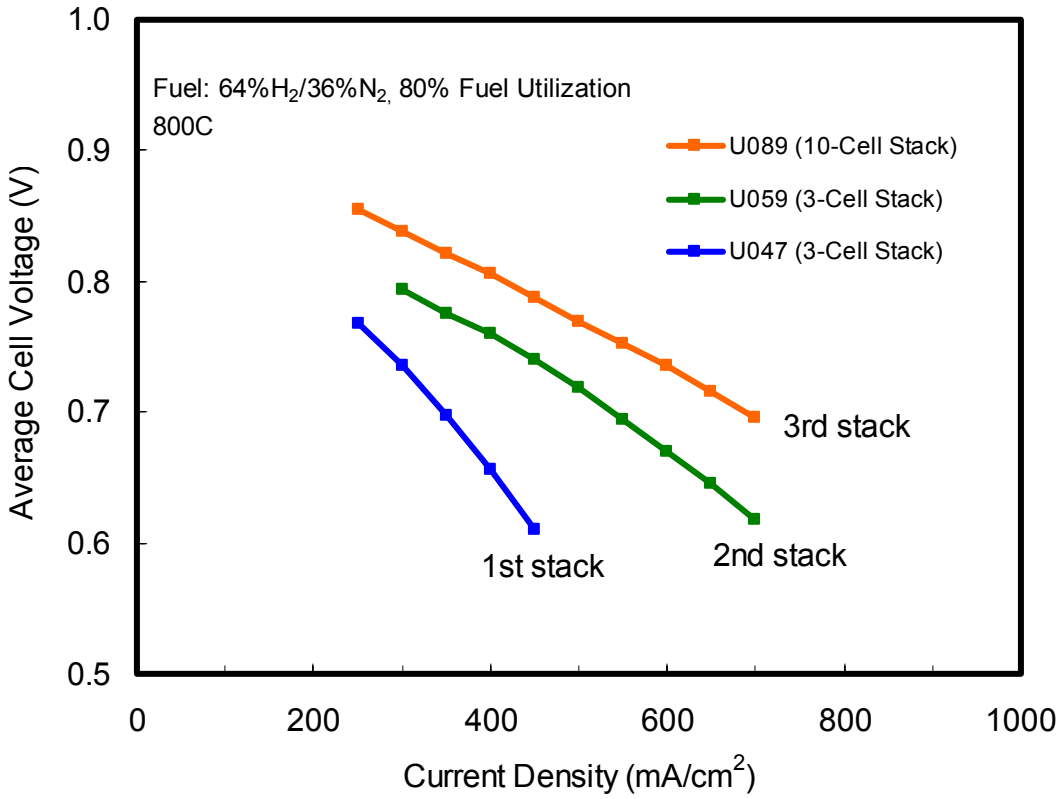

Figure 5-1 Stack performance improvement with oxygen electrode process control and contact resistance reduction

5.3 STACK PERFORMANCE STABILITY

All three stacks were operated for over 1000 hours and the performance of individual cells were monitored. Figure 5-2 shows the individual cell performance stability of one 3-cell stack (U059) under varied operating conditions. Cell 1 and cell 2 showed relatively stable performance, while cell 3 showed high ASR increase with time. The fast degradation rate for cell 3 might be associated with the contact resistance change between electrodes and interconnects. For cell 1 and 2, the overall ASR increase during the 1000 hours of operation was ~0.2 ohm-cm^2, which was comparable to the data observed in single cell modules.

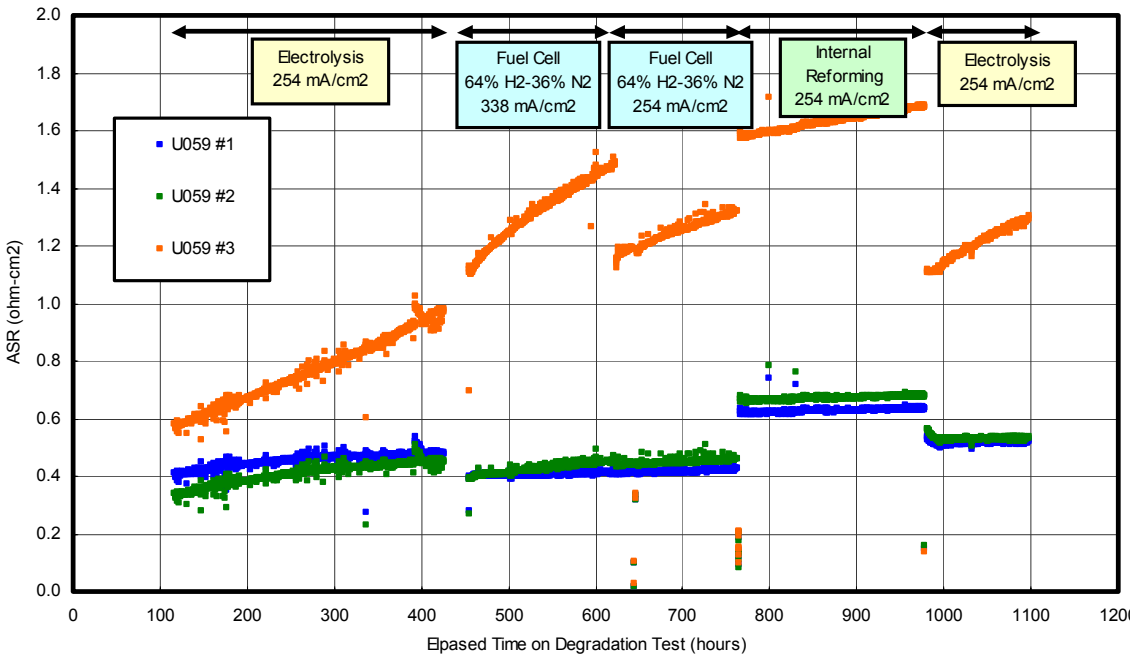

Figure 5-2 Individual cell performance stability of 3-cell stack U059 at 800°C

Post mortem analysis on stack (Stack U047) was also conducted. The effort was focused on microstructure observation and compositional analysis. The compositional analysis was obtained at multiple locations and some examples are shown below. The general observations are summarized as following:

- Microstructure was examined with Secondary Electron Microscopy (SEM). Delamination was observed between SDC barrier layer and YSZ electrolyte, LSCF electrode and SDC barrier layer (Figure 5-3). It was unclear whether the delamination occurred during stack test period or after test (stack cooling down, post test analysis). The delamination could cause performance degradation if it occurred during stack operation period.
- Compositional profiles were obtained with Electron Microprobe Analysis (EMPA). Figure 5-4 is a simplified plot showing the Cr profile through the cell cross sections. The transport of Cr from the stainless steel interconnect might have caused the cell performance degradation. The region under channel (Figure 5-4a, 2B-Off-1, gas channel area where there was no contact materials and there was no direct interconnect contact to the oxygen electrode) shows substantially higher Cr content in oxygen electrode than the region under rib (Figure 5-4b, 2B-On-1, area where interconnect rib is in contact with the oxygen electrode through a contact material).

- Noticeable difference in Sr profile through the electrode was also observed from multiple locations (Figure 5-5). The region under rib (Figure 5-5b, 2B-On-1) showed relatively uniform Sr content through the oxygen electrode layer, while “depletion” in Sr content was observed in the region under channel (Figure 5-5a, 2B-Off-1). Possible migration of Sr into the barrier layer was also observed in some regions (Figure 5-5a). The causes to Sr “depletion” and its impacts to performance stability were unclear at this stage.

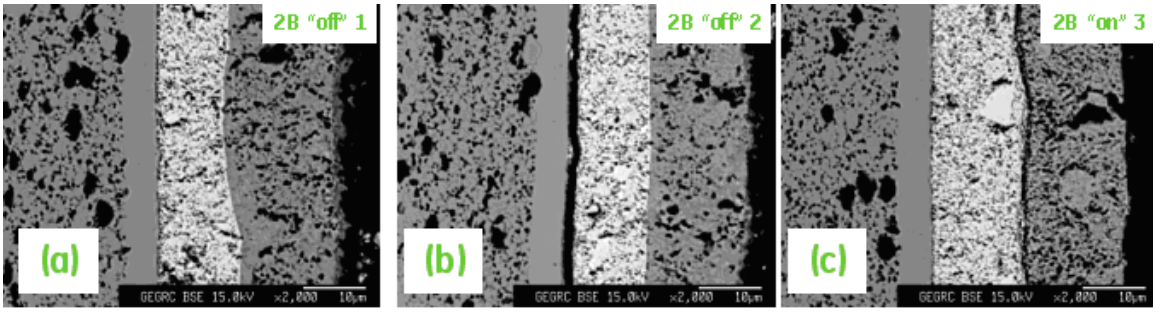

Figure 5-3 Microstructures of one cell in stack U047. (a) typical cross section, (b) cross section showing the delamination between YSZ electrolyte and barrier layer, (c) cross section showing delamination between SDC barrier layer and LSCF oxygen electrode.

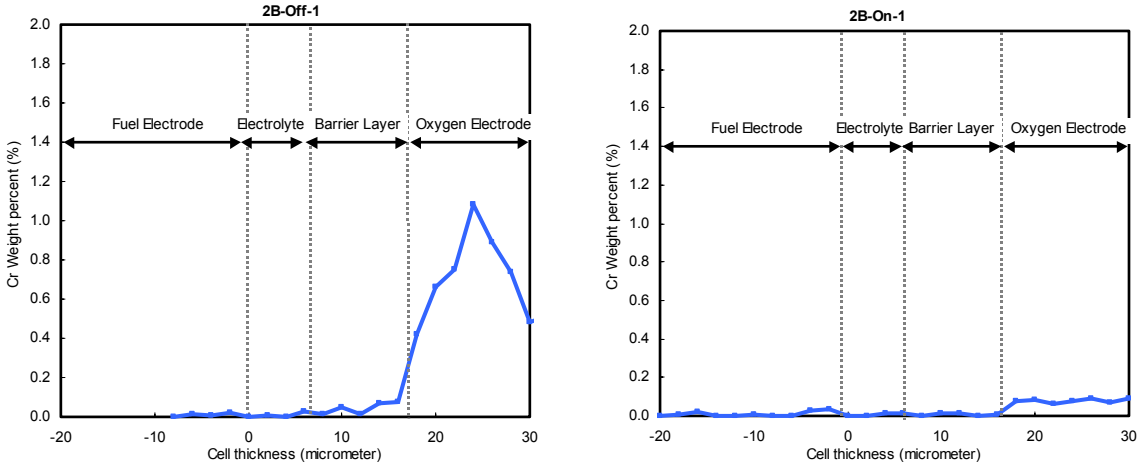

(a) (b)

Figure 5-4 Cr profile through cell cross sections in (a) region under channel, and (b) region under rib

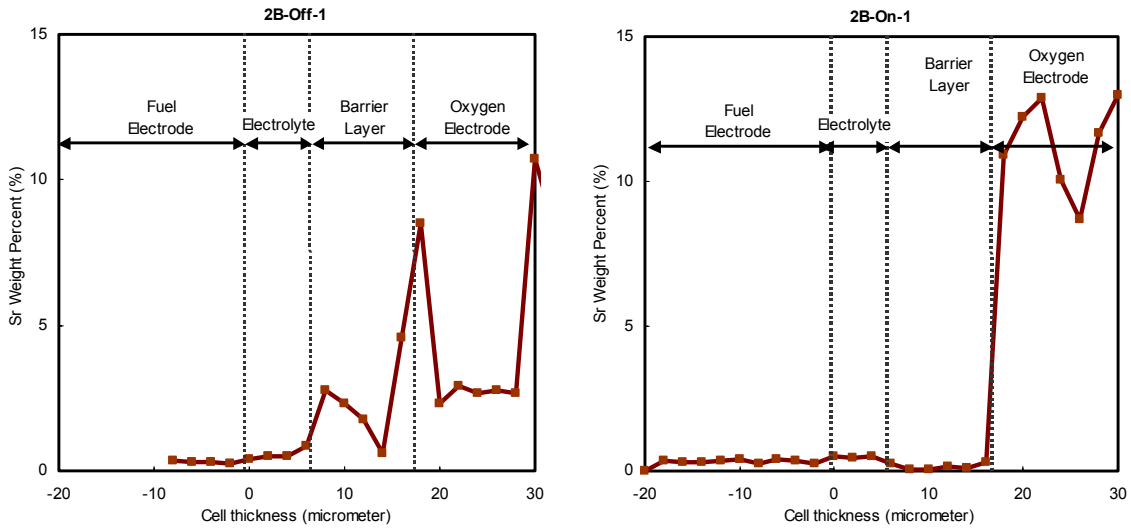

(a) (b)

Figure 5-5 Sr profile through cell cross sections in (a) region under channel, and (b) region under rib

5.4 HYDORGEN PRODUCTION

H_2 generation rate was measured from dehumidified fuel exhaust stream when the stack was operated under electrolysis mode. The input gases to the stack consisted of H_2 and steam. The H_2 flow rate measured at the stack (U047) fuel exhaust stream (dehumidified) was shown in Figure 5-6. The predicted hydrogen flow rates based on the initial hydrogen input and the applied current was also shown for comparison. H_2 flow rate measured matched with the predicted H_2 flow rate fairly well in the experimental range. The slight difference could be due to stack leak and the leakage rate was estimated as 4-6%.

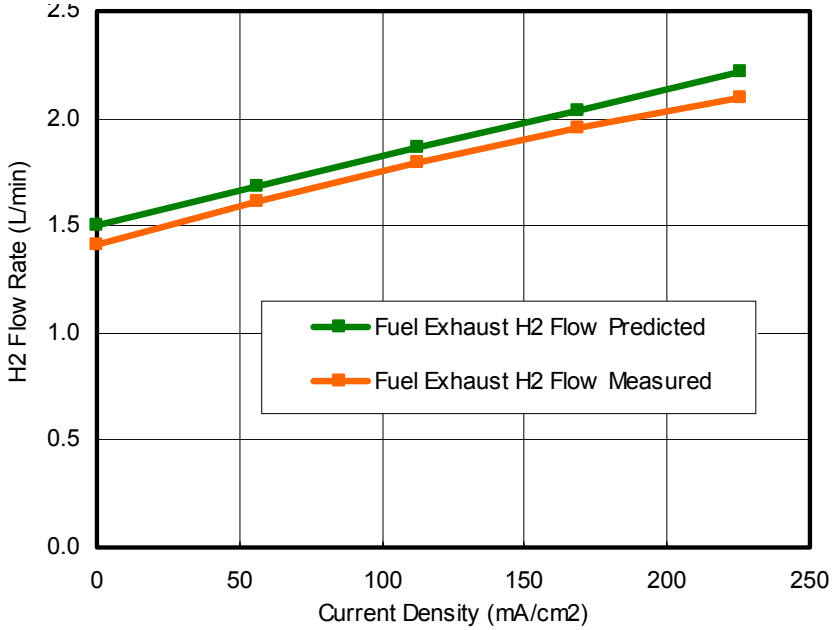

Figure 5-6 H_2 generation through steam electrolysis from Stack U047

5.5 STACK PERFORMANCE DEMONSTRATION

The demonstration stack was 10-cell stack and the main objective was to implement the advancements through the program and demonstrate the power generation in fuel cell and hydrogen production under electrolysis. Figure 5-7 shows the picture of the demonstration stack (U089) built inside a test furnace and Figure 5-8 shows the fuel cell performance at 80% fuel utilization with 64%H_2/36%N_2 as fuel. The stack ran very successfully with the highest stack performance in the program with 480 mW/cm^2 at 0.7V and 80% fuel utilization.

Figure 5-7 Image of the demonstration stack (U089, 10-cell) built in a testing furnace

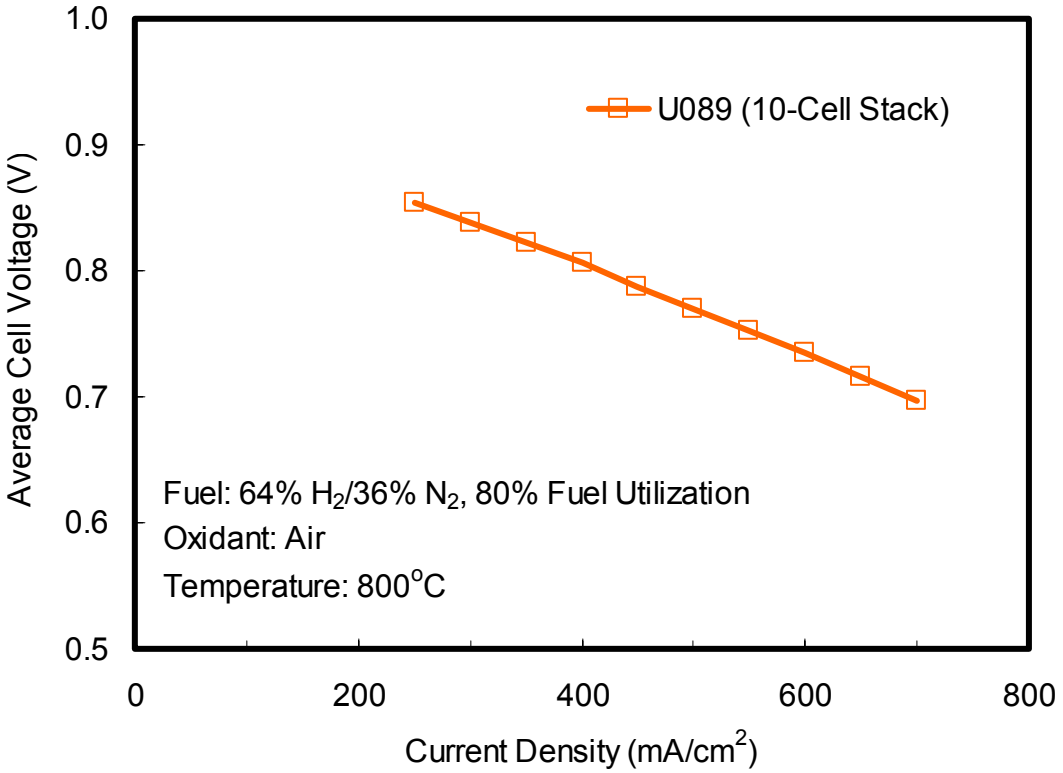

Figure 5-8 Initial performance of stack U089 tested at 800°C

Steam electrolysis for hydrogen production was measured with 30%H_2/70%H_2O feed. The stack performed very well. The average cell voltage was 1.263V at electrolysis current density of 0.62A/cm^2 and steam utilization of ~54%. At this point, the stack generated ~6.13 SLPM hydrogen with ~1.11 kW DC power input (Figure 5-9). This indicates the RSOFC stack is capable of producing hydrogen with electrical consumption of ~3.03 kW/Nm^3, comparing favorably with other electrolysis technologies.

The stack was also operated under varied modes to evaluate its long-term stability. The performance stability in terms of ASR is shown in Figure 5-10. First, the stack was tested at 0.507A/cm^2 under electrolysis with steam utilization ~45%. The performance fluctuations under steam electrolysis were due to instability of steam generation and delivery. The high steam flow coupled with limited heating capacity of the humidifier, resulted in fluctuation in steam generation rate and thus the Nernst potentials. The degradation rate was high initially, ~700 mohm-cm^2/1000 hours. It is not clear whether the steam supply issue had any measurable effect on the degradation rate. After ~300 hours, the stack was shifted to power generation mode with internal reforming. The stack was held for about 300 hours at 0.4 A/cm^2 and 60% fuel utilization with a fuel feed consisting of 30%H_2O, 20%CH_4 and 50%N_2. The addition of N_2 was to improve the stability of steam delivery. The ASR increase under power generation

mode with internal reforming appeared to be normal, in the range of 100-200 mohm-cm^2/1000 hours. The stack was then operated at 0.507 A/cm^2 for ~200 hours followed by another ~200 hours at a lower current density of 0.253A/cm^2 in electrolysis mode. The degradation rate was in the order of 100-300 mohm-cm^2/1000 hours, slower than that observed in the first 300 hours. In the last ~100 hours, the stack was operated under power generation mode with internal reforming and the stability trend was similar to that observed between hour 300 and 600.

In summary, the stack demonstration was successful. A 10-cell stack was operated over 1000 hours alternating between fuel cell and steam electrolysis modes. The stack operated very successfully with high performance of 480 mW/cm^2 at 0.7V and 80% fuel utilization in fuel cell mode, and 6 SLPM hydrogen productions in steam electrolysis mode using about 1.1 kW electrical power. The hydrogen generation is equivalent to a specific capability of 2.59 Nm^3/m^2 with electrical energy demand of 3 kWh/Nm^3. The stack performance stability has to be improved. Due to time constraint, the protective coating developed could not be implemented to the demonstration stack. It is expected that the stack performance stability will be improved with the protective coating on the oxygen electrode interconnect surfaces.

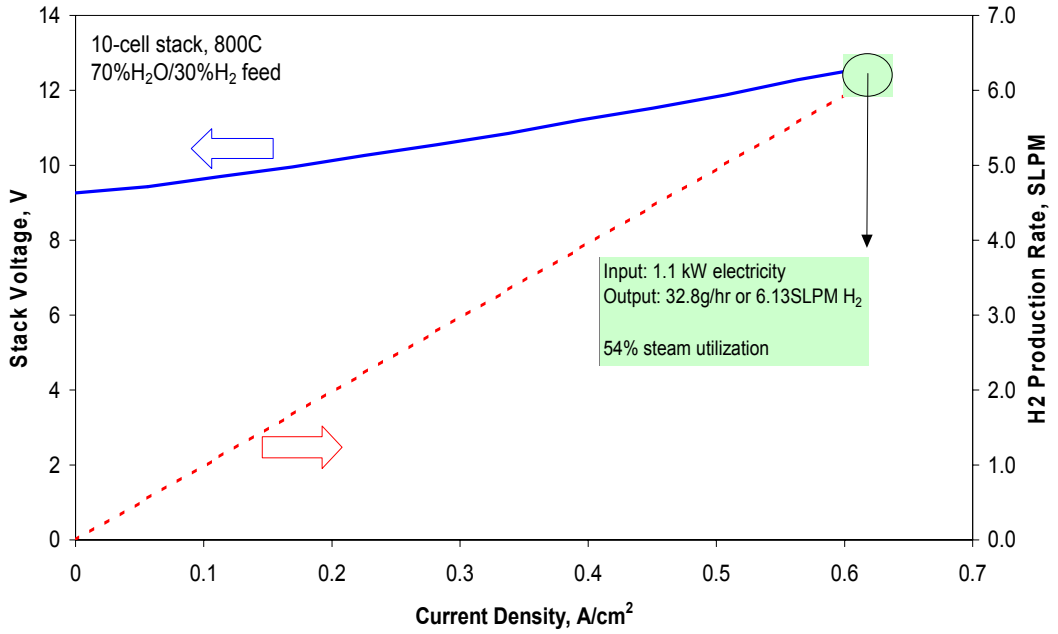

Figure 5-9 Hydrogen production with 10-cell stack

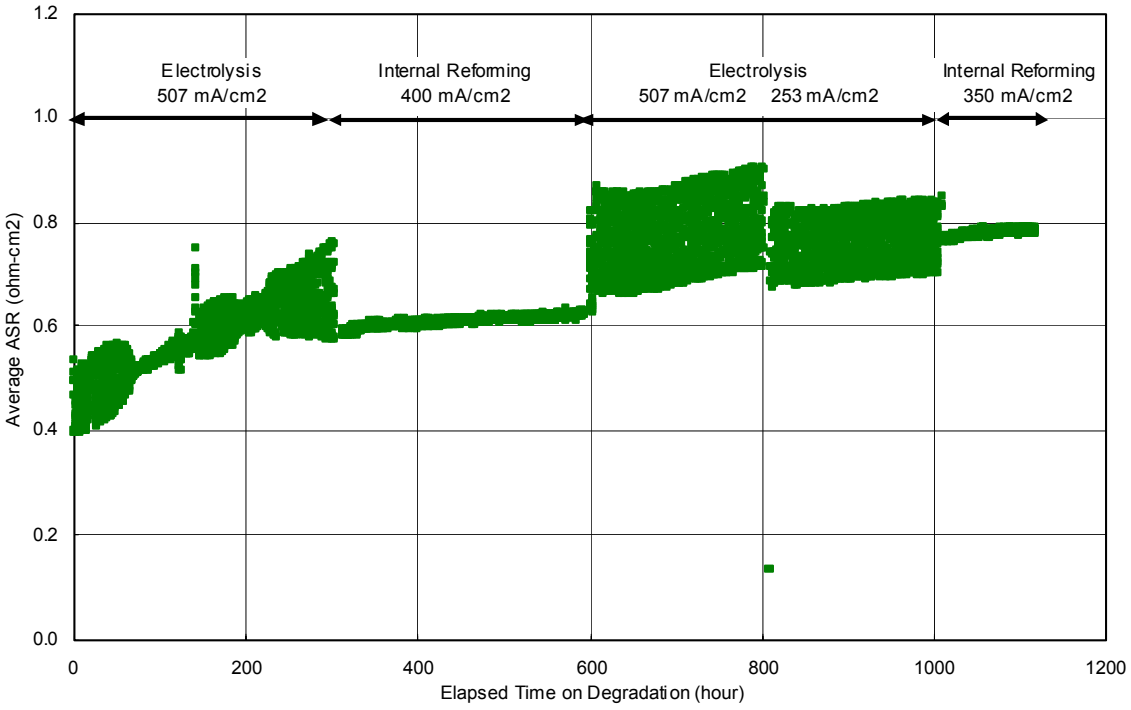

Figure 5-10 Change of average ASR of U089 10-cell stack with operation time

6 COST ESTIMATE

Study was carried out to estimate the cost of hydrogen (CoH) for a reversible solid oxide fuel cell system. The system has the potential to provide low-cost and high-efficiency production of both electricity and hydrogen. For the purposes of this analysis, this technology was analyzed for both distributed (renewable power parks and automobile refueling stations) and central station production sizes.

6.1 SYSTEM CONCEPT

The conceptual RSOFC system is given in Figure 6-1 and Figure 6-2. Figure 6-1 shows the system components operating in electrolysis mode while Figure 6-2 shows fuel cell mode operation.

In electrolysis mode, steam enters the system through a compressor and is heated through the two heat exchangers: H_2 heat exchanger and O_2 heat exchanger. The steam is then heated up to the operating temperature of 800°C through a heater before entering the solid oxide electrolyzer. This heater also provides the power needed during startup to get the steam up to the RSOFC operating temperature. Inside of the RSOFC stack, the steam is electrochemically converted to hydrogen and oxygen. Hydrogen is produced on the same side as the steam while oxygen is produced on the opposite side of the cell. The O_2 is exhausted through the O_2 heat exchanger. A

portion of the H_2 & H_2O stream is recycled back into the stack inlet while the rest enters the hot side of the H_2 heat exchanger before moving onto separation. The heat exchangers for both O_2 and H_2 provide recuperation of the heat energy of the exhaust gases. H_2 is separated from H_2O by condensing the steam with use of cooling water (not shown in diagram). The H_2 at this point is considered the product.

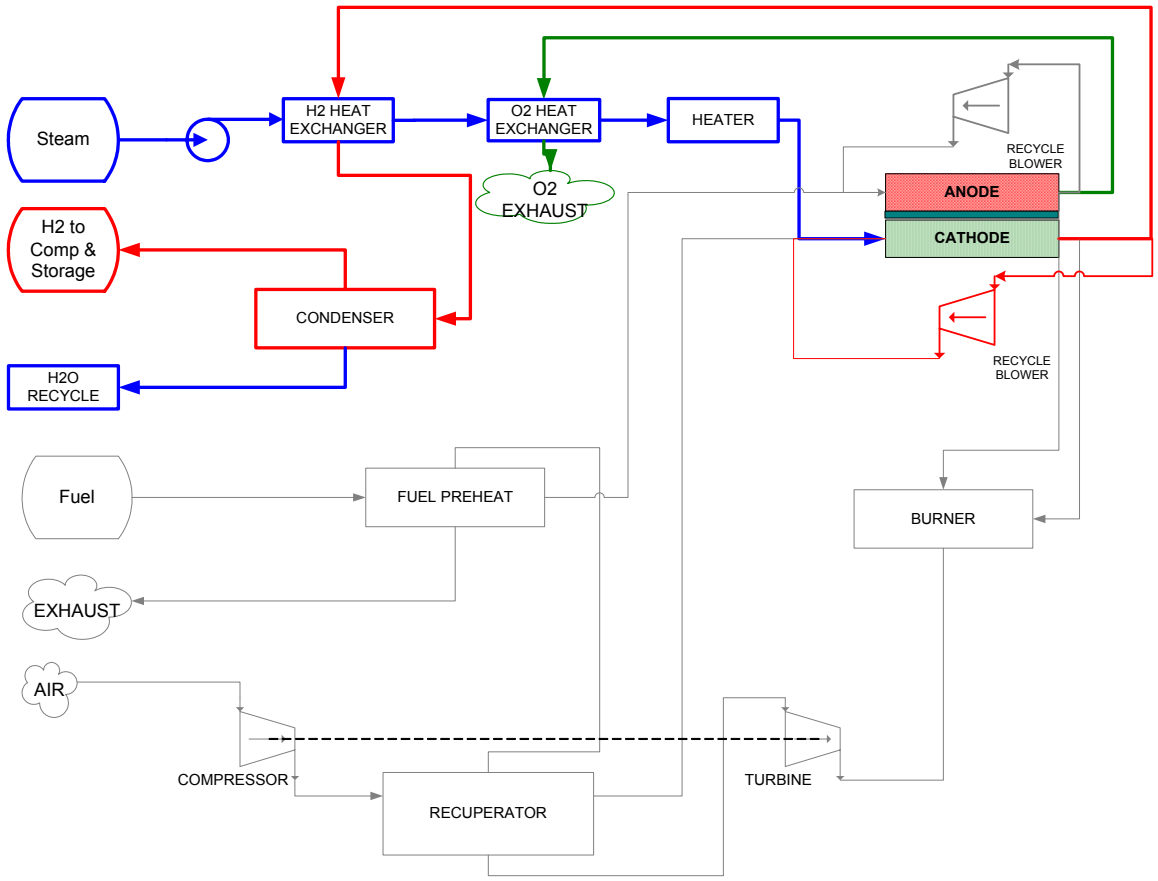

Figure 6-1 System diagram under electrolysis mode

The steam electrolysis reaction within the cell can be either an endothermic or exothermic reaction depending on the operating cell voltage. At cell voltages below ~1.3 V/cell (thermo neutral voltage), the reaction is endothermic resulting in cooler exhaust gases. The cooler exhaust gases lead to a need for more heat to bring the incoming gas stream to the desired temperature of 800°C. Also, extra heat is needed to minimize the temperature differential across the stack. Large temperature differential could cause thermal and/or structural problems in the stack. A temperature differential limit of 150°C was maintained throughout this study.

At voltages above ~1.3V/cell, the reaction is exothermic. This results in a temperature rise across the cell. Again, the temperature differential across the cell is capped at 150°C. With the exothermic reaction, the need to preheat the incoming steam is reduced, resulting in no extra heat energy needed from the heater.

The steam electrolysis reaction could also be near isothermal at 800°C, in which case the cell voltage is close to 1.3V. At this voltage, the exhaust gases temperature is the same as the incoming gases. Since the effectiveness of the heat exchangers is not 100%, a small amount of heat is still needed from the heater to bring the incoming gases to the desired inlet temperature.

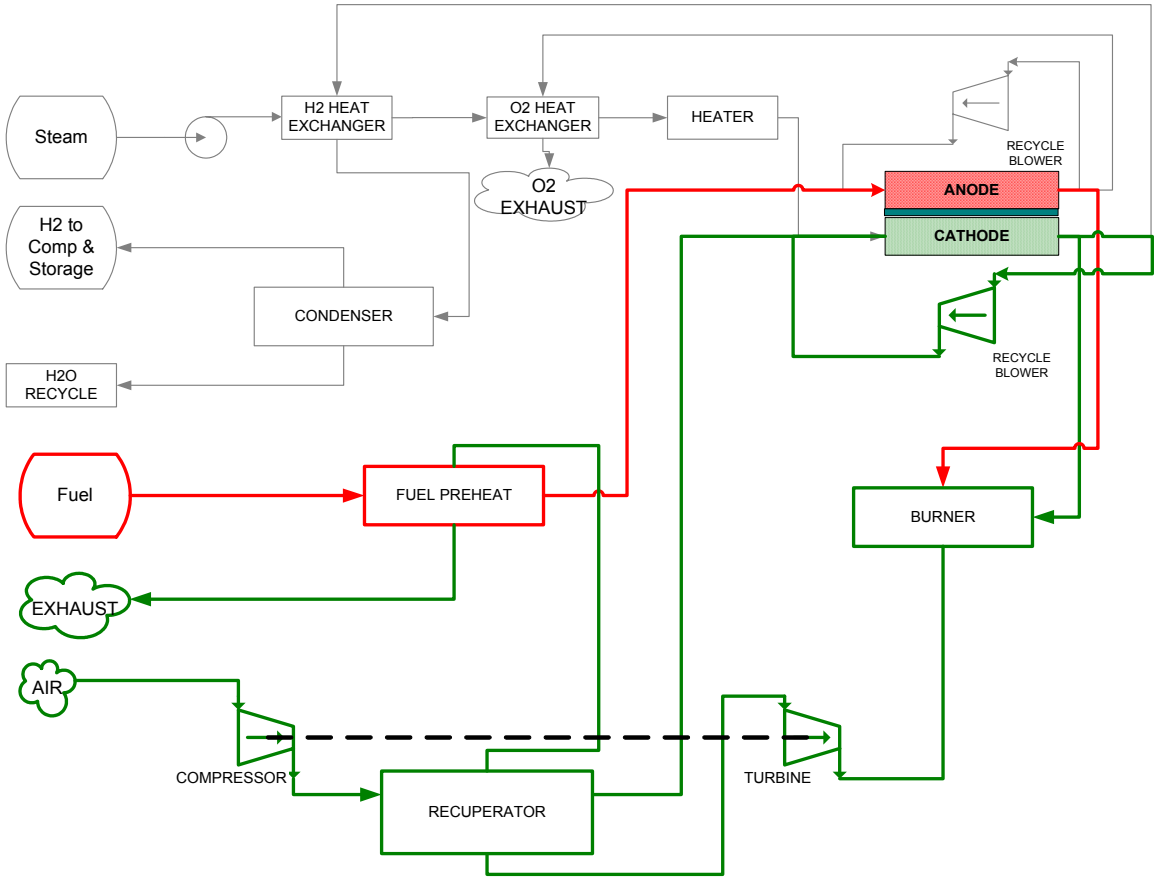

Figure 6-2 System diagram under fuel cell mode

In fuel cell mode, the fuel enters a preheat heat exchanger before entering the anode. Air enters the system through a compressor and then is heated through the recuperator. The air enters the cathode side of the SOFC, providing the reactant oxygen and heat rejection capacity needed. The oxygen ions combine with the fuel at the anode side of the fuel cell to produce H_2O and CO_2. The exiting gas out of the cathode side of the fuel cell is oxygen-lean air. This exhaust air is then split; some of it is re-circulated around to the cathode inlet via a recycle blower while the rest enters a burner. The air entering the combustor burns the excess fuel coming from the SOFC. The resulting high temperature gas is then sent through the turbine to recover the energy of the high temperature gas. This energy drives the compressor via the shaft and generates electricity. After exiting the turbine, the exhaust stream enters the hot side of the recuperator, providing the energy needed to preheat the inlet air. For the distributed station size, addition of the turbine is expensive for the amount of efficiency

gained. A more reasonable system for the distributed size does not include a turbine, which reduces the capital cost as well as the fuel cell system efficiency.

6.2 COST OF HYDROGEN MODEL ASSUMPTIONS

6.2.1 Basic Model Structure

The model is based on the DOE's H2A model used to predict the cost of hydrogen (CoH) for hydrogen production systems. There are two main modifications from the H2A model. First, there is no hydrogen compression or storage included in this study. This includes removing the capital & energy costs of the hydrogen compressor and storage tanks. Secondly, the model is set up so that the system can run and create income in electrolysis (hydrogen production) and fuel cell (electricity production) modes.

6.2.2 Financial Assumptions

The financial assumptions used are summarized in Table 6-1 below. These assumptions are consistent with those from the H2A model 1.0.11.

Table 6-1 Financial assumptions

Assumption	Distributed	Central
Assumed start-up year	2006	2006
After-tax Real IRR (%)	10.0%	10.0%
Depreciation Type	MACRS	MACRS
Depreciation Schedule Length (years)	7	20
Analysis period (years)	20	40
Plant life (years)	20	20
Inflation rate (%)	1.9%	1.9%
State Taxes (%)	6.0%	6.0%
Federal Taxes (%)	35.0%	35.0%
Total Tax Rate (%)	38.9%	38.9%
Plant Design Capacity (kg H2/day)	1,500	150,000
Operating Capacity Factor (%)	70%	90%
% Equity Financing	100%	100%
% Debt Financing	0%	0%
Units per Year	100	100
Cost of Electricity ($/kWhr)	$0.0536	$0.0536
Steam Cost ($/kg)	$0.01353	$0.01353
Cooling Water Cost ($/L)	$0.000021	$0.000021
Natural Gas Price ($/MMBTU)	$5.66	$5.66

6.2.3 Stack Cost

The preliminary stack cost is based on the estimate of cost done under the Cooperative Agreement (DE-FC26-01NT41245) for the U. S. Department of Energy/ National Energy Technology Laboratory (DOE/NETL) entitled "Solid State Energy Conversion Alliance (SECA) Solid Oxide Fuel Cell Program". The cost estimate for this program was scaled using the production volumes given in Table 6-1 and a cell length

of 24 inches (square shape). The resulting preliminary cost of the assembled stack is $255/kW for fuel cell mode.

In the cost estimate, the RSOFC stack life was assumed as 5 years. Since this model assumes a 20-year evaluation period for the distributed case, the stack replacement cost is added to the capital costs at the beginning of years 1, 6, 11, and 16.

6.2.4 System Costs

Along with the stack, the balance of plant (BOP) cost makes up the majority of the capital cost. Estimate of equipment cost is based on a reference cost and reference duty. An exponential formulation is used to scale it to the desired duty. The reference duty is selected to be as close to the desired duty as possible.

$$\frac{\cos t}{\cos t\_ref} = \left(\frac{duty1}{duty\_ref1}\right)^{N1}\left(\frac{duty2}{duty\_ref2}\right)^{N2}\left(\frac{duty3}{duty\_ref3}\right)^{N3}$$

For majority of components, N_i is assumed as 0.7. The BOP component cost was divided into 3 subcategories; fuel cell mode components, electrolysis mode components, and overall system components. The fuel cell mode components include air compressor, heat exchangers, power electronics and other components that are only used in fuel cell mode. Likewise, the electrolysis mode components include only those used in electrolysis mode. The overall system components are components that are needed in both modes, such as the pressure vessel for the stack, skid packaging, electronics, and common controls.

These BOP cost is totaled up and 20% is added on to transition from delivered to installed component price. The O&M costs are assumed to be 7% of the capital costs.

6.2.5 Feedstock Costs

6.2.5.1 Electrolysis Mode Feedstocks

For electrolysis mode, the feedstocks are steam, cooling water, electricity, and a heat source for the heater. Two different types of heat sources for the heater were analyzed, natural gas fired and electrical. The amount of steam required is determined by the hydrogen production rate (1500 kg/day for distributed and 150,000 kg/day for central) and the steam utilization (baseline of 80%). The cooling water need is determined to drop the hydrogen stream exhaust to 60°C while maintaining a 10°C increase in temperature for the water.

The electricity used for the electrolysis of steam is dependent upon the cell voltage of the electrolysis stack and the hydrogen production rate. The lower the voltage, the lower amount of electricity is needed to produce a given quantity of H_2. The electrical power needed for the electrolysis, along with the total including the power

need for heater and furnace, is shown in Figure 6-3. On top of the electrolyzer stack power given in Figure 6-3, a 3% power supply loss was taken into account, which increased the electrical power for the electrolysis by 3%. The amount of heat energy needed from the heater varies, depending on the cell voltage. Below ~1.4V, the heat is used to increase the input gas temperature to 800°C as well as to keep the stack exhaust from falling below 650°C. A furnace can be used to heat the stack to keep the temperature differential across the stack to 150°C for the endothermic reaction. In the voltage range of 1.25-1.4V, the total energy needed is insensitive to the operating voltage. Above ~1.4V, no additional heat is needed for the system and additional cooling capability might be necessary to reduce the stack temperature gradient. When the cell voltage is greater than 1.4V, the total amount of energy required increases with the cell voltage.

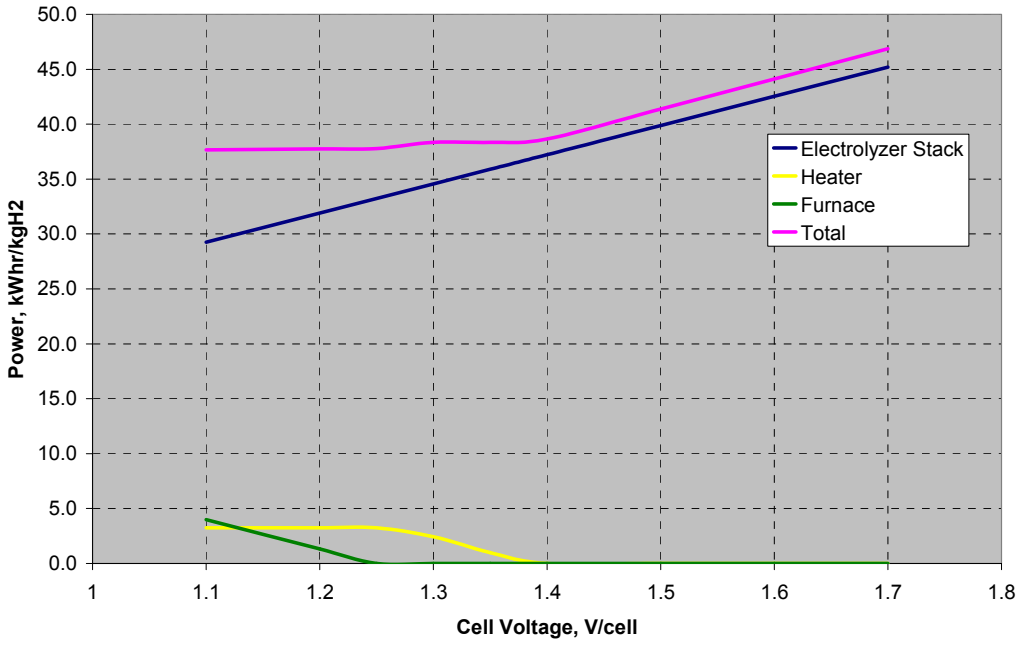

Figure 6-3 SOEC Feedstock Energy

The heater and the furnace could be electrical or natural gas fired. Based on the prices in Table 6-1, the total energy feedstock cost can be expressed in \$/kg H_2 as shown in Figure 6-4. The natural gas fired heater and furnace show a reduced cost because of the lower cost of natural gas in comparison with electrical heater and furnace. To reduce the feedstock cost, one can use natural gas as the heat source and lower the cell voltage. However, as the cell voltage decreases, the current density also decreases. The lower current density requires more active area (either larger cells or a greater number of cells) for a fixed amount of hydrogen production, leading to increased stack capital cost.

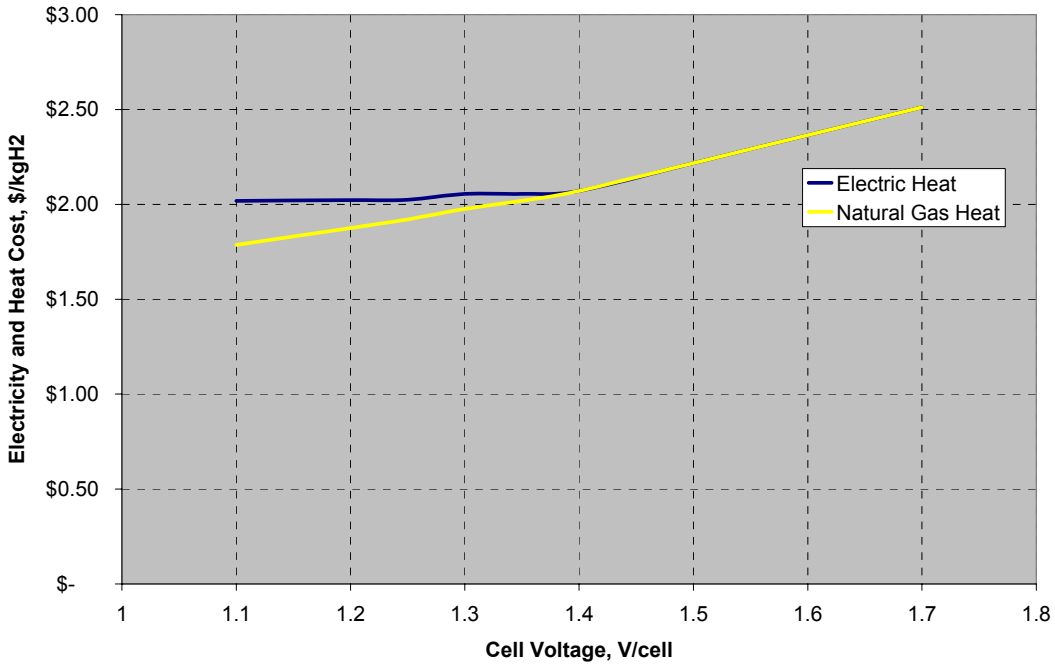

Figure 6-4 Energy feedstock cost for electrolysis

6.2.5.2 Fuel Cell Mode Feedstocks

For fuel cell mode, the main feedstock is natural gas. The amount of natural gas used depends on the efficiency of the system. Steam for reforming is also considered as a feedstock in this analysis.

6.3 RESULTS & DISCUSSION

Analysis was performed under two plant sizes: distributed size (1,500 kg H_2/day) and central station size (150,000 kg H_2/day). The operation modes were assumed as (1) electrolysis mode, (2) power generation mode, and (3) dual mode. Cost estimate under electrolysis mode was also compared with other water electrolysis technologies.

6.3.1 Distributed Electrolysis System

Cell operating voltage influences both energy feedstock cost and stack capital cost. Figure 6-5 shows the optimization of the cell voltage against the calculated cost of hydrogen. The minimum cost is around 1.2 V/cell at \$3.70/kgH_2. Above this voltage, the cost of the extra energy needed outweighs the decrease in stack capital cost. Below ~1.2 V/cell, the extra capital expenditure for the stack outweighs the decrease in energy costs. From this point, all of the distributed electrolysis cases assume 1.2 V/cell as the operating voltage.

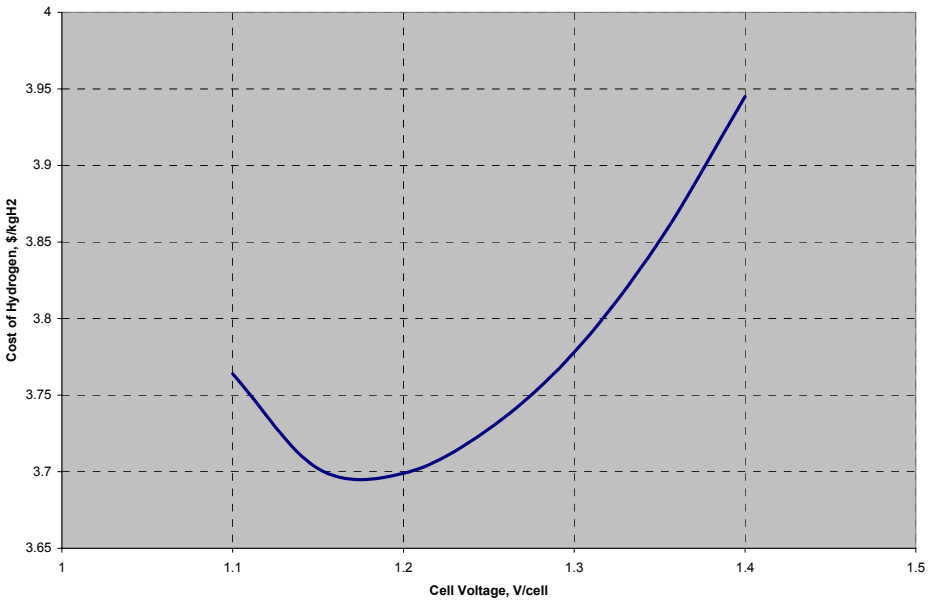

Figure 6-5 Cost of hydrogen production against average cell voltage

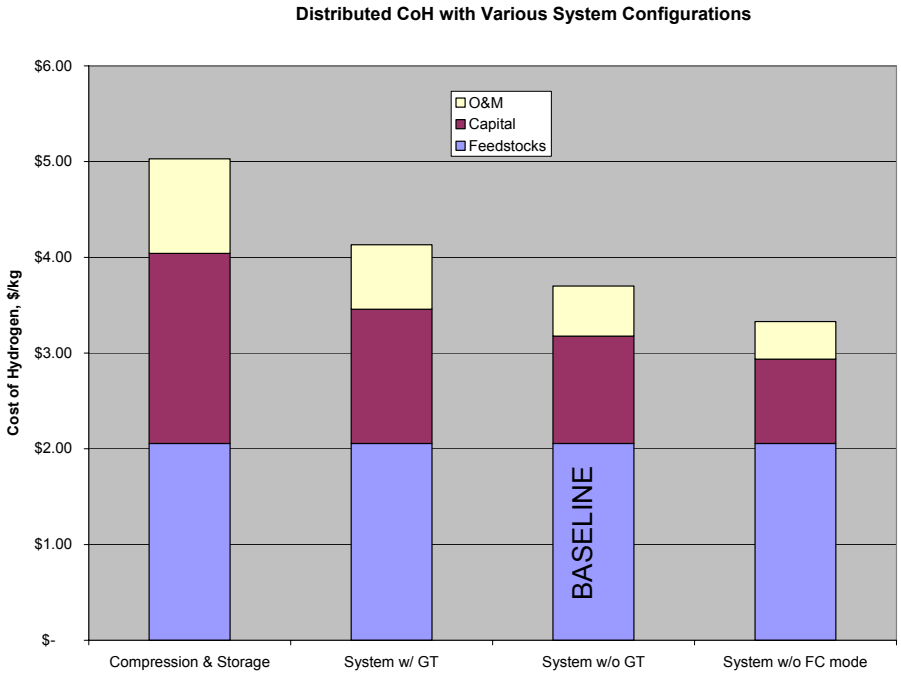

Figure 6-6 Distributed CoH with various system configurations

The baseline CoH for a distributed RSOFC system running in electrolysis mode is \$3.70/kgH_2. The baseline RSOFC system has fuel cell components but has no gas turbine. It doesn't include compression or storage components for hydrogen either.

Figure 6-6 shows the cost of hydrogen in baseline case along with other cases. Please note that this figure is a waterfall chart, meaning the initial value is increased or decreased by a series of intermediate values. For the baseline CoH, greater than 50% of the cost comes from the feedstock cost while the rest is mainly made up of the capital cost. Toward the left of the baseline of $\$3.70/kgH_2$, adding the gas turbine increases the CoH by ~$\$0.40/kgH_2$, from the increase in capital and O&M cost. Adding the compression and storage increases the capital and O&M further, pushing the CoH ~ $\$5/kgH_2$. Going to the right of the baseline, removing fuel cell mode components would decrease the CoH by 10%, giving a cost estimate of ~$\$3.3/kgH_2$ for an electrolysis system alone.

Figure 6-7 and Figure 6-8 show the breakdown of the feedstock and capital cost, respectively. The feedstock cost is dominated by the cost of the electricity needed to drive the electrolysis reaction within the stack. The other main contributors are the steam and natural gas cost (used in external heater). The capital cost breakdown for the baseline value is pretty much evenly distributed in the four categories: stack, electrolysis components, fuel cell components, and overall balance of system components that would be needed for either electrolysis or fuel cell mode operation.

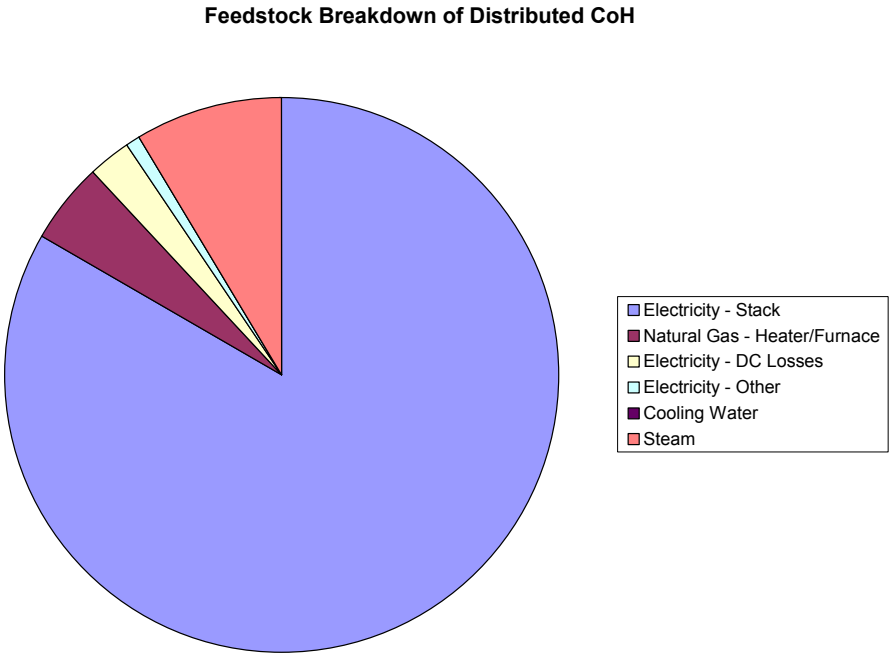

Figure 6-7 Feedstock breakdown for distributed CoH

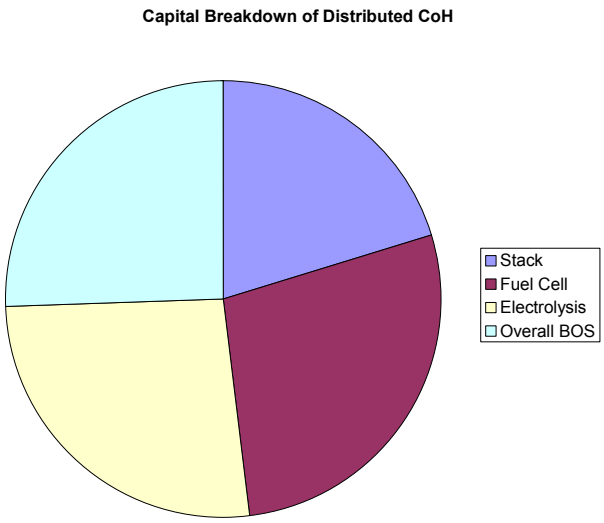

Figure 6-8 Capital breakdown for distributed CoH

CoH sensitivity analysis was also conducted in the distributed case. Figure 6-9 shows the sensitivities of various parameters to the CoH at the baseline point of \$3.70/kgH_2. Each parameter is changed independently of the others and its effect on CoH is plotted. The wider the bar, the larger effect the parameter has on the CoH. As can be seen, the biggest sensitivity belongs to the cost of electricity (CoE). This is expected as the feedstock portion of the CoH is mostly made up of electricity cost. Increasing the capacity factor, reducing the internal rate of return, or increasing the stack power density all result in large impacts on reducing the CoH.

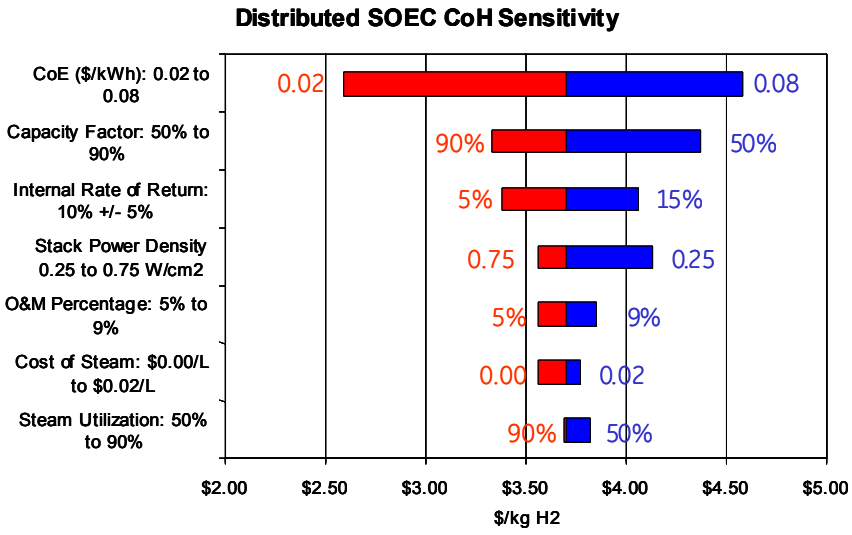

Figure 6-9 CoH sensitivities for distributed size case

6.3.2 Distributed Dual Mode

One benefit of a reversible system is that the system can run in both electrolysis mode and fuel cell mode producing hydrogen or electricity, respectively. In the previous section, CoH was analyzed with the assumption that the system ran in electrolysis mode exclusively, giving a hydrogen production cost of \$3.7/kgH_2. Assuming that the system runs in power generation mode exclusively, it would result in a cost of electricity (CoE) of just above \$0.10/kWhr with natural gas as the input. These two points are shown in Figure 6-10. In the figure, the X-axis is the percentage of operating time that the system runs in electrolysis mode, ranging from 0 to 1 (meaning 100%). A possibility to reduce the CoH is to run in fuel cell mode during the hours when the electricity demand (and selling point) is high. Therefore, one can sell electricity at a higher price to help reduce the cost of the hydrogen. The curve shows the selling price of electricity to reduce the CoH to \$3.50/kgH_2, a \$0.2/KgH_2 reduction from the baseline. As the percentage of time running in electrolysis mode (as opposed to fuel cell mode) increases, the electricity selling point must continue to rise. Likewise, if the hydrogen could actually be sold for more than \$3.70/kg, then the curve of would show the opposite, dropping CoE below \$0.10/kWhr.

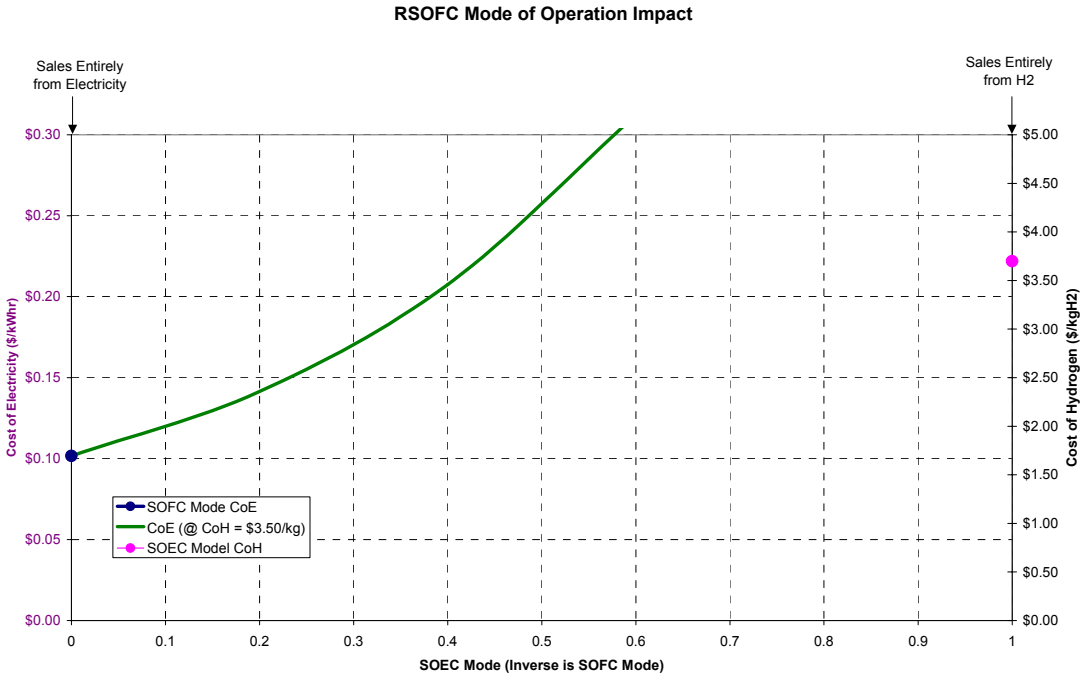

Figure 6-10 Impact of RSOFC operation mode on CoH

6.3.3 Central Electrolysis System

The central station size is assumed as 150,000 kg H_2/day, 100x larger than the distributed production rate. With this large size, the capital cost portion of the CoH is reduced because the balance of plant components scale favorably with size. Due to the smaller impact of the capital cost, addition of the turbine does not increase CoH much while it can provide a much higher SOFC system efficiency. Also, since the feedstock cost and stack cost are unchanged from the distributed case, a cell voltage of 1.2V is again selected. Figure 6-11 shows the breakdown of CoH of various system configurations. The first column shows the distributed baseline case of \$3.70/kg H_2. Moving to the right, the central station case with no turbine results in a lower CoH due to the drop in capital and O&M portion of the CoH. Adding the gas turbine only adds a few cents to the CoH. Removing the fuel cell components also doesn't result in a big difference in CoH. The last column shows the effect of removing the cost of the steam and heat (for heater and furnace) if the central station system were able to integrate within an industrial plant. This reduces the feedstocks cost and can drop the CoH to around \$2.30/kgH_2.

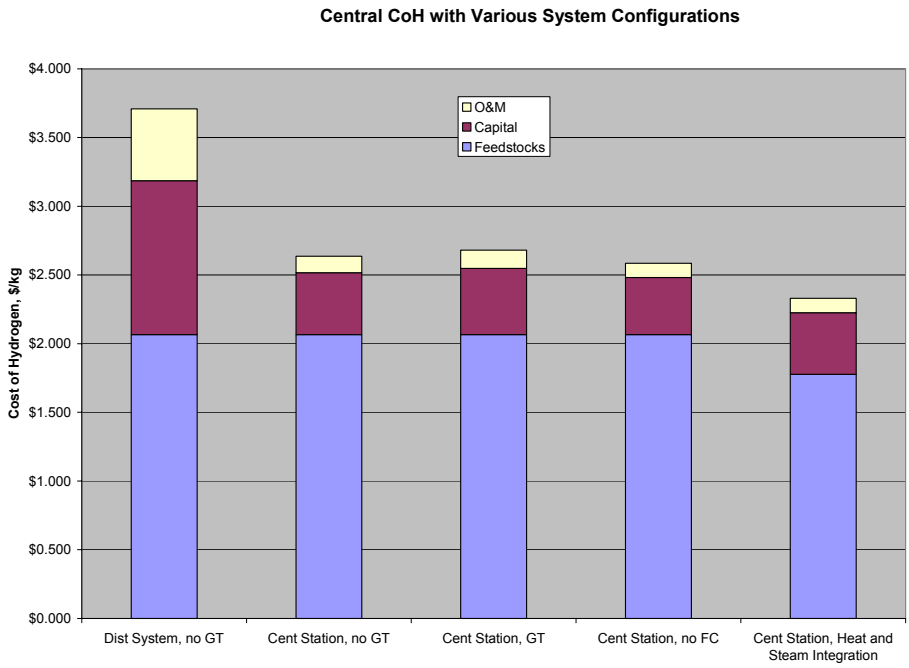

Figure 6-11 CoH for various system configurations with central station sizes

The capital cost breakdown for a central station with turbine is given in Figure 6-12. The breakdown is much different from the distributed system. More than half of the capital cost in the central station attributed to the stack cost. This is because the cost of the stack does not reduce with the plant size while the other balance of system components scale favorably as the volume becomes larger.

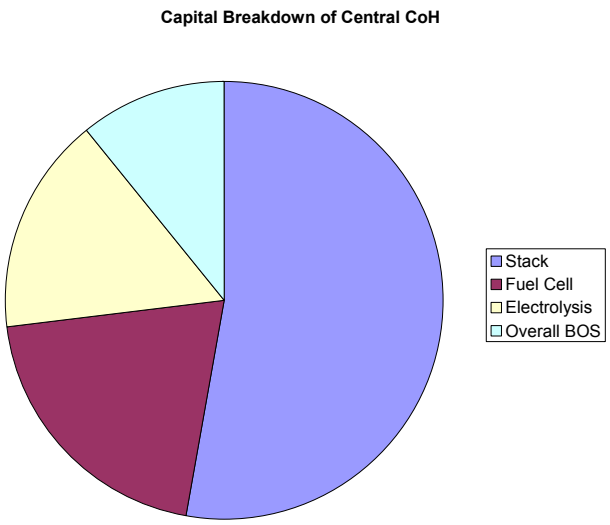

Figure 6-12 Capital cost breakdowns for central station case

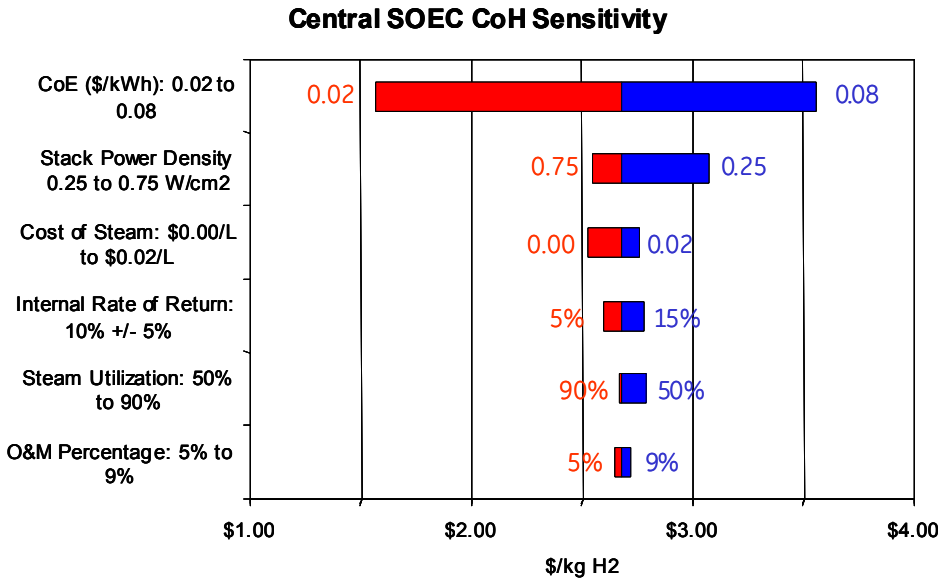

Figure 6-13 CoH sensitivities for central station case

CoH sensitivity analysis for central station case was also conducted (

Figure 6-13). The baseline point of central station CoH with the gas turbine is \$2.68/kgH_2. Each parameter is changed independently of the others and its effect on the CoH is plotted. The wider the bar, the larger effect the parameter has on the CoH.

The biggest sensitivity again belongs to the cost of electricity. This is expected as the feedstock portion of the CoH is mostly made up of electricity cost. The stack performance also has a large impact due to the larger portion of the stack costs to the capital.

6.3.4 Central Dual Mode

Similar to the distributed size RSOFC, the system can run under power generation mode alone. Running power generation mode exclusively would result in a cost of electricity (CoE) of just below $0.06/kWhr with natural gas as input. As discussed earlier, the baseline point of central station CoH with the gas turbine is $2.68/kg$H_2$. A possibility to reduce the CoH is to run in fuel cell mode during the hours when the electricity demand (and selling point) is high. Therefore, one can sell electricity at a higher price to help reduce the overall cost of the hydrogen. Figure 6-14 shows a curve of what the electricity-selling price must be so that the CoH from the dual mode system will be reduced to $2.00/kg$H_2$. As the operating percentage of electrolysis mode increases, the percentage of power generation mode will decrease and the electricity selling point must continue to rise to drive the overall CoH to $2.00/kg. Likewise, if the hydrogen could actually be sold for more than $2.68/kg, then the curve of selling price of electricity would show the opposite, dropping the CoE below $0.06/kWhr.

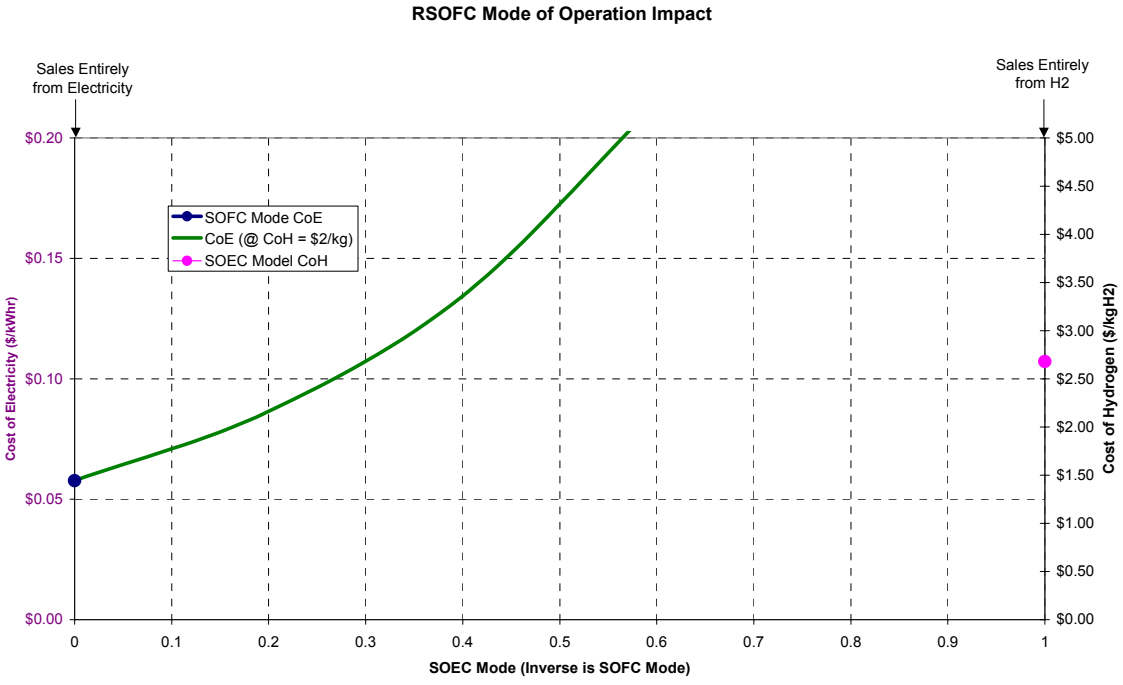

Figure 6-14. Impact of RSOFC operation mode on CoH

6.3.5 Peak Shaving

Another possible configuration is peak shaving. The idea is to sell electricity during the day while the electricity rate is high and to make hydrogen at night when it is inexpensive to buy electricity. The difference between this and the central dual mode in section 6.3.4 is that the hydrogen made at night becomes the fuel for the fuel cell during the day. Therefore, the only product to sell from this scenario is the electricity as the hydrogen is totally consumed by the system. Table 6-2 gives the results of peak shaving by running exactly long enough in fuel cell mode to use all of the hydrogen produced in electrolysis mode.

Table 6-2 Peak shaving results

	SOEC Electricity $0.05/kW hr	SOEC Electricity $0.02/kW hr
Distributed	**$0.28/kWh**	**$0.22/kWh**
Central	**$0.21/kWh**	**$0.15/kWh**

The results show that for purchasing electricity at $0.05/kWhr at night, the selling price during the day would have to be $0.28/kWhr for distributed and $0.21/kWhr for the central station to make economical sense. Similar results are shown for purchasing electricity at $0.02/kWhr at night. The results indicates that this type of peak shaving configuration only makes sense when there is a large difference in the CoE between day and night.

6.3.6 Electrolysis System CoH Comparisons

Since a RSOFC system has components for both fuel cell mode and electrolysis mode, it adds extra capital cost compared to those electrolysis systems that just produce hydrogen, namely Alkaline and proton exchange membrane (PEM) electrolysis system. Therefore, for the purposes of this comparison, the CoH is based on an electrolysis system with no specific fuel cell components present (SOEC). Also, the compression and storage cost of the product H_2 was excluded for all three electrolysis systems. The cell voltage for Alkaline, PEM, and SOEC are assumed as 1.65, 1.5, and 1.2 V/cell, respectively. The CoE is assumed as $0.0536/kWhr. Since the different electrolysis technologies operate at different cell voltages, the amount of power needed to produce the same amount of hydrogen varies. The stack cost is normalized in $/kg$H_2$ per day based on performance at the operating voltage and stack materials cost. Shown in Table 6-3 are cell voltage, electrolysis electricity requirement, and stack cost for the different electrolysis technologies.

Table 6-3 Cell voltage, electrolysis electricity requirement, and stack cost assumptions

	Cell Voltage	Electrolysis Electricity	Stack Cost
Technology	V/cell	kW-hr/kgH2	$/kgH2 per day
Alkaline	1.65	43.9	$ 183
PEM	1.5	39.9	$ 665
SOEC	1.2	31.9	$ 247

The alkaline electrolysis stack operates at the highest voltage and therefore needs the greatest amount of electricity to operate the stack. However, the stack is the lowest cost because of inexpensive materials. PEM has a mid range cell voltage but the capital cost of the stack is expensive. SOEC has the lowest electricity needed due to the low voltage but has a stack cost in between that of PEM and Alkaline. These stack cost estimates are predictions with large uncertainties. As these costs change, so do the results of the CoH that is presented below.

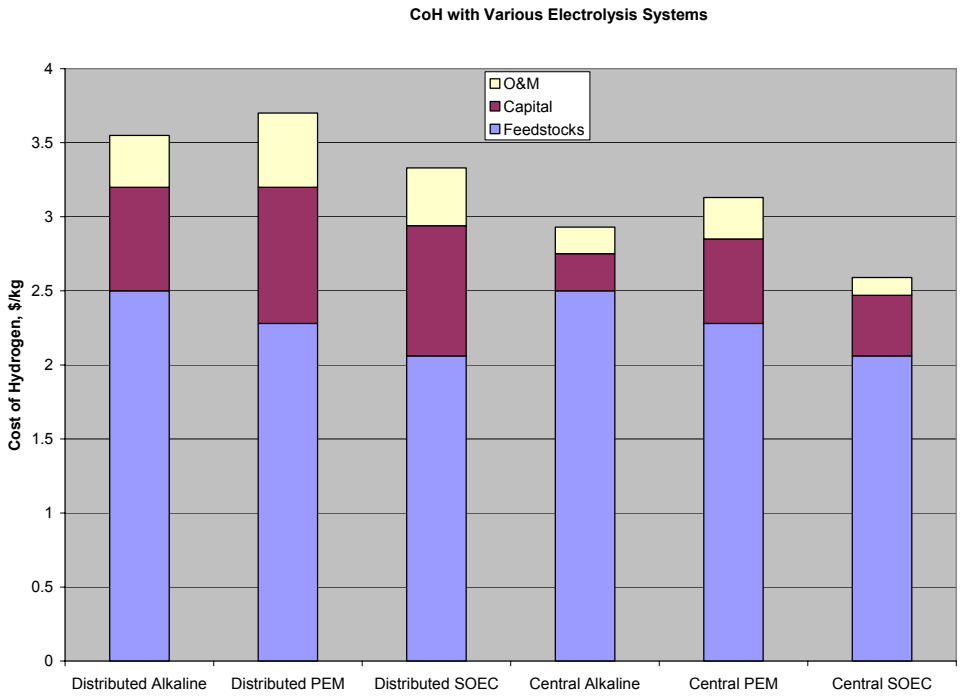

Figure 6-15 CoH comparisons across electrolysis technologies

Figure 6-15 gives the breakdown of CoH for the 3 different types of electrolyzers with both distributed and central station sizes. For the distributed case, SOEC has the lowest overall cost due to its much lower feedstock costs (operating at lower voltage). Following SOEC is Alkaline. Even though it has the highest feedstock cost, it has a much lower capital cost. PEM is the highest in this analysis due to its large capital cost. However, one benefit of PEM electrolysis is its ability to electrochemically pressurize the hydrogen product, thus offering potentials to reduce the compression cost, which was

not accounted for in this analysis. Once again, the CoH are dependent upon the assumptions on cell voltage and stack cost. If the electricity price were lowered, the difference between SOEC and Alkaline would become smaller, as the alkaline feedstock cost would reduce faster than the SOEC feedstock cost.

Looking at the central station cases, the SOEC again has the lowest CoH. This is because the feedstock costs play such a large portion of the CoH that the lower operating voltage definitely has an advantage. Because the PEM stack is much more expensive, once again it shows the highest cost.

6.4 SUMMARY

A CoH model was developed based on the DOE's H2A model with conceptual systems. The CoH for RSOFC systems was studied at both distributed and central station size. It was found that the optimal cell operating voltage of the solid oxide electrolyzer was around 1.2 V/cell and the extra heat needed should be provided via a non-electrical heater/furnace, such as a gas heater/furnace.

For the distributed size, the CoH was estimated at \$3.70/kgH_2 with a RSOFC system. The cost breakdown shows that the feedstock costs are mainly made up of the electricity cost while the capital cost breakdown is split relatively equally among the stack, electrolysis mode components, fuel cell mode components, and overall shared components. The sensitivity analysis shows that the cost of electricity is the largest driver of cost followed by the capacity factor, internal rate of return, and stack power density.

For a central station size, the CoH was estimated at \$2.68/kgH_2. The feedstock cost breakdown is the same as the distributed case but the capital breakdown is dominated by the stack cost. The reduction in overall CoH is attributed to the reduction of balance of plants cost. Integration of the heat and steam production within an industrial plant would reduce the CoH by more than 10%. Again, the sensitivity analysis indicates that CoH is most sensitive to the cost of electricity.

Running the system under dual mode, producing both hydrogen and electricity as products was also analyzed. To be able to reduce the CoH, the electricity must be sold for a higher price than that the system could produce if running in fuel cell mode only. That is, if running in fuel cell mode exclusively and a CoE selling point is \$0.06/kWhr, the CoE must be sold for more than that if the system runs in both modes to reduce the CoH.

Another possibility is to run the system in a peak shaving mode. This is to produce hydrogen at night with low cost electricity and use this hydrogen for power generation with fuel cell during the day. The electricity from the fuel cell mode will be the final product from the system. The result indicates that the peak shaving mode only makes sense when the electricity rate differentials are large enough (\$0.15 to \$0.20/kWhr) between day and night.

A comparison with Alkaline and PEM electrolysis shows that SOEC has the lowest feedstock cost due to the lowest operating voltage. Alkaline has the lowest capital costs due to relatively inexpensive materials. PEM has the highest CoH. Under the assumptions in this study, the solid oxide electrolysis system shows the lowest CoH for both distributed and central station sizes.

7 TECHNOLOGY ASSSESSMENT

As a commodity chemical used in the refining and petrochemical industries, hydrogen is now treated as the energy carrier for the future because it can be directly used as fuel with virtually no emission. However, hydrogen is not a primary energy source since it is not available in nature and cannot be directly collected from nature for consumption. Hydrogen is an ENERGY CARRIER like electricity in the energy industry. It can only be produced from naturally existing resources i.e. primary energy sources, such as coal, petroleum, natural gas, and nuclear energy, secondary energy sources through electrolysis, and from renewable sources such as biomass, wind, hydro and solar power. Figure 7-1 [23] shows processing options for the hydrogen production from different energy sources. The feasibility of economical production of hydrogen in large-scale depends on the availability of energy sources and the efficiency and maturity of processing technologies. Integration of nuclear power, renewable energy with water electrolysis provides a sustainable hydrogen production option [24, 25].

The technology assessment, focusing on the water electrolysis and steam reforming technologies, includes overview of each technology and a technological comparative analysis of RSOFC versus other electrolysis systems (alkaline and PEM) and steam reforming for hydrogen production. It also includes the technology gaps for commercializing RSOFC technologies and a technology roadmap to bridge the gaps.

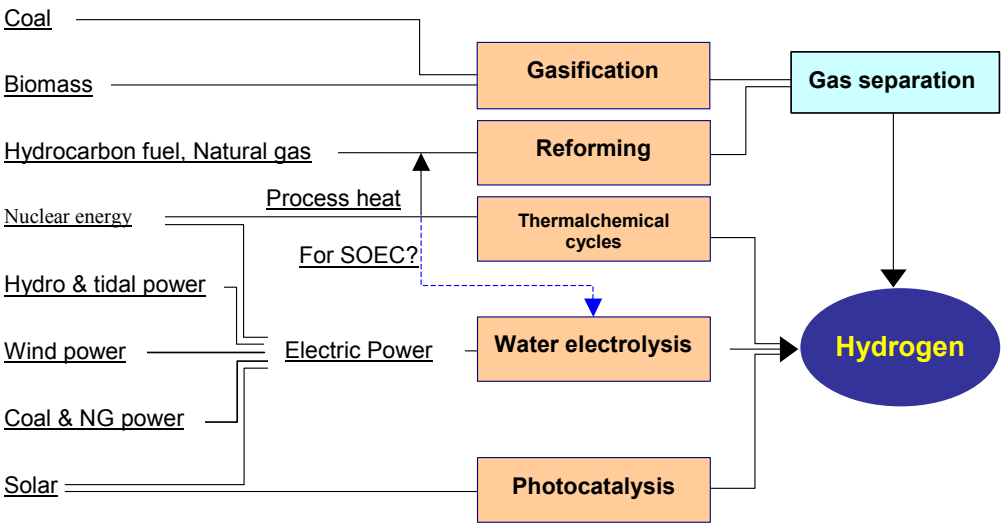

Figure 7-1 Energy sources and processing options for hydrogen production

7.1 STEAM REFORMING OF NATURAL GAS

7.1.1 Thermodynamics of Steam Reforming

As the most commonly used process to produce hydrogen or hydrogen rich gases, steam reforming converts hydrocarbons with steam to hydrogen and carbon dioxide. Potential fuels that can be converted to hydrogen are listed in Table 7-1. The general reaction of steam reforming of hydrocarbons can be described as

$$C_nH_m + 2nH_2O \rightarrow nCO_2 + (0.5m + 2n)H_2$$

This overall reaction consists of a series of elementary reactions. For example, reaction of the methane (the major component in natural gas) steam reforming can be described as endothermic reforming reactions:

$$CH_4 + H_2O_{(g)} \Leftrightarrow CO + 3H_2 \qquad \Delta H=206 \text{ kJ/mol}$$

and exothermic water-gas-shift reaction

$$CO + H_2O_{(g)} \Leftrightarrow CO_2 + H_2 \qquad \Delta H=-41 \text{ kJ/mol}$$

The overall process is endothermic. Since water is in the liquid state at room temperature and the steam reforming occurred at high temperature where water is in the vapor state, additional energy is required to convert water from liquid to steam.

Table 7-1 Potential fuels for steam reforming

Methane (CH_4):	Expensive, not readily available
Natural Gas:	Relatively inexpensive, contains sulfurous compounds, good infrastructure
Methanol (CH_3OH):	Relatively expensive, not readily available, poor infrastructure at present
Ethanol (CH_3CH_2OH):	Relatively expensive, not readily available, poor infrastructure
Gasoline	Inexpensive, readily available, mature infrastructure, contains sulfurous compounds
Logistics Fuels (e.g. JP-8):	Inexpensive, readily available, poor infrastructure, contains sulfurous compounds
Naphtha:	Inexpensive, not readily available, poor infrastructure, contains sulfurous compounds
Diesel:	Inexpensive, readily available, mature infrastructure, contains sulfurous compounds

7.1.2 Thermal Efficiency of Steam Reforming

The thermal efficiency of steam reforming is defined as the energy content of product gas divided by the energy input into the steam reforming system. Due to the

difference in the definition of system boundaries and energy inputs, there are several ways to calculate the thermal efficiency of steam reforming [26]. Assuming the steam reforming reaction is 100% in completion, the maximum thermal efficiency of steam reforming without considering the external heat can be described as

$$\eta_{\max.} = \frac{x\Delta H_{H_2}}{\Delta H_{fuel}}$$

where x is the number of moles of hydrogen produced from a mole of fuel, ΔH_{H2} represents the low heating value per mole of hydrogen, and ΔH_{fuel} is the lower heating value per mole of fuel consumed.

Since additional heat is required for the endothermic reaction and conversion of liquid water to steam, the maximum thermal efficiency above is an overly optimistic measure of thermal efficiency. To account for the additional heat, the thermal efficiency of steam reforming can be reasonably defined as

$$\eta_a = \frac{x\Delta H_{H_2}}{\Delta H_{fuel} + Q_{in}}$$

or

$$\eta_a = \frac{(1-y)x\Delta H_{H_2}}{\Delta H_{fuel}} \quad or \quad \frac{x\Delta H_{H_2} - Q_{in}}{\Delta H_{fuel}}$$

where Q_{in} is the heat required for the steam reforming process and vaporization of water, y represent the fraction of hydrogen to be burned to provide the heat, Q_{in}.

Table 7-2 Thermal efficiency entitlements of methane steam reforming

Description	Efficiency	Comments
$\eta_{\max.} = \frac{x\Delta H_{H_2}}{\Delta H_{fuel}}$	120.6%	Maximum entitlement of steam reforming without considering the heat for steam reforming process and vaporization of water
$\eta_a = \frac{x\Delta H_{H_2}}{\Delta H_{fuel} + Q_{in}}$	91.7%	Entitlement of steam reforming with consideration of heat supplied externally for steam reforming process and vaporization of water
$\eta_a = \frac{x\Delta H_{H_2} - Q_{in}}{\Delta H_{fuel}}$	89%	Entitlement of steam reforming with consideration of heat generated from product gas for steam reforming process and vaporization of water

Table 7-2 shows the entitlements of the methane steam reforming where lower heating values are used. The efficiency for a practical steam reforming system has to be calculated based on composition of product gas, feedstock, heat loss, and sources

of heat. The overall efficiency of existing plants is in the range of 70-80 % in comparison with 89% or 92% of efficiency entitlement.

7.1.3 Carbon Formation

The carbon formation in steam reforming system is often referred as coking. Carbon may form on catalyst, reactor container, and gas pipes, depending upon temperature, steam level, and catalyst type. The coking can be prevented by increasing the levels of steam, i.e. steam to carbon ratio, or alleviated by special catalysts and/or supports. Normally steam reformers operate with steam-carbon ratios larger than 2-3 to protect the reformer catalyst and the downstream pathways from carbon formation.

7.1.4 Reformer and System Design

A simplified flow diagram of steam reforming process is shown in Figure 7-2. The main components of a steam reforming system are:

- Heat exchanges for feedstock heating and heat recovering
- Desulfurizer
- Steam generator
- Steam reformer
- Combustor for heat generation
- Product gas separator

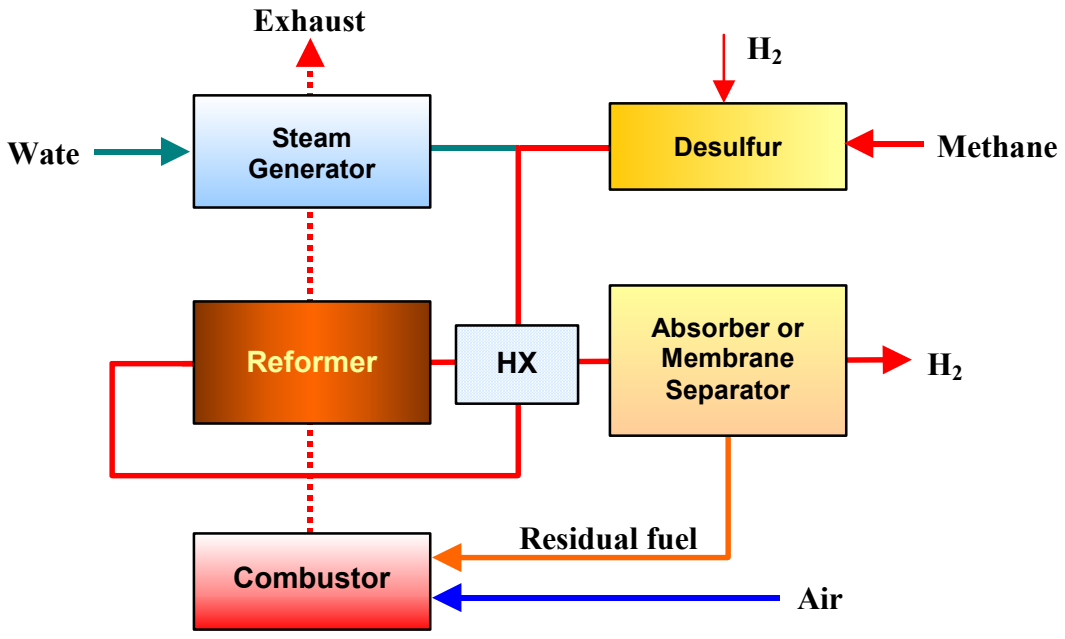

Figure 7-2 A simplified flow diagram of steam reforming process

To achieve high methane conversion, industry scale steam reforming processes are normally operated at temperatures around 750 to 850 °C and pressures in the order of 30 atm. Since the product gases from steam reforming contain carbon dioxide, water vapor, and residual CH_4, absorption or membrane separation methods and condenser are used to remove carbon dioxide and other unwanted components from product gases. The resulted product may be further cleaned depending on the requirement. The residual gas that consists of mainly carbon monoxide, hydrogen, and residual hydrocarbons can be used as fuel to provide heat for steam reforming process. The sulfur removal step is required to prevent catalyst from sulfur poisoning. Multiple heat exchangers are used to recover the heat from product gases and combustion exhaust for increased overall system efficiency.

A typical steam reformer consists of a catalyst-filled tube where the steam reforming reaction takes place and a furnace that provides the heat required for endothermic reaction. The temperature of the catalyst-filled tube is around 750-850°C depending on steam-to-carbon ratio, space velocity of process gas, and catalyst property. High skin temperature (950-1000°C) of the catalyst-filled tube requires high temperature construction materials for the reactor. To obtain a higher conversion rate, say over 90% for methane steam reforming, a secondary (adiabatic) reformer is often used to promote additional methane conversion. Because the outlet temperatures of product gases may be over 1000°C from the adiabatic reformer, special gas coolers are utilized in most systems. Advantages of two stage reformers over a single primary reformer include the reduced system cost and increased overall conversion efficiency. The major disadvantages of a two-stage reformer system are the need for additional components and the diluting effect of nitrogen if air rather than oxygen is used in the secondary reformer.

Autothermal reformer (ATR) combines partial oxidation (or catalytic partial oxidation) and steam reforming reactions in one reactor. In an ATR reformer, heat generated in partial oxidation reaction (an exothermic reaction) is partially absorbed by steam reforming reaction (an endothermic reaction), which helps to control the temperature of the reactor. The partial oxidation may also help break heavy hydrocarbons down to a methane rich gas for further reforming.

Membrane reactor integrates hydrogen separation component with reformer reactor to provide better conversion of methane. The production rate of a membrane reactor is usually mass transfer limited by the membrane hydrogen permeability. Pd-based membranes are often used for hydrogen separation in the membrane reactor. Methane conversions as high as 96% with Pd membranes in isothermal operation have been reported [27].

7.1.5 Key Technical Challenges

While methane steam reforming is a relatively matured process for hydrogen production, further improvements are required to reduce cost of hydrogen to $2.00–3.00/gge (gallon of gasoline equivalent) and decrease CO_2 emissions from the plant. The key technical challenges include: (1) increase of reforming and separation

efficiencies, (2) CO_2 separation, and (3) capital cost reduction of reformer and balance of plant components.

7.2 WATER ELECTROLYSIS

7.2.1 Thermodynamics of Water Electrolysis Process

Water electrolysis systems (especially alkaline electrolyzer) have been used in varied industries to make hydrogen and oxygen from water for decades. Using alkaline water electrolysis as an example shown in Figure 7-3, the reactions taking place at anode and cathode of the electrolyzer are

Anode (oxygen evolution): $2OH^-_{(aq)} \Rightarrow 0.5O_2 + H_2O + 2e^-$

Cathode (hydrogen evolution): $2H_2O + 2e^- \Rightarrow H_2 + 2OH^-_{(aq)}$

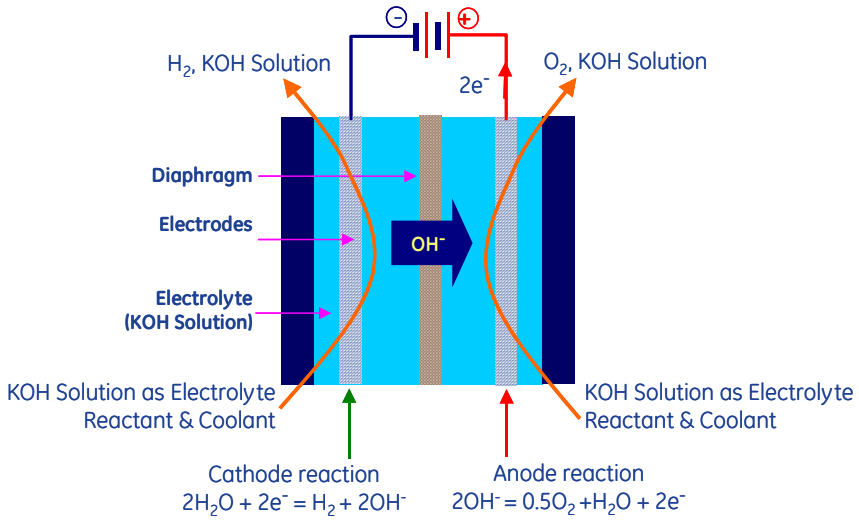

Figure 7-3 Schematic of alkaline water electrolysis

The enthalpy changes of the overall reaction H_2O (l)$\rightarrow$ H_2 (g)+ 0.5 O_2 (g) is 285.84 kJ/mol, which defines the thermoneutral cell voltage E_{TN} as

$$-\frac{\Delta H}{nF} = E_{TN}$$

When the cell voltage, V_{cell}, is less than the thermoneutral cell voltage, external heat must be provided to the electrolysis cell to match the endothermic heat demand; when the cell voltage is higher than the thermoneutral cell voltage, the cell must be cooled to take out the extra heat from the electrochemical reaction. Most electrolyzers operate at voltages above of the thermoneutral voltage and hence require cooling. The minimum cell voltage to initiate the water electrolysis reaction is the reversible voltage defined by

$$E_{rev} = \frac{-\Delta G}{nF}$$

where the F is Faraday constant, n is the number of electrons transferred per reaction, and ΔG is the Gibbs free energy change. At standard conditions (25 °C and 1atm.), the reversible cell voltage E_{rev} = 1.229V and the thermoneutral cell voltage E_{TN} = 1.482V.

7.2.2 Efficiency and Polarization of Electrolysis Cells

The efficiency of an electrolysis process is defined by the energy content of product gas divided by the energy input into the electrolysis system. Assuming the electrolysis cell is operated above thermoneutral cell voltage, efficiency of the electrolysis stack can be described by

$$\eta_{stack.} = \frac{xHHV_{H_2}}{V_{stack} I_{stack}} = \frac{E_{TN}}{V_{cell}}$$

where HHV_{H2} represents the high heating value per mole of hydrogen.

The efficiency calculated above is electrolyzer efficiency only. The efficiency for a real water electrolysis system has to be calculated based on the hydrogen production, energy applied on the electrolyzer, and energy consumed by rest of the system. The overall efficiency of existing alkaline plants is in the range of 80 to 90 % (HHV) [28].

7.2.3 Alkaline Electrolysis System

A simplified flow diagram of an alkaline electrolysis system is shown in Figure 7-4. The main components of an alkaline electrolysis system are:

- Heat exchanges for removal of waste heat from electrolysis stack and heat recovering
- Filters
- Gas separators
- Electrolysis stack
- DC power
- Reservoirs for alkaline electrolyte
- Pumps for circulation of electrolytes
- Water tank

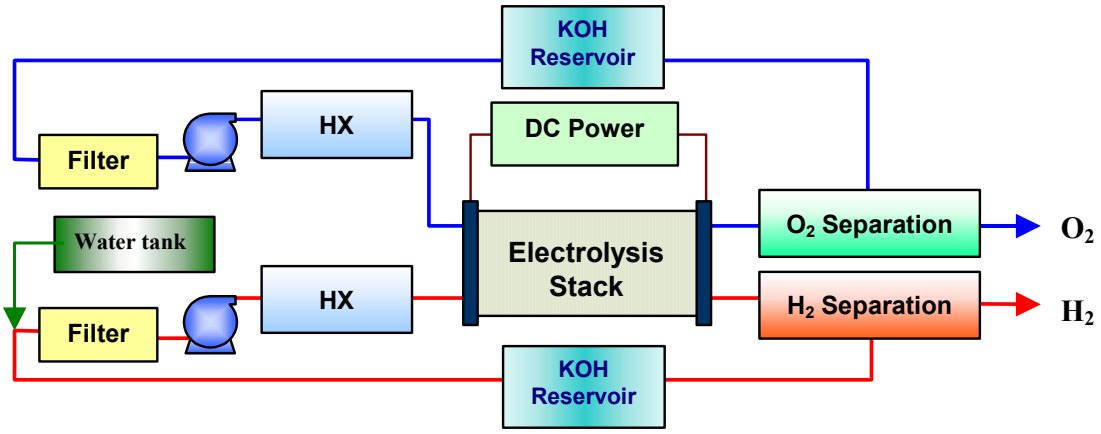

Figure 7-4 A simplified flow diagram of an alkaline electrolysis process

As shown in Figure 7-4, electrolytes (usually 30% of KOH solution) that contain hydrogen from cathode side of the electrolysis cell and oxygen from anode side of the cell exit from the electrolysis stack to two gas separators. Hydrogen and oxygen are discharged from the gas separators via gas control valves and the rest electrolytes return to the electrolysis stack through two filters. Since the operation cell voltage is usually above the thermoneutral cell voltage, extra heat is generated during the operation. Heat exchangers are used to remove the waste heat and sustain the operation temperature. Water is fed into the system to compensate what has been converted to hydrogen and oxygen. To achieve high electrical efficiency of electrolysis, commercial alkaline electrolysis systems are normally operated at 70 to100 °C and 1 to 30 atm.

7.2.3.1 Alkaline Electrolyzer

A typical alkaline electrolyzer consists of electrodes where the anode and cathode reactions take place for water electrolysis, diaphragm for preventing hydrogen and oxygen from mixing, and electrolyte for ion conduction. The electrolyte used in the alkaline electrolyzer also functions as reactant (water) supply to the cathode and cooling media to take out waste heat from electrolysis reaction. Considering the corrosion resistance of construction materials and the requirement of ionic conductivity for electrolyzer, 20-30 wt% of potassium hydroxide (KOH) solutions are traditionally used in alkaline water electrolyzers. The typical operating temperatures and pressures of these electrolyzers are 70-100^{0}C and 1-30 atm, respectively. The main components of an alkaline electrolyzer and their desired properties are listed in Table 7-3.

Table 7-3 Main alkaline electrolyzer components and their desired properties

Components	Desired properties
Anode and cathode materials	• Corrosion resistance • Good conductivity • Good kinetic activity for hydrogen and oxygen evolution reactions • Long term stability
Diaphragm	• Stable in the electrolyte • Good ionic conductivity (or absorb electrolyte to provide ionic conductivity) and electronic resistivity • Physical integrity • Low gas permeability to separate hydrogen and oxygen • Stable in reducing and oxidizing environments
Electrolyte	• Stable at reducing and oxidizing potentials • Good ionic conductivity • Provide sufficient concentration of charge carrying ions

There are two types of design for alkaline water electrolyzers, i.e. monopolar and bipolar (Figure 7-5). In the monopolar design, also called tank design, multiple anodes and cathodes are placed in a tank filled with electrolyte to form a module. The anodes and cathodes of all individual cells are connected in parallel such that the overall module voltage is the same as the single cell voltage. Electrodes are separated from adjacent opposite electrodes by a diaphragm that allows passage of the electrolyte but prevents mixing of product gas. Multiple modules are then connected in series to achieve the desired hydrogen production rate. The monopolar electrolyzer requires a relatively small number of module components and the components are usually inexpensive. One advantage of monopolar design is easy maintenance for the electrolyzer because individual cell can be shut down for repair or replacement simply by short-circuiting two adjacent cells while the rest of the cells are still functional. In the bipolar design, so called filter-press design, a bipolar plate is used, which contains a cathode for one cell and an anode for the adjacent cell. In contrast to the monopolar design, bipolar cells are connected in series each with its own electrolyte. Bipolar design takes up less floor space than monopolar one and is better suited to high-pressure and high-temperature operation. The design compactness provides shorter current paths for the connection between current bus bar and electrodes, which reduces the energy losses due to internal ohmic resistance and therefore increases the electrolyzer efficiency. The advantages and disadvantages of monoplar and bipolar

designs are summarized in Table 7-4 [29]. The monopolar electrolyzers are relatively simple and sturdy in comparison with the bipolar electrolyzers; however, the design trend is toward the bipolar electrolyzer for high electrical efficiency in hydrogen production.

Table 7-4 Comparison of monopolar and bipolar designs for alkaline electrolyzer

	Monopolar Design	**Bipolar Design**
Construction	• Simple, require low degree of precision	• Complex, require high degree of precision of components
Electrolyte	• Share with in cell bank	• Restricted to individual cells
Cell connections	• Parallel	• Series
Operating characteristics	• High current at low voltage • Need external bus bars • Unsuitable for high-temperature operation due to heat losses from large surface area • Requires more floor space • Needs DC power with high current output	• Lower current with high voltage • Simplified power conditioning
Service characteristics	• High reliability • Easy removal of individual cells for repair	• Cells in series make maintenance and repair of individual cells costly

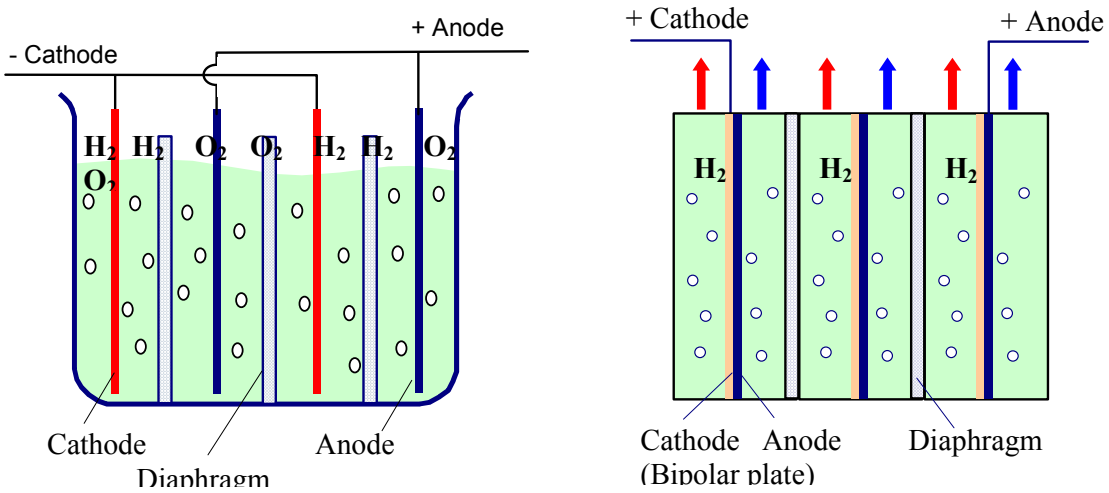

(a) Monopolar (tank-type) design (b) Bipolar (filter-press type) design

Figure 7-5 Schematics of alkaline electrolyzer designs

7.2.3.2 Technical Advancements

The alkaline electrolysis has been in commercial use for decades and works quite reliably for the production of hydrogen and oxygen. To make the alkaline electrolysis an economically competitive process producing hydrogen for energy industry, several areas are required for further improvements, such as electrolyzer design, corrosion resistance and low cost material, and electrocatalyst.

7.2.3.3 Electrolyzer Design

Alkaline electrolyzer design focuses on reduction of capital and operation cost and improvement of hydrogen production efficiency. A new cell configuration, so-called zero-gap cell was developed to reduce the internal resistance and minimize the effects of gas bubbles. In the zero-gap cell design, anode and cathode are pressed on either side of the diaphragm to reduce the internal resistance of the electrolysis cell and force hydrogen and oxygen gases to escape from the electrodes. The design has been widely used by most manufacturers [30]. However there is a limitation for the separation of evolved gas bubbles from liquid electrolyte at normal gravitational force, especially when the electrolysis cell is operated at high current density. To overcome this limitation, centrifugal force was used to promote the separation of gas bubbles from the electrolyte and electrode surface within the electrolysis cell [31]. With the centrifugal force, gas bubbles can effectively be discharged from the electrodes and diaphragm even with very small spacing, thereby virtually eliminating gas blanketing and enhancing the local heat/mass transfer coefficients. The energy required to provide centrifugal force can be compensated by the energy saved from the reduction of cell operation energy. In addition to capital and operation cost reduction, cost reduction for

manufacture and maintenance should also be considered in alkaline water electrolyzer design.

7.2.3.4 Material Development

Most alkaline water electrolysis cells operated at cell voltage of ~1.7-2.1 V with operating current densities of 0.1 to 0.32 A/cm^2 [32]. Increasing operation temperature and pressure can reduce the electrode overpotentials and ohmic resistance. However, the increase of cell operation temperature and pressure is limited by electrolyzer materials due to aging and corrosion of electrodes, cell frame and seal, and crossover of hydrogen and oxygen through the diaphragm.

Traditionally, asbestos with metal (Ni) mesh support was used as diaphragm. However, asbestos is not environmentally friendly. New materials, such as NiO membranes, are used for diaphragm [30]. Plastics, such as modified polyphenylene oxide, polyphenylene ether [32] polyether, polypropylene, epox, and silican rubbers [31] are used to make frame, seal plate, and seal for alkaline electrolyzer. Long-term exposure to corrosive environmental at temperature and pressure can cause aging of these materials and reduce their mechanical strength. Platinum has long been realized as a superior electrocatalyst material for both anode and cathode, but it is too expensive. The commonly used anode is nickel substrate or nickel-plated steel with high surface area catalysts such as nickel oxide and cobalt oxide. The cathodes used for hydrogen evolution also have electrocatalyst, such as high-surface-area nickel alloys, cobalt, sulphided nickel. To further improve the performance stability under intermittent operation condition, electrode that consists of hydrogen storage alloys and nickel-molybdenum coatings was also developed [33].

7.2.4 PEM Electrolysis System

A simplified flow diagram of a PEM electrolysis system is shown in Figure 7-6. Since PEM electrolyte (such as Nafion®, a sulfonated tetrafluorethylene copolymer) is used instead of aqueous electrolyte, there are no needs in the PEM electrolysis system for pump, reservoir, and filter to circulate electrolyte. The system is much simpler than the alkaline electrolysis system. The main components of a PEM electrolysis system are:

- Heat exchanges for the removal of waste heat from electrolysis stack and heat recovering
- Liquid/gas separators
- Electrolysis stack
- DC power
- Proton pump
- Water tank

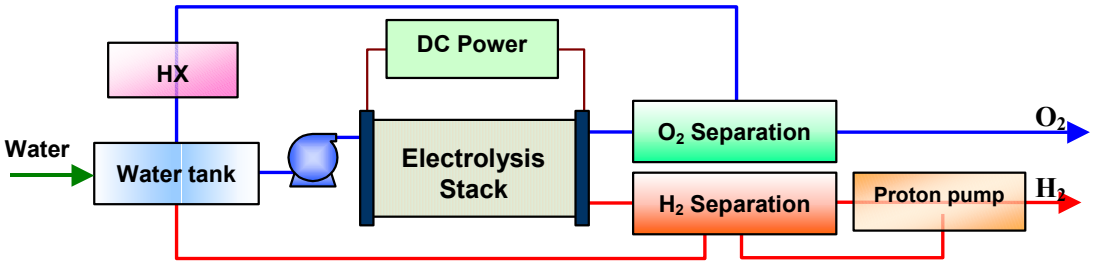

Figure 7-6 A simplified flow diagram of a PEM electrolysis process

Same as the alkaline water electrolyzer, the PEM water electrolyzer consumes electrical energy for the decomposition of water to produce hydrogen and oxygen. However, anode and cathode reactions occurred in a PEM electrolyzer are different from those in alkaline electrolyzer because the conducting ion is proton rather than OH^-. As shown in Figure 7-7, the reactions taking place at anode and cathode of the PEM electrolyzer are:

Anode (oxygen evolution): $H_2O \Rightarrow 2H^+ + 0.5\ O_2 + 2e^-$

Cathode (hydrogen evolution): $2H^+ + 2e^- \Rightarrow H_2$

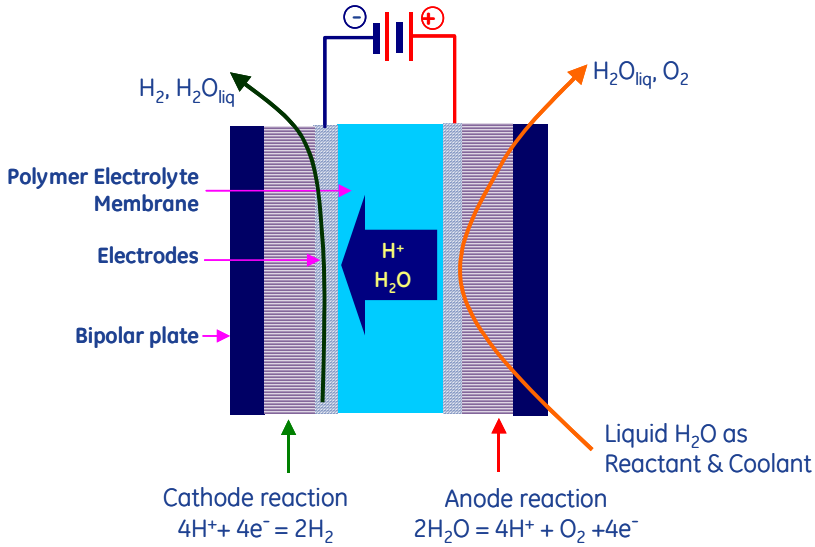

Figure 7-7 Schematic of a PEM water electrolysis cell with liquid-fed anode configuration

The efficiency of the PEM electrolyzer can also be calculated with thermoneutral cell voltage divided by operation voltage of an electrolysis cell. To achieve high electrical efficiency, PEM electrolysis systems are normally operated at temperatures around 80 to 90 °C. PEM electrolyzers are also capable of operating at pressure of 3000 psi or higher [34] with non-aqueous polymer electrolyte. The high-pressure operation makes it possible to electrochemically pressurize the hydrogen product.

The PEM water electrolysis cell shown in Figure 7-7 is configured in the conventional liquid-fed anode configuration. In this configuration liquid water is fed to the anode during electrolysis operation, where oxygen evolution occurs, and protons transport along the electric field gradient to the cathode where hydrogen evolution occurs. Due to the effect of electroosmosis, protons always carry water during their migration (one to four molecules per proton based on hydration condition of Nafion® membrane), which results in liquid water being present at both electrodes, therefore gas/liquid separator is required to dry the hydrogen and oxygen generated from anode and cathode of the PEM electrolyzer (see Figure 7-6). An electrochemical proton pump may also be employed on the cathode loop of PEM electrolyzer to remove all hydrogen from the re-circulation water stream to avoid the hydrogen and oxygen mixing in the water loop. Since the operation cell voltage is usually above the thermoneutral cell voltage, extra heat is generated during the operation. Heat exchangers are used to remove the waste heat and sustain the operation temperature.

7.2.4.1 PEM Electrolyzer

As shown in Figure 7-7, a typical PEM electrolyzer consists of electrodes where the anode and cathode reactions take place for the decomposition of water, proton exchange membrane that functions as electrolyte for proton conduction as well as preventing the mix of hydrogen and oxygen produced at anode and cathode. Water also working as cooling media is supplied to the anode as reactant in the conventional liquid-fed anode configuration. Due to the effect of electroosmosis and concentration gradient, liquid water always presents at both electrodes. The benefit of the full hydration is the relaxation to Nafion® membrane degradation, which will significantly improve the reliability of PEM water electrolyzer though gas/liquid separator is required to dry the hydrogen.

Based on the requirements of application and system design, two alternative water-fed configurations, i.e. liquid-fed cathode configuration and vapor-fed anode configuration, are also developed. As shown in Figure 7-8, liquid water is fed to the cathode, and diffuses through the membrane to the anode where oxygen evolution occurs, and protons transport from the anode to the cathode along the electric field gradient. Since the only source of water at the anode is from cathode via diffusion, and that diffusion is constantly being countered by the electroosmotic drag of the proton flux, the anode is usually operated under less than saturated conditions. This results in the production of an oxygen stream that, while not completely dry, contains only vapor phase water and eliminates the need for a phase separator.

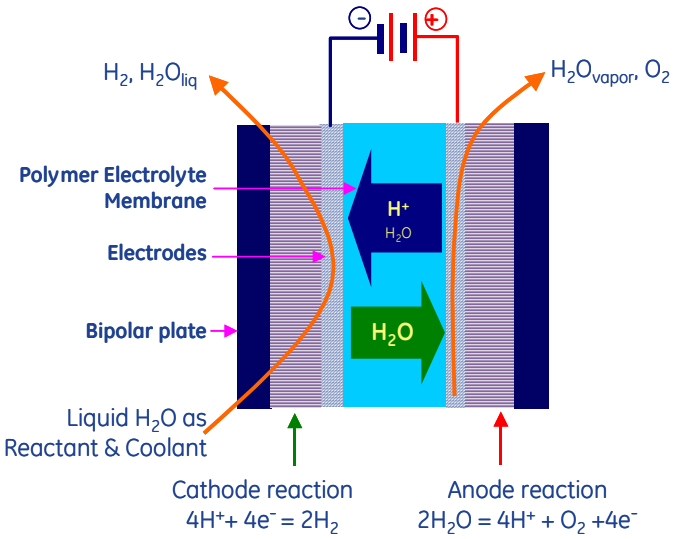

Figure 7-8 Schematic of a PEM water electrolysis cell with liquid-fed cathode configuration

For vapor-fed anode configuration (Figure 7-9), water vapor is fed to the anode, where oxygen evolution occurs, and protons transport along the electric field gradient to the cathode where hydrogen evolution occurs. The membrane electrolyte is in relatively dry condition, which reduces the effect of electroosmosis. Less water molecules are carried by the migration of proton. No liquid water exists in anode and cathode, eliminating the need for phase separators. However, this configuration may lower the reliability of PEM water electrolyzer since dehydration will promote the degradation of Nafion® membrane.

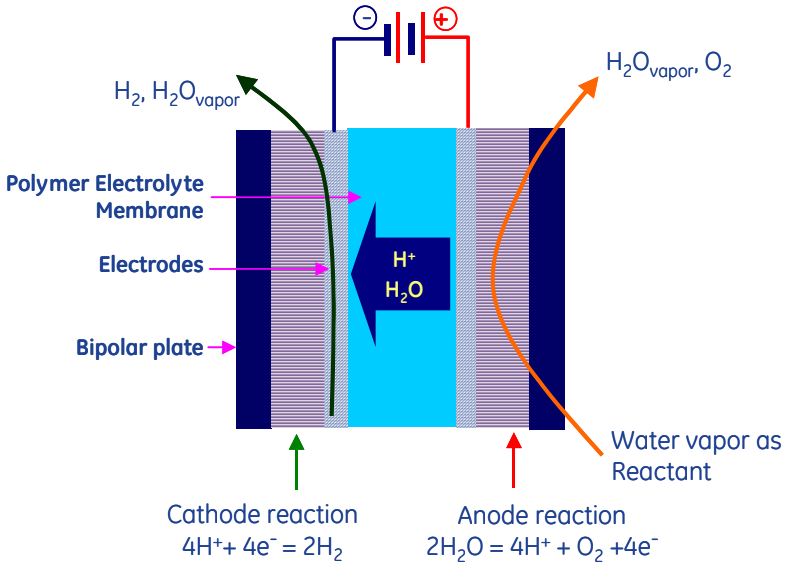

Figure 7-9 Schematic of a PEM water electrolysis cell with vapor-fed anode configuration

Due to the acidic nature of proton exchange membrane and the elevated operation temperature and pressure (80 to 90 °C with pressure up to 3000 psi or higher), corrosion resistant materials that have sufficient mechanical property and chemical stability are required for the construction of PEM water electrolyzer. The main components of the PEM water electrolyzer and their desired properties are listed in Table 7-5.

Table 7-5 Main PEM electrolyzer components and their desired properties

Components	Desired properties
MEAs (membrane and electrodes assembly) Such as Nafion® membrane, Pt/C for cathode, and Pt/C, Ir, and RuO_2-IrO_2-SnO_2 for anode catalysts	• Good kinetic activity for hydrogen and oxygen evolution reactions • Stable at reducing and oxidizing potentials • Good ionic and electrical conductivity for electrodes • Good ionic conductivity for membrane electrolyte • Electronic isolator for membrane electrolyte • Sufficient mechanical strength • Low gas permeability to prevent gas crossover • Long term stability
GDLs (gas diffusion layers) Such as carbon paper, carbon cloth	• Stable at reducing and oxidizing potentials • Good electrical conductivity • Good gas and liquid water permeability • Sufficient mechanical strength • Long term stability
Bipolar plates Such as graphite, carbon composite, SS steal	• Stable in the acidic reducing and oxidizing environment, • Good electrical conductivity • Sufficient mechanical strength • Low gas permeability for gas crossover
Seals Such as silicon rubber, Teflon	• Stable at reducing and oxidizing potentials • Electrical isolator (depends on design of electrolyzer) • Sufficient mechanical strength • Low gas permeability to prevent gas leakage • Long term stability

7.2.4.2 Technical Advancements

PEM water electrolysis is historically related to the invention of proton exchange membrane Nafion®. GE created the first PEM electrolyzer as regenerative fuel cell for the NASA space program [35]. Since then advanced PEM electrolyzers have been

developed and manufactured. A 95.1% of hydrogen production efficiency was achieved for an electrolysis cell with 2500 cm^2 active area operated at 1.556V and 1 A/cm^2 current density at 80°C [36]. PEM electrolyzers have been used reliably to generate high-purity hydrogen and oxygen for special applications, such as power plant cooling, material processing, and semiconductor manufacturing. The capital cost of PEM water electrolysis, however, is still too high for producing hydrogen as energy carrier. It is necessary to reduce the capital cost and improve the performance of PEM electrolyzer through innovated electrolyzer and system designs as well as low-cost materials.

7.2.4.3 Electrolyzer Design

As shown in Figure 7-10, the performance entitlement of PEM electrolysis cell is very impressive [37]. PEM electrolyzer is also capable of operating at high pressure, offering potentials to reduce operation cost for hydrogen production. In addition to reducing impact of product gases on mass transfer in liquid fed configuration and improving thermal management at high current densities, the electrolyzer design are focused on (1) increasing operation pressure to eliminate the need for hydrogen compressor and (2) replacing expensive materials and simplifying component design.

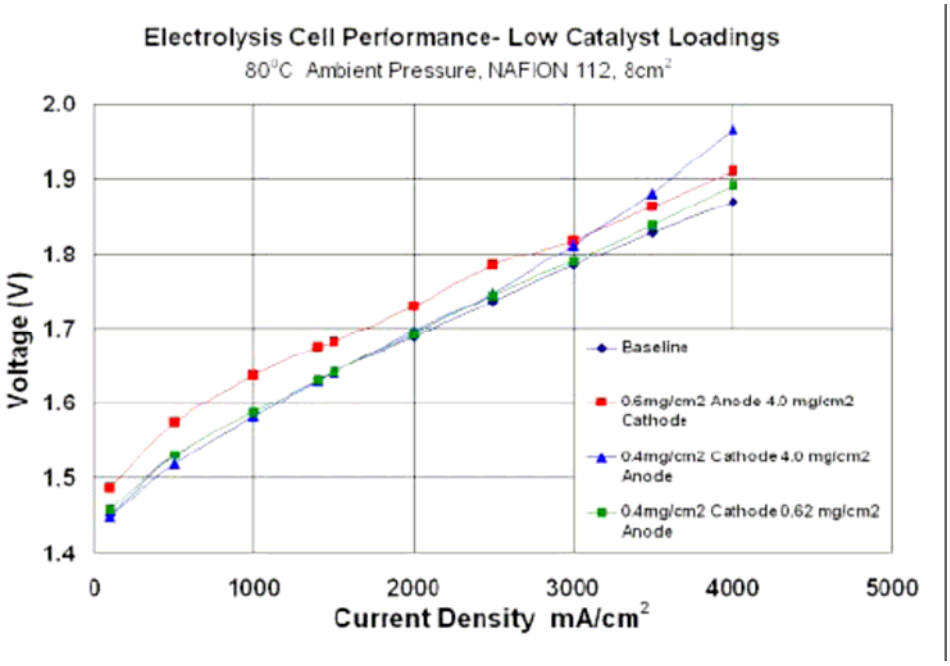

Figure 7-10 Performance of a single PEM electrolysis cell

For PEM electrolyzer operated at high pressure, thick membrane electrolyte is required to increase mechanical strength for high differential pressure across the membrane and reduce product gas crossover through the membrane. However, the thick membrane will cause the increase of ohmic overpotential. In addition, the high strength construction materials for electrolysis stack are also required for the high-pressure operation. Therefore a capital and operation cost trade-off should be

performed between a PEM electrolysis stack with thick membrane and strong construction material for high-pressure operation and an electrolysis stack with thin membrane and regular construction materials for nominal pressure operation.

Another approach to reduce capital cost is to simplify the design of PEM electrolysis stack by reducing component count and manufacture process cost. Simple design and less part count will also benefit the reliability and life of the electrolysis stack.

7.2.4.4 Material Development

PEM water electrolysis stacks have been tested over 30,000-hour at high pressures with very low cell voltage degradation rate (approximately. 0.026V/year). However, the cost of current materials used in the PEM electrolysis stack, such as expensive proton exchange membrane, precious metal catalysts, and construction materials, limits the mass production and further performance improvements at high operation temperature and pressure.

Proton exchange membrane functions as electrolyte in the PEM electrolyzer and it also keeps the hydrogen and oxygen apart. The crossover of product gas can result in coulombic efficiency reduction. For example, the equivalent current lost of the crossover is about 0.08 A/cm² for Nafion 117 membrane at 90°C and 1000 psia hydrogen differential pressure. To improve the efficiency, safety, and reduce the cost of PEM electrolyzer, it is necessary to explore and develop advanced proton exchange membrane. Another approach to reduce the gas crossover is to control the operating condition and membrane hydration since the gas permeability decreases with decrease of temperature and increase of water content in the membrane.

Plastics, such as polycarbonate, polypropylene, silicone rubbers, expanded PTFE (polytetrafluoroethylene) and metal alloy (stainless steel, titanium) sheets are used to make frame, seal plate, bipolar plates, and seal for PEM electrolyzer. Long-term exposure to hydrogen/oxygen environmental at temperature and pressure can cause aging and hydrogen embitterment to these construction materials. Advancements are needed in improving the base materials properties and developing protective coatings.

As part of the cost reduction effort, the developments of electrode for PEM electrolyzer focus on the reduction of catalyst loading and the replacement of precious metal catalyst. The performance of an MEA with 1mg/cm^2 precious metal catalyst loading has been demonstrated to be comparable to that of a baseline MEA with 8mg/cm^2 precious metal catalyst loading (4 mg/cm^2 Pt on cathode, 4 mg/cm Pt plus Ir on the anode) at current densities up to 4,000 mA/cm^2 [37]. The activity of anode catalyst with 30 to 50% of RuO_2 is comparable to the activity of pure IrO_2. Development on high performance and low cost electrocatalysts will directly lower the capital cost and reduce the activation overpotential, thus the operation cost of the PEM electrolysis.

7.2.5 SOFC Electrolysis System

SOFC steam electrolysis uses the same electrochemical principles as other water electrolysis technology. High temperature steam electrolysis, however, has the potentials for high efficiency because

- the total energy demand for water splitting is lower in the vapor phase than in the liquid phase and the energy for vaporization can be provided thermally rather than electrically,
- the minimum demand for electrical energy needed for electrolysis decreases with increasing temperature, i.e. one has the possibility of providing part of the splitting energy by thermal energy instead of electrical thus achieving higher total efficiency; and
- the improved reaction kinetics at elevated temperatures lower overpotentials.

The efficiency benefit can be graphically illustrated with Figure 7-11. As can be seen from the figure, the total energy required for steam electrolysis slightly increase with temperature, but the electrical energy required decreases with temperature while the heat demand increases. The efficiency benefit can be better described with the thermodynamic efficiency defined with equation [38]:

$$\eta_{ther} = \frac{\Delta H_{H2(HHV)}}{E_{electrolyzer} / \eta_{electrical} + Q + S_{steam} / \eta_{steam}}$$

where $\Delta H_{H2(HHV)}$ is the high heating value of the hydrogen generated, $E_{electrolyzer}$ is the electrical energy required, $\eta_{electrical}$ is the thermodynamic efficiency of electrical power generation, S_{steam} is heat needed to generate the steam at a thermodynamic efficiency of η_{steam}, and Q is the heat demand excluding steam generation. For a simplified case where the η_{steam} is assumed as 100% and the Q is replaced with $T\Delta S$, the thermodynamic efficiency of electrolysis as a function of the electrical power generation efficiency $\eta_{electrical}$ can be presented in Figure 7-12. The typical electrical power generation efficiency $\eta_{electrical}$ is in the range of 30-50% depending on technologies. As can be seen, steam electrolysis has better thermodynamic efficiency than the liquid water electrolysis unless the electrical power generation efficiency is extremely high where the difference is not evident.

Comparing to other water electrolysis systems (PEM and Alkaline), the SOEC electrolysis system development is less mature. The progress has been limited to lab-scale prototypes. The key system components include solid oxide electrolyzer, heat exchanger, recycle blower, and steam generation and feed sub-system. Similar as other electrolysis system, the solid oxide electrolysis system can be integrated with renewable energy sources, such as wind and solar. The system also offers additional

potentials to integrate with sources where high temperature steam is available at low cost, such as nuclear, geothermal, and fossil energy plants.

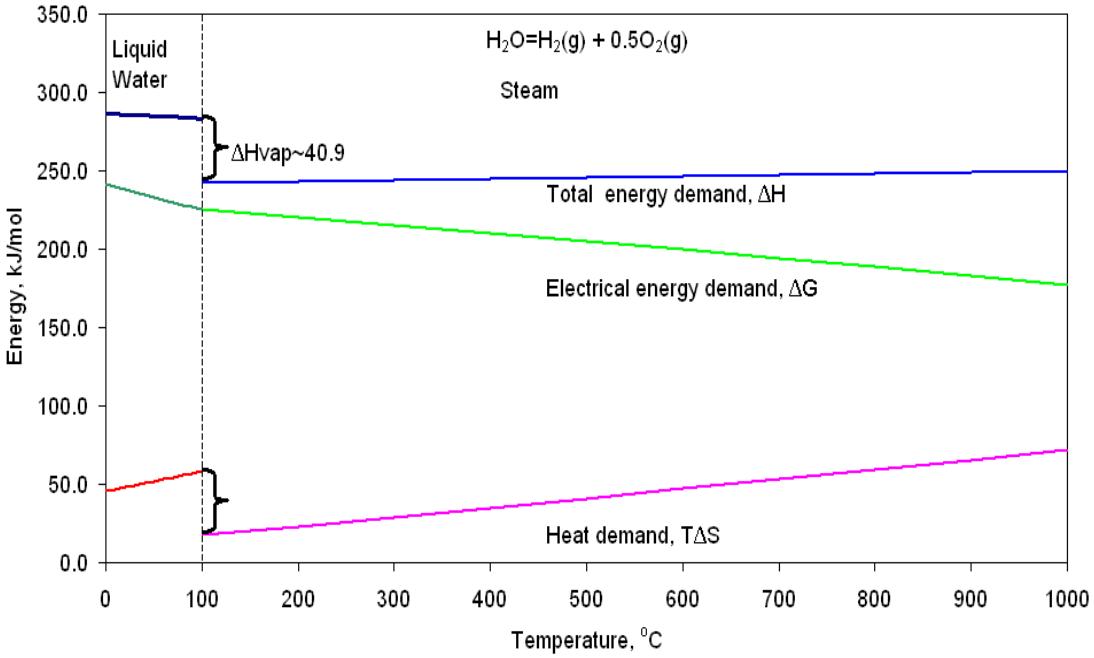

Figure 7-11 Energy required to split water to form one-mole hydrogen at different temperature.

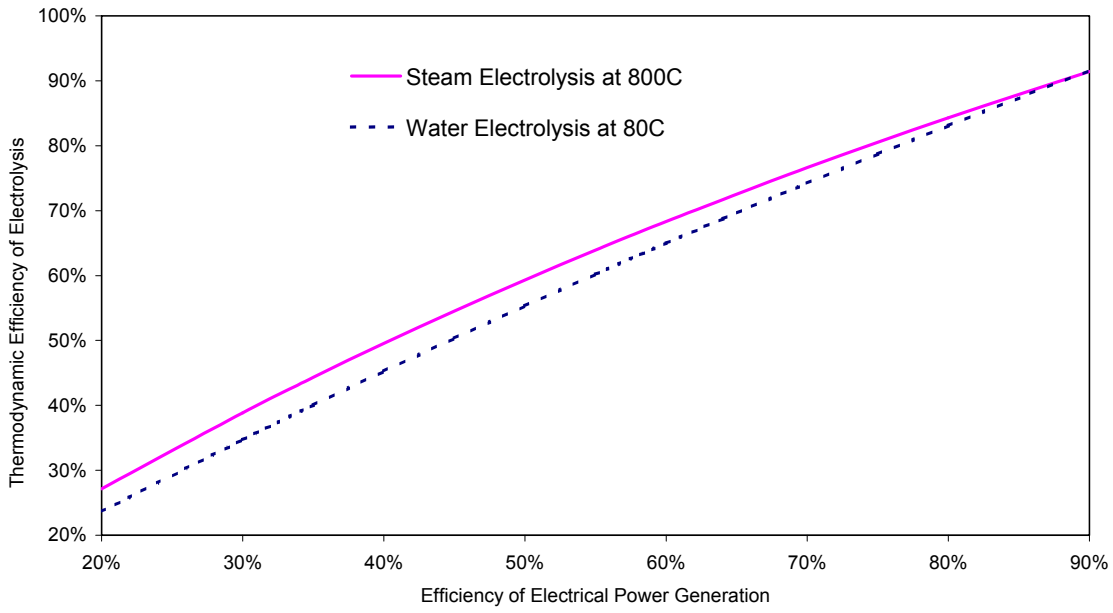

Figure 7-12 Thermodynamic efficiency of electrolysis

7.2.5.1 Solid Oxide Electrolyzer

The general electrochemical principle for high temperature steam electrolysis is schematically illustrated in Figure 2-1a using an oxygen ion-conducting electrolyte as an example. The same principle can be used for CO_2 reduction to generate O_2 and CO. The electrolyzer can easily adapt the existing SOFC stack design, such as planar and tubular design.

The key challenges in the development of solid oxide electrolyzer relate to stack materials (electrode and interconnect) for performance and stability, electrolyzer design and components fabrication for cost reduction, reliable seals for efficient hydrogen collection, system design for heat integration, and enabling technologies such as high temperature recycle blower and high temperature heat exchangers.

7.2.5.2 Technical Advancement

There had been some studies on the high-temperature steam electrolysis in 80's [38-42], including system analysis and cell and stack development. To reduce the capital cost and increase electrical efficiency thus reduce the operation cost, specific hydrogen generation ability and cell performance have to be improved simultaneously because of the direct correlations between specific hydrogen generation and electrical energy demand (Figure 7-13).

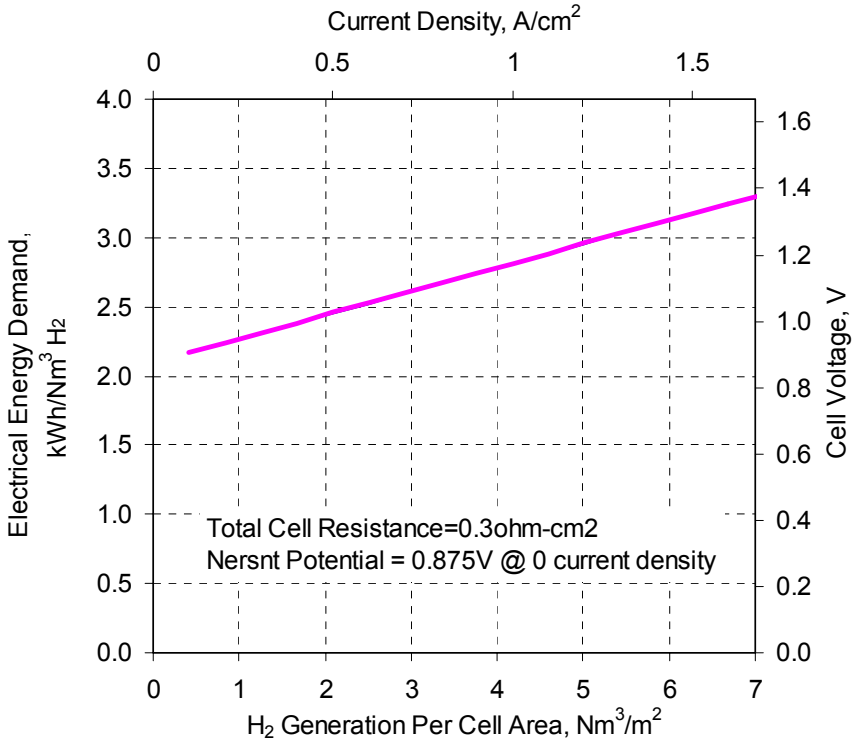

Figure 7-13 Correlations between specific hydrogen generation and electrical energy demand

A recent advancement is natural gas-assisted steam electolyzer, where a reducing gas is introduced into the anode side to consume the oxygen generated and to lower the high Nernst potential to overcome [43]. More recently, a composite/hybrid SOFC/SOEC stack has been proposed for electricity and hydrogen co-gen from natural gas [44]. Such operation modes offer potentials for high electrolyzer efficiency but one challenge is to develop an active and stable anode material.

Another advancement is to use the planar cell design to improve the performance and specific hydrogen generation capability [45, 46]. With self-supported YSZ as the electrolyte at 800°C, about 2.67 SLPM hydrogen was generated with 25-cell stack (64 cm^2 active area per cell) at stack voltage of ~33V [46]. This suggested a specific hydrogen generation capability of 1.17 Nm^3/m^2 with DC electrical power consumption of 3.16 kWh/Nm^3.

To further reduce the ohmic losses of the cells, it is desired to use electrode-supported cells with thin electrolyte. For instance, at cell voltage of 1.48V, a current density of 3.6A/cm^2 was obtained in a button cell at 950°C in the absence of stainless steel interconnect materials [47]. Under the current program, 10-cell with footprint of 16-cm in diameter have been tested at 800°C with the hydrogen generation capability of 2.59 Nm^3/m^2 and the energy demand of 3 kWh/Nm^3.

7.2.5.3 Electrolyzer Design

Electrolyzer design can be generally categorized as planer and tubular design based on the cell topology. The existing SOFC stack design can be easily adapted in solid oxide electrolyzer design. At present, four common SOFC stack design configurations have been proposed and fabricated: sealess tubular design, segmented-cell-in-series design, monolithic design, and flat plate design. Each of these designs distinguishes itself from the others in characteristics of geometry, structural support, sealing methods, and cell-to-cell electrical connections. Depending on the stack design topology, the cell structures can be generally categorized as planar and tubular. Independent of the cell topology, the cell structures can also be classified as electrolyte-supported cells, electrode-supported cells (cathode- and/or anode-supported), and interconnect/flow field-supported cells (interconnect-supported or porous substrates-supported).

Cell configurations can vary depending on the stack design and manufacturing processes. The cell configuration selection depends on the stack/system design requirements as well as the fabrication and technology capability. At present, most efforts have been focused on the electrode-supported thin electrolyte configuration, while the porous metal-supported cell configuration with deposition technology is in the exploration stage.

7.2.5.4 Materials Development

Key materials in the SOEC stack is the cell materials, interconnect materials, and seals. The options of the electrode and electrolyte materials have been discussed in the materials assessment section. One of the key challenges is to develop oxygen electrode to improve the performance and stability. In addition to the cells materials,

issues associated with interconnect and seal materials have to be addressed for efficiency and reliability.

Interconnect materials include ceramic interconnect, such as doped lanthanum chromite, and metallic ones, such as Crofer22APU, E-Brite, Hitachi ZMG232, and ODS chromium alloys $Cr5Fe1Y_2O_3$. Similar to SOFC, the electrolysis cells are susceptible to degradation associated with the usage of stainless steel interconnect. The degradation associated with the Fe-Cr ferritic alloys includes the oxide scale growth on the metal surface and chromium poisoning of the oxygen electrode. The oxide scale formation mechanism is relatively well understood. In Fe-Cr alloys, the oxide scale formation is most likely dependent on the Cr outward diffusion to the surface to form oxide scale. The Cr poisoning mechanism is lack of clear understanding. The general hypothesis is that the Cr_2O_3 oxide reacts with oxygen and moisture to form volatile species such as CrO_3 and $CrO_2(OH)_2$. These species can react with the oxygen electrode to form resistive materials such as $SrCrO_4$, and/or deposit Cr_2O_3 species at the cathode/electrolyte interfaces leading to reduction of electrode activities. To reduce performance degradation rate, most of the efforts have been focused on metal surface composition modification to form a more conductive and less volatile oxide scale and development of protective coatings.

Table 7-6- Comparison of seal options

Option	Pros	Cons
Compressive Seal	• Tolerance for CTE mismatch • Long-term stability • Potential for disassembly, repair • Easy manufacturing	• Leaking seal • High pressure or load required • Surface preparation and finish • Limitation on location for usage • Potential to creep at high load
Glass-Ceramic Seal	• Leak tight or hermetic • Good bonding and wetting to both ceramic and metal • Tailored CTE to match mating parts • Stress release at high T	• Reactive with fuel cell parts over long-term • Brittle in nature, especially at low temperature • Weaker with thermal cycling • Structure, phase change over time

Seal is another critical element in the solid oxide electrolyzer. The basic requirements for a SOEC seal in a stack are:

- Gas-tightness or allowable/controllable leakage rate under steady-state and thermal transits
- Compatibility with stack design, assembly, operation, and service processes

- Chemical stability under processing and operating conditions (gas, temperature, pressure, and voltage)
- Compatibility with materials and components in contact
- High electrical resistance under cell potential

Currently, two major approaches are used in SOFC sealing practice, glass-ceramic based chemical seal and gasket based mechanical (compressive) seal. A brief comparison of pros and cons of these two groups of seals are listed in the Table 7-6.

7.3 TECHNOLOGY COMPARISON SUMMARY

Like RSOFC, alkaline and PEM electrolyzers can also be operated under dual mode: power generation mode and electrolysis mode. Steam reforming, however, is a chemical process to produce hydrogen and doesn't have the flexibility to covert the chemical energy into electricity. A status and potential of varied hydrogen production technologies has been summarized in Table 7-7.

Table 7-7 Summary of status and potential of hydrogen production technologies

	SOEC steam electrolysis	**Alkaline water electrolysis**	**PEM water electrolysis**	**Steam reforming**
Feedstock	• Electricity Grid Renewable: Wind, Solar • Water	• Electricity Grid Renewable: Wind, Solar • Water	• Electricity Grid Renewable: Wind, Solar • Water	• Methane • Biogas • Liquid fuel
Technology Readiness	• R&D Bench scale • Operated at high current density, small package size • Potential for high system efficiency	• H_2 production rate up to 27 kg /hr at 360 psi • Operated at low current density, large package size • Commercial system efficiency ~ 65 –73%	• H_2 production up to 4.5 kg /hr at 200 psi • Operated at high current density, small package size • Commercial system efficiency ~ 60%	• H_2 production rate up to 9000 kg/hr • Difficult for scale down in size • Commercial system efficiency ~70~80%
Applications	• Distributed fueling station • Oxygen generation • Regenerative power plant (Back-up power, residential)	• Centralized and distributed fueling station • Oxygen generation • Industry use of high purity H_2 • Regenerative power plant possible	• Distributed fueling station • Oxygen generation • Industry use of high purity H_2 • Regenerative power plant (Back-up power, residential…) • Aerospace industry	• Food and chemical industry • Centralized fueling station
Purity of Hydrogen	• High purity of H_2 • Easy H_2 separation from H_2O	• High purity of H_2 • Easy H_2 separation from KOH electrolyte	• High purity of H_2 • Easy H_2 separation from H_2O	• Need additional separation process (PSA or membrane) for the separation of CO, CO_2, H_2O,

				and CH_4
Hydrogen Pressure for Storage	• Need H_2 compressor • Low risk of O_2 and H_2 crossover	• Up to 440 psi balanced pressure demonstrated • Low ΔP tolerance • Need H_2 compressor • Risk of O_2 and H_2 crossover	• Up to 3000 psi ΔP or balanced pressure demonstrated • Potential to 6000 psi • May need H_2 compressor to push pressure up to 10000 psi • Low risk of O_2 and H_2 crossover	• Need H_2 compressor
Efficiency Entitlement	• Potential for high efficiency by using waste heat or free heat to generate steam • Depend on operation conditions (H_2 production/cm^2) • Stack efficiency = E_{TN}/V_{cell}	• Depend on operation conditions (H_2 production/cm^2) • Stack efficiency = E_{TN}/V_{cell}	• Depend on operation conditions (H_2 production/cm^2) • Stack efficiency = E_{TN}/V_{cell}	• 120.6% with free heat • ~90% (heat supplied externally for the steam reforming process and vaporization of water)
System Reliability	• High temperature system design and auxiliary components may reduce reliability • No data yet	• Simple system design, need reliable pressure control system • Proven for high reliability for life support in submarines • Proven commercial designs • •KOH may cause piping system corrosion	• Simplest system design • Proven for high reliability for life support in submarines • Commercial system available	• Mature technology (some plants operated over 40 – 60 years) • Complicated system design and auxiliary components may reduce reliability
EHS, Emissions, and CO_2 Sequestration	• Chemicals: O_2, H_2 • High operation temperature	• Chemicals: O_2, H_2 and KOH or NaOH • Corrosive electrolyte at operation temperature	• Chemicals: O_2, H_2	• Chemicals: H_2, CO, CO_2, CH_4, possible NO_X from burner, and waste chemicals from desulfur • High operation temperature • Require CO_2 sequestration
Hurdles for Producing H_2 as Energy Carrier	• Cost of electricity • System and electrolyzer cost • Challenges for large scale H_2 production	• Cost of electricity • System and electrolyzer cost	• Cost of electricity • System and electrolyzer cost • Challenges for large scale H_2 production	• Low flexibility for different H_2 production rate • CO_2 emissions • Still use fossil fuel • Capital cost
Development Focuses	• Electrode and stack design to increase efficiency and reduce materials cost • Reliable seal for	• New catalyst and design innovation to increase efficiency and use low cost materials • Optimize pressure control system for	• New catalyst and design innovation to increase efficiency (high pressure operation) • Design for cost	• New catalyst and design innovation to increase efficiency and reduce materials cost

	H_2 production • Interconnect for reliability • Design for cost and manufacturing	high pressure operation • Design for cost and manufacturing	and manufacturing • Use low cost materials	• Optimize system design • H_2 separation and CO_2 sequestration technologies
Flexibility	• Has the capability to operate under power generation mode with a variety of fuels	• Has the capability to operate under power generation mode with hydrogen fuel	• Has the capability to operate under power generation mode with hydrogen fuel	• Not capable to convert fuels to electricity

7.4 TECHNOLOGY ROADMAP

Comparing to other electrolysis technology, the solid oxide steam electrolysis is less mature. Significant development effort is needed to fully realize its potentials in efficiency and cost. This includes the critical element development and system demo. A simplified technology road map is presented in Figure 7-14.

Technology feasibility of RSOFC has been demonstrated through the program. The next critical developments are for the key stack elements: cells, seals and interconnects to prepare for a technology demo through a small system for system efficiency and dual mode operation. In parallel, reliability related to seals and interconnects are to be significantly advanced. With the lessons learned from the system demo and reliability improvement, stack scale up is needed and this includes the large footprint cell fabrication and large stack design. Once the stack scale-up is completed, most of the technology risks will be retired. Additional stack risks are associated with pressurization, which might be optional depending on the system designs and applications. The rest of the technology milestones are system and cost related. In the system optimization, specific application must be identified and system design must be detailed for such specific application. Key system elements such as high temperature heat exchangers and high temperature recycle blowers must be developed for determined system efficiency and reliability. The cost reduction is to mature the manufacturing process, implement low cost materials, and simplify balance of plant components without compromise of system performance. The last technology milestones will a proof of concept demonstration for efficiency and reliability at system level and pressurization operation if it is preferred.

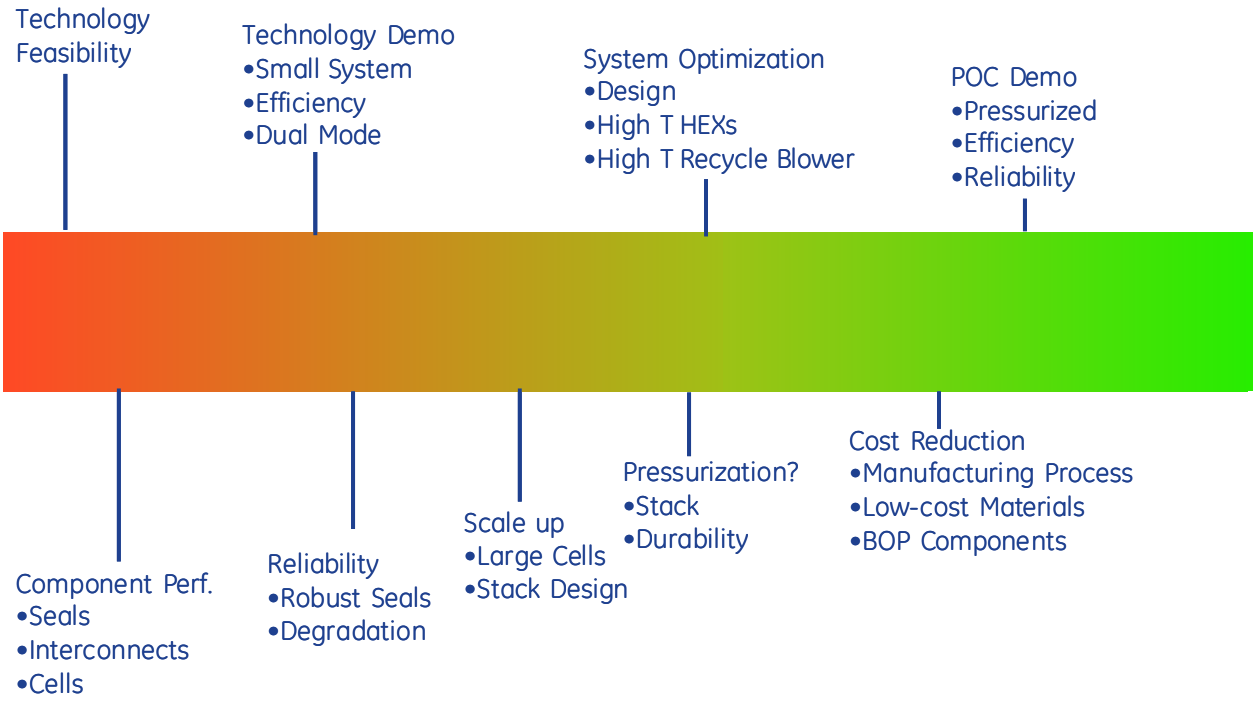

Figure 7-14 Technology roadmap for reversible solid oxide fuel cell systems

8 CONCLUSIONS

In conclusion, the "High Performance Flexible Reversible Solid Oxide Fuel Cell" program was very successful. This project has developed a set of materials and optimized electrode microstructures for reversible solid oxide fuel cells; and demonstrated the feasibility and operation of a reversible SOFC multi-cell stack. A 10-cell reversible SOFC stack was operated over 1000 hours alternating between fuel cell and steam electrolysis modes. The stack ran very successfully with high power density of 480 mW/cm^2 at 0.7V and 80% fuel utilization in fuel cell mode and >6 SLPM hydrogen production in steam electrolysis mode using about 1.1 kW electrical power. The hydrogen generation is equivalent to a specific capability of 2.59 Nm^3/m^2 with electrical energy demand of 3 kWh/Nm^3. The performance stability in electrolysis mode was improved vastly during the program with a degradation rate reduction from 8000 to 200 mohm-cm^2/1000 hrs. Both cost estimate and technology assessment were conducted. Besides the flexibility running under both fuel cell mode and electrolysis mode, the reversible SOFC system has the potentials for low cost and high efficient hydrogen production through steam electrolysis. The cost for hydrogen production at large scale was estimated at ~\$2.7/kgH_2, comparing favorably with other electrolysis technology. The advancements under this program have formed a basis for future work to move the technology toward practical applications.

9 REFERENCES

1 N.Q. Minh and T. Takahashi, Science and Technology of Ceramic Fuel Cells, Elsevier, Amsterdam, 1995.

2 N.Q. Minh, J. Am. Ceram. Soc., **76** (1993) 563

3 S.C. Singhal and K. Kendall (eds.), High Temperature Solid Oxide Fuel Cells: Fundamentals, Design, and Applications, Elsevier, Oxford, UK, 2003.

4 R. Steves, "An Introduction to Zirconia", Magnesium Elektron, London, UK, 1986.

5 A. Bieberle, L.J. Gauckler, in "Oxygen Ion and Mixed Conductors and Their Technological Applications", Edited by H. Tuller, J. Schoonman, and I. Riess, Kluwer Academic Publishers, Dordrecht, 2000.

6 T. Ishigaki, S. Yamauchi, K. Kishio, J. Mizusaki and K. Fueki, J. Solid State Chem. **73**, (1988).

7 X.J. Chen, K.A. Khor and S.H. Chan, J. Power Sources, **123** (2003) 17.

8 E.T. Elshof, in Dense Inorganic Membranes, Ph.D. Thesis, University of Twente, Netherlands (1998).

9 A.M. Svensson, S. Sunde and K. Nisancioglu, J. Electrochem. Soc. **145**, (1998) 1390.

10 J. Xu and G.F. Froment, AIChE Journal 35, (1989) 88.

11 R. Jackson, in Transport in Porous Catalysts, Elsevier Scientific, New York (1977).

12 Winkler, P.V. Hendriksen, N. Bonanos, and M. Mogensen, J. Electrochem. Soc., **145** (1998) 1184.

13 S. B. Adler, J. Elecrochem. Soc., **149** (2002) E166.

14 T. Kato, A. Momma, Y. Kaga,S. Nagata, Y. Kasuga, and M. Kitase, "Influence of Cell Configuration on Measuring Interfacial Impedances between a Solid Electrolyte and an Electrode", Solid State Ionics, **132** (2000) 287.

15 H. Yokokawa, in Solid-State Ionic Devices III, E. Wachman, K. Swider-Lyons, M. F. Carolan, F.H. Garzon, M. Liu, and J. R. Stetter, Editors, PV 2002-26, p.1, The Electrochemical Society Proceedings Series, Pennington, NJ (2002).

16 Taniguchi, M. Kadowaki, H. Kawamura, T. Yasuo, Y. Akiyama, Y. Miyake, and T. Saitoh, J. Power Sources, **55** (1995) 73.

17 S. Badwal, R. Deller, K. Foger, Y. Ramprakash, and J. Zhang, Solid State Ionics, **99** (1997) 297.

18 K. Hilpert, D. Das, M. Miller, D. Peck, and R. Weiss, J. Electrochem. Soc., **143** (1996) 3642.

19 S.P. Jiang, J. Zhang, K. Foger, J. Electrochem. Soc., **147** (2000) 3195.

20 E. Konysheva, H. Penkalla, E. Wessel, J. Mertens, U. Seeling, L. Singheiser, and K. Hilpert, J. Electrochem. Soc., **153** (2006) A765.

21 S. Simner, M. Anderson, G. Xia, Z. Yang, L. Pederson, and J. Stevenson, J. Electrochem.Soc., **152** (2005) A740.

22 J. Kondoh, T. Kawashima, S. Kikuchi, Y. Tomii, Y. Ito, J. Electrochem. Soc. **145** (1998) 1527.

23 B. C. R. Ewan and R. W. K. Allen, International Journal of Hydrogen Energy, **30** (2005) 809.

24 S. Dunn, International Journal of Hydrogen Energy, **27** (2002) 235.

25 J. Ohi, Journal of Materials Research, **20** (2005) 3180.

26 Andrew E. Lutz, Robert W. Bradshaw, Jay O. Keller, and Dennis E. Witmer, International Journal of Hydrogen Energy, **28** (2003) 159.

27 Fabiano A.N. Femandes, Aldo B. Soares Jr, Fuel, **85** (2006) 56.

28 Peter Hoffmann, Tomorrow's energy: hydrogen, fuel cells, and the prospects for a cleaner planet, MIT Press, 2001, p61.

29 Michael C. Stemp, Thesis for Master's degree in Applied Science and Engineering, University of Toronto, 1997.

30 Oystein Ulleberg, International Journal of Hydrogen Energy, **28** (2003) 21.

31 H. Cheng, K. Scott, and C. Ramshaw, Journal of The Electrochemical Society, **149** (2002) D172.

32 R. Bourgeois, Presentation at DOE Hydrogen Program Annual Review Meeting, Project # PD8, Crystal City, VA, 5/17/2006.

33 W. Hu, International Journal of Hydrogen Energy, **25** (2000) 111.

34 C. Cropley, Presentation at DOE Hydrogen Program Annual Review Meeting, Project # PDP2, Crystal City, VA, 5/16/2006.

35 Fuel Cell Systems, edited by Leo J. M. J. Blomen and Michael N. Mugerwa, Plenum Press, New York and London, 1993.

36 S. A. Grigoriev, V. I. Porembsky, and V. N. Fateev, International Journal of Hydrogen Energy, **31** (2000) 171.

37 C. Cropley and T. Norman, DOE Hydrogen Program, FY 2004 Progress Report, II.F.5 Giner Electrochemical Systems, LLC, 2004.

38 M.A. Liefa and A. Borhan, International Journal of Hydrogen Energy, **11** (1986) 435.

39 K. H. Quandt and R. Streicher, International Journal of Hydrogen Energy, **11** (1986) 309.

40 W. Donitz and E. Erdle, International Journal of Hydrogen Energy, **10** (1985) 291.

41 E. Erdle, W. Donitz, R. Schamm, and A. Koch, International Journal of Hydrogen Energy,**17** (1992) 817.

42 R. Accorsi and E. Bergmann, Journal of The Electrochemical Society, **127** (1980) 804.

43 J. Martinez-Frias, A-Q. Pham, and S. M. Aceves, International Journal of Hydrogen Energy, **28** (2003) 483.

44 G. Tao, T. Armstrong, A. Virkar, DOE Hydrogen Program Annual Review, May 23, 2005, Project ID PD2.

45 C. E. Milliken and R. C. Ruhl, Porceedings of the 2002 U.S. DOE Hydrogen Program Review, NREL/CP-610-32405.

46 S. Herring et al., Presentation at DOE Hydrogen Program Annual Review Meeting, Project # PD17, Crystal City, VA, 5/17/2006.

47 M. Mogensen, S. H. Jensen, A. Hauch, I. Chorkendorff, and T. Jacobsen, 7th European SOFC Forum, 3–7 July 2006, Kultur- und Kongresszentrum Luzern, Lucerne / Switzerland.